Multi-scale modeling of paracrine PDGF-driven glioma growth and invasion

Susan Christine Massey

A dissertation
submitted in partial fulfillment of the
requirements for the degree of

Doctor of Philosophy

University of Washington

2016

Reading Committee:

Kristin R. Swanson, Chair

Randall J. Leveque

Jose Nathan Kutz

Hong Qian

Program Authorized to Offer Degree:
UW Applied Mathematics

University of Washington

Abstract

Multi-scale modeling of paracrine PDGF-driven glioma growth and invasion

Susan Christine Massey

Chair of the Supervisory Committee:
Affiliate Professor Kristin R. Swanson
Applied Mathematics

The most common primary brain tumor in adults, glioma claims thousands of lives each year. Despite efforts to improve survival rates, the standard of care has remain unchanged for more than a decade. Recent research has started to uncover the role of stromal involvement in the growth of gliomas. Consisting of the supportive cells in the tissue, these stromal cells had long been overlooked in finding strategies for treating cancers. One particular component of this stromal support of gliomas is plateletderived growth factor (PDGF). PDGF is secreted by a number of cells in the brain, and has a number of cellular targets, including oligodendroglial progenitor cells. In animal models, upregulated PDGF signaling leads to the formation of tumors similar to human gliomas through the recruitment of oligodendroglial progenitor cells by PDGF. Central to my work is the mathematical examination of the effects of paracrine PDGF signaling on normal brain tissue and in brain tumor formation using PDE models. Model simulations show that PDGF can drive a number of outcomes in response to brain injury, and that increased PDGF signaling can speed up tumor growth and can alter the steepness of the tumor density gradient extending into adjacent normal brain tissue. Greater understanding of the contributions of PDGF in the development and growth of tumors may lead to much needed new strategies for combating glioma.

TABLE OF CONTENTS

LIST OF FIGURES

Figure Number Page

LIST OF TABLES

GLOSSARY

ANGIOGENESIS: the formation of new blood vessels from pre-existing ones; this commonly occurs in tumors in response to increased cellular density and increased demand for oxygen and nutrients.

ASTROCYTE: a type of glial cell named for its star shape; closely associated with neural synapses.

AXON: a long projection of a neuron that conducts electrical impulses away from a neuron.

CORPUS CALLOSUM: bundle of nerve fibers in the brain that connects both brain hemispheres; the largest white matter structure in the brain.

CORTEX: the outer layer of the brain, consisting of gray matter.

CYTOKINES: broad category of small proteins that are important in cell signaling, especially in immune function; produced by immune cells and stromal cells.

DENDRITE: branched projections from neurons that receive electrochemical input from other neurons and transmit these signals to the body of the neuron.

GLIA: non-neuronal cells in the nervous system which provide structure and support for neurons, including the maintenance of homeostasis and assitance in formation of synaptic connections between neurons; name derives from the greek for glue as its role was initially thought to be simply holding the brain together.

GLIOMA: a brain tumor consisting of cells that are glial in origin. This is the most common type of brain tumor in adult humans.

GRAY MATTER: tissue in the brain and nervous system consisting largely of neuronal cell bodies, myelinated and unmyelinated axons, glial cells, synapses, and capillaries; looks gray in contrast to adjacent *white matter*.

MESENCHYME: a type of tissue arising in embryological development consisting of loosely associated cells surrounded by a large extracellular matrix; mesenchymal cells are able

to develop into tissues of the lymphatic and circulatory system as well as connective tissues. In adults, *mesenchymal stem cells* exist in the stroma of various organs and do not differentiate into blood cells, but do give rise to many types of stromal cells and are broadly important in tissue repair.

MULTI-SCALE: spanning multiple temporal and/or spatial scales. Examples in this work include μm vs. cm, and minutes vs. days, where the former units describe the appropriate scale of cells and the latter the scale of tumors.

MYELIN: a fatty white substance that grows out of glial cells (oligodendroglia in the brain and spine, Schwann cells in the peripheral nerves) to surround axons and form nerve fibers; acts as an electrical insulator and improves speed of electrical impulse propagation along the axon.

NEURON: an electrically excitable cell consisting of a cell body, dendrites, and an axon; processes and transmits information through electrical and chemical signals, forming networks when connected with other neurons.

OLIGODENDROCYTE: a type of glial cell found only in the central nervous system; provides insulation to neuronal axons by forming myelin sheaths with its projections.

OLIGODENDROGLIAL PROGENITOR CELL (OPC): a type of cell that is found in the brain; these cells express PDGFRα and can differentiate into oligodendrocytes and type 2 astrocytes, two types of "white matter" brain cells.

PARACRINE: a type of chemical signaling in which a cell signals to other nearby cells which express receptors for the emitted signal.

PARENCHYMA: the portion of tissue in an organ which carry out that organ's specialized funtions; often defined in contrast with stroma.

PLATELET–DERIVED GROWTH FACTOR (PDGF): a protein that is produced by many different cells of mesenchymal origin and that stimulates growth of cells that express platelet-derived growth factor receptors.

PLATELET–DERIVED GROWTH FACTOR RECEPTOR (PDGFR): a protein belonging in the family of receptor tyrosine kinases. There are two types, called PDGFRα and PDGFRβ.

PROLIFERATION–INVASION (PI) MODEL: the brain tumor model which describes the *proliferation* of brain tumor cells and their *invasion* into the adjacent normal brain. This model has been used to analyze the growth of human gliomas (see [41, 96, 97]).

PROLIFERATION–INVASION–RECRUITMENT (PIR) MODEL: the brain tumor model described in this dissertation, which captures the growth of tumors similar to that in the PI model, but also incorporates the *recruitment* effects of PDGF on the cells that contribute to the tumors.

PRONEURAL GLIOMA: a genetically defined subtype of glioma based on patterns found in the Cancer Genome Atlas (TCGA); these tumors contain alterations in gene expression of PDGFRA (the gene encoding for the PDGFRα protein) among other aberrations.

RECRUITMENT: the term used herein to describe the process of oligodendroglial progenitor cells behaving as tumor in response to binding paracrine PDGF ligand.

STROMA: the structural portion of tissue in an organ consisting of connective tissue and blood vessels; often defined in contrast with parenchyma.

WHITE MATTER: tissue in the brain central nervous system consisting primarily of myelinated axons; the white color of the tissue is due to the lipids in the myelin.

ACKNOWLEDGMENTS

My deepest thanks go to the many people who supported me throughout the process of earning my doctorate.

First, I would like to thank my adviser, Professor Kristin R. Swanson, for her guidance and support. She inspired me to go enter the field of mathematical biology when I encountered her work during my undergraduate years. I have been very priviledged to work with Dr. Swanson at the leading edge of mathematical medicine. Her flexibilty and unwavering support also allowed me to take care of my mom and younger brother while working on my Ph.D. and to make the most of Mom's last years and months. For this gift I will be eternally grateful.

Next, I must also thank each of my committee members, Professors Hong Qian, Randall J. Leveque, and J. Nathan Kutz, for taking the time to evaluate my work. Their suggestions and feedback have greatly strengthened this dissertation.

The department administrators have been invaluable. Lauren Lederer helped make sure I followed all the Graduate School procedures correctly, which was sometimes challenging as I worked from a distance. Keshanie Dissanayake helped me navigate funding procedures, especially when my adviser relocated.

I would like to extend my gratitude to my collaborator, Professor Peter Canoll, Columbia University Neuropathologist, for sharing biological data and for many insightful conversations that have helped guide my research pursuits.

My labmates, especially Andrea Hawkins–Daarud and Pamela R. Jackson, have offered lots of helpful feedback and advice, and proofread my papers. I feel fortunate to have had their support and encouragement.

I must also acknowledge the critical role of Dr. Ellsworth C. "Buster" Alvord, Jr. (1923-

2010), University of Washington Neuropathologist, in the development of my my field. His ideas led to the development of clinically useful models of gliomas in collaboration with Professor James Murray in the 1990's. It was a great honor of mine to be able to work with him in his final years, even as he was in "retirement." He remains a great inspiration to all of us.

Furthermore, I would like to acknowledge my primary funding sources. I was supported by the National Science Foundation Graduate Research Fellowship grant DGE-0781824, an NSF Vertical Integration of Research and Education in the Mathematical Sciences (VIGRE) Fellowship, and by the James S. McDonnell Foundation.

Finally, I want to thank my friends and family for encouraging and believing in me. Natasha "Alex" Cayco Gajic taught me how to properly balance work and fun and helped me through some very rough times as I lost my mother. My brother, Jordan, and sister, Carmen, have been incredibly supportive, and their looking up to me has kept me hard at work over the years, while also making sure I take time to enjoy life along the way. I could not have done this without you.

DEDICATION

For my mother, Paula Mae Hansen (1964-2013),
who's twelve year battle with leukemia taught me a great deal
about hope, persistence, and celebrating life to its fullest.
I miss you every day, "Smomster."

Chapter 1

INTRODUCTION.

1.1 Background and Motivation

Of all the myriad lethal diseases in the world anyone could get, glioma is arguably among the worst. Glioma is the most common type of primary brain cancer, composed primarily of the white matter cells of the brain, known as glia. These tumors are diffusely invasive, making them especially difficult to treat and prone to recurrence. Glioblastoma is the most aggressive form of the disease. It is uniformly fatal, and most patients with this disease die 14–16 months after diagnosis [61].

1.1.1 PDGF as a central biological driver

Normal glial cells can be of several different types—my work is mainly focused on the role of undifferentiated oligodendroglial progenitor cells (cells can that give rise to a few different types of glia). These cells express receptors for Platelet-derived growth factor (PDGF). PDGF was first described as a molecule produced by platelets that stimulates mitosis of arterial smooth muscle cells [52, 85]. In the decades since its discovery, it has been shown that various types of PDGF are secreted by many other cells, including smooth muscle cells, monocytes, macrophages, endothelial cells, epithelial cells, and glial cells [29, 43]. The two receptors of PDGF, known as PDGFRα and PDGFRβ, are expressed by an even greater number of cells, including mesenchymal and stromal cells such as hepatic stellate cells, mesangial cells, osteoblasts, fibroblasts, and oligodendroglial progenitor cells [4, 5, 42, 43, 86]. These cells are driven to proliferate, migrate, and sometimes differentiate in response to PDGF signal [29, 36, 43].

PDGF signaling is critical for development, with genetic knockout mutations in experi-

mental mouse models leading to defects in cardiac and skeletal formation, as well as deficits in brain myelination, which results in lethality during embryogenesis [14, 45]. In adults, PDGF signaling is involved in many types of maintenance functions. The role of PDGF in dermal wound healing has been particularly well described [43]. PDGF has an angiogenic effect, particularly in the heart, and it also affects vasoconstriction and blood pressure [13,31]. Further, PDGF produced in capillaries and arteries can recruit pericytes and smooth muscle cells, contributing to injury repair and the maintenance of vessel integrity [38, 64]. In this capacity, it contributes to the regulation of the blood brain barrier [8]. But it does more than that in the CNS: PDGF also stimulates axonal remyelination through the proliferation, migration, and differentiation of oligodendroglial progenitor cells [1, 82]. Recently, PDGF and other growth factors have shown some promise as therapies to be given to patients undergoing orthopedic surgeries and oral surgeries involving dental implants and bone grafts to enhance repair and healing [5, 15, 56], paving the path for other therapeutic uses of recombinant PDGF.

PDGF acts through both paracrine and autocrine signaling pathways. Autocrine signaling means that the cell type producing the PDGF is *itself* stimulated by PDGF, while paracrine signaling means that other cells *near* to the PDGF–secreting cell are stimulated by the PDGF. This latter type of signaling is a central concern of my work, as it forms the basis of tumor cell interactions with adjacent tissue stromal cells. In other diseases, PDGF has been shown to lead to tissue pathologies through its effect on these stromal cells, particularly fibrosis, and such stromal changes have been shown to play an important role in the growth of cancers [28, 40, 58]. For example, and it is involved hepatic fibrosis and steatosis, leading to the development of hepatocellular carcinoma (liver cancer) [22, 42, 115].

Some experiments have shown that PDGF can drive the formation of brain tumors that are very similar in character to human glioma, as well—most notably capturing their invasiveness—through its effect on oligodendroglial progenitor cells [9, 10, 35]. The set of experiments in [9] showed that a small number of cells that were genetically altered to produce PDGF, and the PDGF that those cells released caused the normally present oligo-

dendroglial progenitors to grow and divide. Essentially, they behaved as cancer cells and were "recruited" to the tumor through paracrine PDGF signaling. Thus, these experimental tumors that look so similar to human tumors, possessing the diffuse invasiveness that other experimental glioma models failed to capture, consisted mostly of normally–occurring glial progenitors, with only a small proportion of aberrant cells. Furthermore, the Cancer Genome Atlas (TCGA) shows that gene mutations related to oligodendroglial progenitors, PDGF, and PDGF receptors are linked to the proneural subtype of human glioma [111], meaning that they could be playing an important role in a significant subset of human cases.

One question arising from these experimental animal models was whether this afore described *recruitment* process could realistically occur to such a dramatic extent in the human disease. More broadly, I wanted to explore the relationship between oligodendroglial progenitor cells and paracrine PDGF signaling to better understand the possible contribution of paracrine–mediated recruitment in glioma growth dynamics, and possibly even the origin of some gliomas. Since it is difficult to study the early origins of these tumors in humans, mathematical modeling has proved to be a useful tool for synthesizing the information that is known and testing hypotheses about how PDGF molecules affect brain tissue and brain tumors.

1.1.2 History of Mathematical Modeling of Brain Tumors.

Mathematical modeling of tumors has a long history, with roots extending back into the 1950's. At that time, there was an increase in interest and new methodologies to understand cell division and the controls of cellular division in tumor cells [93, 94]. This included the emergence of H^3-thymidine labeling in autoradiographic cellular proliferation assays [3,32,37, 53, 54, 70–74, 104]. Specific techniques allowed more precise quantification of division rates, and in 1965 the first mathematical model of intestinal crypt cell growth was published [20,21]. These early tumor models were further refined in the 70's by G. Steel, who wrote a thorough review of this early time of tumor modeling in [91].

Fastforward to the mid-1990s: University of Washington Neuropathologists Dr. Ellsworth

Alvord, II and Dr. Cheng-Mei Shaw started adapting Steel's model using data from brain tumors [2, 26]. Dr. Alvord enlisted the assistance of Applied Mathematics Professor James Murray, and together they built a novel mathematical model of glioblastoma multiforme, a particular type of glioma with an especially poor prognosis. This model consists of a reaction diffusion partial differential equation (PDE), which models the diffuse distribution of tumor cells emmanating from a dense core "source" characteristic of these tumors:

$$c_t = \nabla \cdot (D \nabla c) + \rho c,$$

where c is the number of tumor cells, D is the diffusion coefficient, and ρ is the rate of cell division. The initial condition $c(x, t = 0) = f(x)$ describes the spatial distribution of initiating tumor cells, usually taken to be a point source.

Continuing this work into the 2000's, Professor Kristin Swanson refined the model [96,97] to make it more spatially accurate, and improve the model's clinical applicability:

$$c_t = \nabla \cdot \left(\vec{D}(\vec{x}) \nabla c \right) + \rho c,$$

where $\vec{D}(\vec{x})$ is a vector of diffusion coefficients that differ the in gray versus white matter of the brain. Thus,

$$\vec{D}(\vec{x}) = \begin{cases} D_g & \text{if } x \in \text{gray matter region of the brain;} \\ D_w & \text{if } x \in \text{white matter region of the brain.} \end{cases}$$

This is then implemented on a 3-dimensional brain atlas that describes where the white and gray matter of the brain are spatially, to the resolution of one cubic millimeter voxels [41].

My own work is focused on extending these glioma models to include tumor–stromal interactions mediated by paracrine PDGF signaling. Because we have interacting species that operate on different spatial and temporal scales, namely cells and molecules, a large component of extending these models was finding a way to bridge these scales, giving us a multi-scale model.

1.2 Overview.

In this dissertation, I begin by modeling the wounding process in the brain (Chapter 2—this introduction is Chapter 1). Since PDGF plays a role in wound healing and contributes to the formation of gliotic scars, I have here modeled the interplay between glial progenitor cells and PDGF released following a needle wound. This was largely based on the controls from the experiments done in [9,10]. Although this model was actually created after the full tumor model in Chapter 4, I have presented it here first as a simpler introduction to the modeling approach taken for bridging scales. First, we walk through the model design. I then analyze the linear stability of the model at the uniform steady states, both to spatially homogeneous and spatially heterogeneous perturbations (Section 2.3). My analysis shows that the model is stable in the physiologic domain, and therefore I would not expect to see any patterning for physiologically relevant simulations. Finally, I present model simulation results. My model shows the formation of a stable durable gliotic scar in response to the PDGF released during the wound incident.

We expand upon this wound model in Chapter 3 by adding a source term. This chapter consists of a paper submitted to the Journal of Theoretical Biology in 2016. Adding the PDGF source allows us to investigate the effects of varied PDGF secretion behavior following an injury. After discussing the formation of the model itself, we examine the results from a set of simulations spanning the range of PDGF secretion parameters. These simulations show that different dynamics of PDGF secretion can lead to the mild recruitment of oligodendroglial progenitors seen in small healed wounds as observed in Chapter 2, through longer lasting periods of recruitment such as with scars, to large areas of recruitment that persist for long periods of time, similar to neoplasia. We discuss the implications of this, including the connection with case reports of tumors that developed in regions of patients' brains in locations where years prior there had been traumatic brain injury.

Chapter 4 consists of a paper published in the Journal of the Royal Society Interface in 2012 [67]. This paper presents a model of the experimental PDGF-driven tumors in [9]

simulated in one dimension with spherical symmetry (that is, we look at what happens along the radius of a model tumor). We call this model the proliferation-invasion-recruitment (PIR) model. Since the paper was written for a more general audience, I walk through the more basic model assumptions, present the model, and then turn directly to presenting simulation results. Going through the simulation results, we see that the model corresponds well with the experiment, and suggests that dramatic levels of recruitment are compatible with the growth dynamics seen in human glioma cases. Furthermore, the level of recruitment could at least in part explain some of the variation in observed human growth dynamics (i.e., recruitment leads to more nodular lesions). Finally, I discuss some of the experimental methods relevant to model creation and go through the finer details of model development, which were originally given in the supplemental material to the paper.

Important to model creation was data analysis and parameterization, which gets full treatment in Chapter 5. Through strong collaborations with researchers in the departments of Neurosurgery and Neuropathology at Columbia University, I had unique access to vast amounts of cell tracking data to examine and quantitatively characterize cell behavior in experimental tumors. This gave us the opportunity to use data to parameterize the proliferation and invasion rates of tumor cells. Some of this parameterization was given in the paper of Chapter 4 and its supplement, but I expand on the discussion of this analysis, placing it in a larger context. Here I also discuss the utility of individual cell tracking analysis for examining the efficacy of potential anti-invasive therapies, as I did for the analysis in [49].

In Chapter A, I find the steady states of the PIR model. Only one of these turns out to be physically possible. However, this steady state is physiologically unattainable since it occurs when the entire brain has become tumor—lethality occurs well before that.

Sensitivity analysis of the PIR model is presented in Chapter 6. This was done using the technique of Latin hypercube sampling (LHS) with Monte Carlo simulations and partial rank correlation coefficients (PRCC). In this chapter, we walk through the steps of the technique and discuss its application for our particular analysis. Finally, we look at the results of the sensitivity analysis and discuss the implications.

I extend the PIR model to two dimensions in Chapter 7, executing simulations on a mouse brain atlas with different diffusion rates in gray versus white matter regions (improving the original model which was not able to handle this geometric consideration). The material in this chapter was submitted as a paper to the Bulletin of Mathematical Biology in 2016 to be included in a special issue on Mathematical Oncology. Simulations focus primarily on comparing the effects of varied rates of PDGF secretion (and thus rates of recruitment) and varied gray–white differential diffusion rate on tumor growth. Those with higher recruitment grow faster, and tumors with recruitment are more nodular than those that have no recruitment. This result is similar to the one found for the 1D PIR model. Simulations with increased difference between the rate of diffusion in gray matter versus the rate in white matter show a greater proportion of tumor contained in the white matter. This is consistent with findings in human glioma that some tumors show a greater proclivity for white matter and are thus noted as "white matter disease." The 2D model simulations also present more compelling visual comparisons to the experiment, appealing to the biological audience. Overall, we see that recruitment remains important to understanding glioma growth.

1.3 Goal.

Ultimately, the goal of my work in this dissertation is to connect the experimental with the human. Through mathematical tools, I have aimed to better flesh out the implications of paracrine PDGF signaling in interactions between glioma and brain stroma for the human disease. Hopefully this will help guide future understanding of the larger picture of glioma growth and lead to new therapeutic opportunities.

Chapter 2

MODEL OF NEEDLE WOUNDING EFFECT IN BRAIN TISSUE IN EXPERIMENTAL RAT MODEL

2.1 Background

Experiments have shown that a genetic alteration in one cell population can cause other cell populations to behave as cancer [9, 35], but those experiments involve injecting brain tissue, thus causing injury. It is also known that injury to brain tissue can cause a release of growth factors that cause cells to divide (proliferate) and migrate (diffuse), apart from any substances that are injected locally. Because the needle insertion injury incurred during injection stimulates production of the same growth factor as that which is upregulated by the experimental virus, studying a control injection gives a basis on which to build the more complex model.

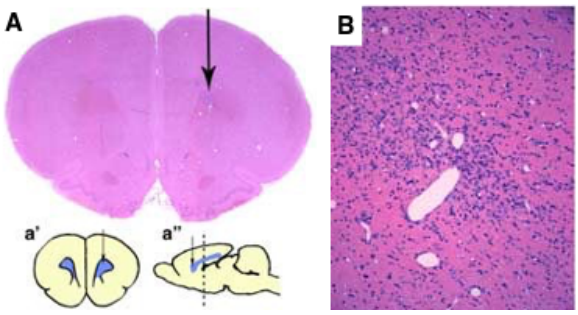

Figure 2.1: **Gliosis due to injection of control virus.** A. Slice of rat brain injected with control virus (i.e., not expressing PDGF), stained with hemotoxylin and eosin (H&E). Arrow points to location of gliotic scar. a' and a" show location of injection in overall rat brain. B. Higher maginification of the scar histology. Images reprinted from [9].

To differentiate between (a) the effect of transducing cells (i.e., cells are infected with a retrovirus that causes a change in their genes) to induce a glioma-like tumor in an animal model and (b) the effect of inserting the needle, an experiment was done with a control virus (i.e., one that does not cause a genetic change) [9]. This virus lacks the part that codes for upregulating the growth factor, and this "empty" virus produces no tumor. Instead, it produces a localized region that is denser than the surrounding tissue, called a gliotic scar, in a process known as gliosis (see Figure 2.1).

When cells are injured by the needle and the pressure from injection, they naturally release growth factors to help aid in repairing the demage to the tissue, not unlike the process that occurs when the skin is cut, then scabs over and heals. Those growth factors cause cells to divide rapidly and migrate in to replace the damaged stromal cells and reconnect blood vessels, thus restoring the tissue overall, but leaving the gliotic scar.

We can model this process of gliosis with two equations: one describes the growth factor dynamics initiated by the injury, and the other describes the cells that respond to the growth factor to repair the damage to the brain tissue.

2.2 Model Equations

The first equation for the wound describes the cells that respond to the release of growth factors by the injury. The cells divide and migrate, through diffusion and chemotaxis, in a spatially and temporally dependent manner, so we have a reaction-diffusion-advection partial differential equation:

$$\overbrace{\frac{\partial r}{\partial t}}^{\substack{\text{rate of}\\ \text{change of}\\ \text{glial}\\ \text{progenitor}\\ \text{density}}} = \overbrace{\nabla \cdot \left(\overline{D_r}\left(r,p\right)\nabla r\right)}^{\substack{\text{diffusion of glial}\\ \text{progenitor cells,}\\ \text{depends on local}\\ \text{PDGF concentration}}} + \underbrace{\overbrace{\overline{\rho_r}\left(p\right)r}^{\substack{\text{PDGF dependent}\\ \text{exponential net}\\ \text{proliferation at}\\ \text{low cell density}}} \overbrace{\left(1-\frac{r}{K}\right)}^{\substack{\text{limit net}\\ \text{proliferation}\\ \text{when space}\\ \text{is limited}}}}_{\substack{\text{net proliferation of}\\ \text{glial progenitor cells}}} \tag{2.1}$$

The second equation describes the behavior of growth factor released by injured cells to

incite repair of the tissue. Growth factor is consumed by the progenitor cells, r, and diffuses into the surrounding tissue. We do not incorporate any PDGF decay because consumption occurs on a much faster time scale, such that no PDGF remains to decay. For this equation we have the following reaction-diffusion partial differential equation:

$$\overbrace{\frac{\partial p}{\partial t}}^{\substack{\text{rate of change of extracellular PDGF concentration}}} = \overbrace{\nabla \cdot (D_p \nabla p)}^{\text{diffusion of PDGF}} - \underbrace{\overbrace{q_r}^{\substack{\text{rate of PDGF consumption by glial progenitors}}} \overbrace{\beta\,(p)}^{\substack{\text{percent of cell receptors bound to PDGF}}} r}_{\substack{\text{consumption of PDGF by glial progenitors}}} \tag{2.2}$$

2.2.1 Model Formulation

In formulating our model, we started with the formalism of reaction-diffusion partial differential equations to capture the movement (diffusion terms) and birth/death (reaction terms) of cells and PDGF. We could use a reaction-diffusion-advection system to account for any advective or chemotactic movement, but data suggests that diffusion is a good approximation for the movement of the cells we are interested in (see [30, 92] and chapter 5), as well as for that of the PDGF molecules. Thus, for our purposes, it was not worth the added computational cost of including an advection term.

Reaction. For the cells, r, we have an experimentally observed cell division rate, $\overline{\rho}_r$ giving a birth term of the form $\overline{\rho}_r r$. There is no death or loss of r cells. Moving to the equation for PDGF, p, we have no birth term, only a death term. In the wounding experiment, our only PDGF source is the initial release of PDGF, p_0; since we assume no PDGF is produced beyond the time of injury, t_0 (see section 2.2.2 for details on initial conditions), we do not have a birth term in the PDGF equation. We do have a death term in our equation for PDGF, p, however, as the PDGF molecules are taken up by the r cells. The most basic form of this death rate is $-q_r(p)r$, where $q_r(p)$ is the rate of consumption, which is dependent upon p. This dependency is discussed in the section below about Michaelis-Menten terms.

Diffusion. In the case of the r cells, we have an experimentally observed net migration rate, $\overline{D}_r$. (Throughout, the overline on D's and ρ's indicates the *attained* or *observed* rate as

opposed to a *maximal* rate, since, as we discuss in the following paragraphs, these parameters are dependent on variables.) The diffusion term in our PDE thus takes the form $\nabla \cdot \left(\overline{D}_r \nabla r\right)$. The diffusion term for the PDGF, p, is similar: $\nabla \cdot (D_p \nabla p)$.

The model as described thus far, has the form:

$$\frac{\partial r}{\partial t} = \nabla \cdot \left(\overline{D}_r \nabla r\right) + \overline{\rho}_r r$$
$$\frac{\partial p}{\partial t} = \nabla \cdot (D_p \nabla p) - q_r(p) r.$$

However, this is not sufficient to describe the basic dynamics of the experiment. For example, we have not included the dependency on PDGF, p, in our equation for the r cells. Therefore we require a few refinements.

Logistic Growth. The brain is a finite domain with a no flux boundary, i.e. the skull. Because cells take up space and there is limited space in the brain, it has a carrying capacity, which we represent with parameter K in units of cells/mL. This carrying capacity not only affects the birth rate of new cells - meaning that fewer new cells can be made in a dense location, it also affects the ability of cells to move (not unlike traffic flow responding to the density of cars on the road.) We account for this density restriction upon the cells via a multiplicative logistic growth factor of the form $\left(1 - \frac{r}{K}\right)$ that we incorporate into the diffusion and proliferation terms of the r cells. Thus, at higher values of r, this factor gets closer to 0, scaling down these rates, whereas at low values of r, the value of this factor is closer to 1, imposing little constraint on the rates of migration and proliferation.

Michaelis-Menten Kinetics. An additional refinement to our equations involves incorporating the dependence of terms upon p. First and foremost, the rate of consumption of PDGF by cells depends on the local concentration of PDGF, as little may be taken up when little PDGF is locally present. Furthermore, through uptake of the PDGF signal, the cells will increase their rates of migration and proliferation. To capture these dependencies, we rely on the Michaelis-Menten formalism of enzyme kinetics.

Briefly, this formalism states that the observed rate of a reaction (in this case free PDGF

molecules binding to cell surface receptors and being taken up) is equal to the max reaction rate multiplied by the ratio of substrate concentration to substrate concentration plus a constant. This constant is the substrate concentration at which the half maximal reaction rate is attained, called k_m.

That is,

$$\text{Rate}^{\text{observed}} = \frac{\text{Rate}^{\max}[\text{substrate}]}{k_m + [\text{substrate}]} \tag{2.3}$$

Specifically, for our consumption rate $q_r(p)$, we have

$$q_r(p) = q_r^{observed} = q_r^{max}\frac{p}{k_m + p} \tag{2.4}$$

and thus our equation for $\partial p/\partial t$ becomes:

$$\frac{\partial p}{\partial t} = \nabla \cdot (D_p \nabla p) - q_r \frac{p}{k_m + p} r, \tag{2.5}$$

where we take parameter q_r to be the maximum possible consumption rate *per cell.* [1]

Incorporating the dependence of proliferation and migration rates is somewhat similar, but relies on another parameter, the EC_{50}. This constant is the concentration of a substrate, in our case p, at which the *half maximal effect* is observed for some "downstream" action of the substrate, such as cellular proliferation and migration.

Replacing the Michaelis-Menten k_m with EC_{50} results in the Pharmacodynamic (PD) term:

$$\text{Effect}^{\text{observed}} = \text{Effect}^{\max}\frac{[\text{substrate}]}{EC_{50} + [\text{substrate}]}. \tag{2.6}$$

This form corresponds with the curves in Figure 2.2. Notice that the curve for $EC_{50} = 10^{1/2}$ most closely approximates the data (shown by the circles), but the shapes of these curves don't quite match the shape given by the data.

However, when we change the response, scaling all of those terms by k_m, as with the rate

[1] Compare this consumption term with equation (6.42) in [75], $ds/dt = -Qs/(k_m + s)$, which describes uptake of a substrate. The primary difference is that our rate q_r is "per cell" and thus multiplied by the local number of cells.

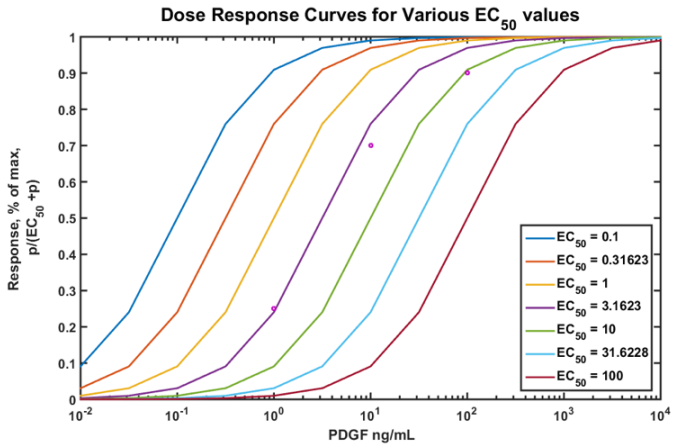

Figure 2.2: **Response Curves: Simple Pharmacodynamics form.** Here we see the dose response curves that correspond to the Pharmacodynamic (PD) formulation of downstream response to PDGF. Legend indicates the varied EC_{50} parameter value corresponding to a given curve. Circles correspond to data from [81]. Notice that these do not quite fit the shape suggested by the data.

terms above, we have:

$$\text{Effect}^{\text{observed}} = \text{Effect}^{\max} \frac{\frac{[\text{substrate}]}{k_m + [substrate]}}{\frac{EC_{50}}{k_m + EC_{50}} + \frac{[\text{substrate}]}{k_m + [\text{substrate}]}} \tag{2.7}$$

which results in the curves shown in both panels of Figure 2.3. As you can see in those plots, we get curves whose shape better approximates that given by experimental data [81]. These curves also suggest the best parameter value choices for k_m and EC_{50}:

$$k_m = 30 \text{ ng/mL and } EC_{50} = 10^{1/2} = \sqrt{10} \text{ ng/mL}. \tag{2.8}$$

Letting

$$\beta(p) = \frac{p}{k_m + p} \text{ and } \gamma = \beta(EC_{50}) = \frac{EC_{50}}{k_m + EC_{50}}, \tag{2.9}$$

to make things less messy in appearance, we have response

$$\text{Effect}^{\text{observed}} = \text{Effect}^{\max} \frac{\frac{[\text{substrate}]}{k_m + [substrate]}}{\frac{EC_{50}}{k_m + EC_{50}} + \frac{[\text{substrate}]}{k_m + [\text{substrate}]}} = \text{Effect}^{\max} \frac{\beta(p)}{\gamma + \beta(p)}. \tag{2.10}$$

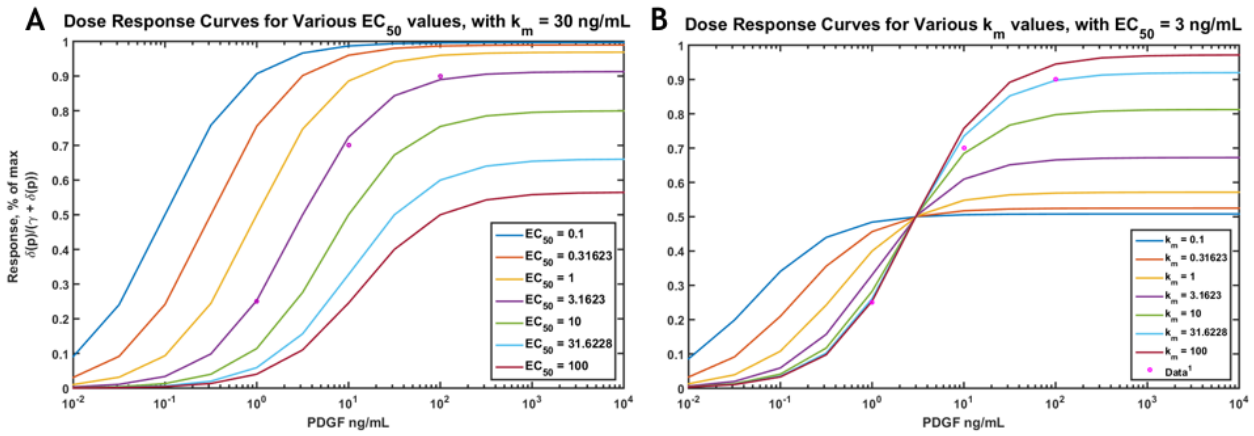

Figure 2.3: **Response Curves: Incorporating k_m and EC_{50}.** Panels show the modified response, where we have scaled by k_m to better match the shape traced by the data points. Because this response includes k_m, we have a panel with varied EC_{50} (A) as well as a panel with varied k_m (B). Legends indicate values of the varied parameter value corresponding to a given curve. Circles in both panels correspond to data from [81]. Panel A shows varied EC_{50} for fixed $k_m = 30$ ng/mL, while panel B shows varied k_m for fixed $EC_{50} = 3$ ng/mL. Notice that the curve corresponding to $EC_{50} = 10^{1/2} \approx 3.1$ ng/mL (panel A) and that corresponding to $k_m = 10^{3/2} \approx 31.62$ ng/mL (panel B) best fit the data points.

Thus our cellular diffusion rate in response to PDGF now takes the form:

$$\overline{D}_r(r,p) = D_r \frac{\beta(p)}{\gamma + \beta(p)} \left(1 - \frac{r}{K}\right), \tag{2.11}$$

and the proliferation rate:

$$\overline{\rho}_r = \rho_r \frac{\beta(p)}{\gamma + \beta(p)} \left(1 - \frac{r}{K}\right). \tag{2.12}$$

Finally we arrive at the model equations presented at the beginning of the section:

$$\frac{\partial r}{\partial t} = \nabla \cdot \left(D_r \frac{\beta(p)}{\gamma + \beta(p)} \left(1 - \frac{r}{K}\right) \nabla r \right) + \rho_r \frac{\beta(p)}{\gamma + \beta(p)} \left(1 - \frac{r}{K}\right) r \tag{2.13}$$

$$\frac{\partial p}{\partial t} = \nabla \cdot (D_p \nabla p) - q_r \frac{p}{k_m + p} r. \tag{2.14}$$

with initial conditions r_0 and p_0, as discussed in the following section.

2.2.2 Initial and Boundary Conditions

For this model, we have an inciting event that sets everything in motion: the injury. Since the injury occurs over a very short period of time, we start the simulations immediately post-injury, avoiding the complexity of simulating the event itself. Thus, we start with a non-zero initial condition for p, i.e., the amount of PDGF released upon injury.

Initial PDGF Concentration, p_0. While we do not have an exact, measured value for p_0, we do have data from looking at proliferation rates in brain tissue, with and without added PDGF [10]. Briefly, this experiment compares cellular proliferation of cells in rat brain tissue in tissue with added exogenous PDGF (experimental condition), and without (control condition). The harvested tissue (without any added exogenous PDGF) has some level of PDGF due to the injury involved in removing it from the animal, so through comparing these, we can estimate the PDGF released by injury. Specifically, it was observed that adding 100 ng/mL of PDGF to the experimental condition caused an approximately four-fold increase in proliferation rate as compared to the control condition.

Thus, they both start with some baseline amount, which we'll designate with variable s. Then the experimental case is given additional PDGF, so that the control has s ng/mL PDGF, and the experimental condition has $s + 100$ ng/mL PDGF. Response is measured in proliferation, a downstream effect of PDGF, so we can use our downstream effect response term in our model equations, where response to PDGF is

$$R(p) = \frac{\beta(p)}{\gamma + \beta(p)}, \text{ where } \beta(p) = \frac{p}{k_m + p} \text{ and } \gamma = \frac{EC_{50}}{k_m + EC_{50}}. \tag{2.15}$$

In our model, we use parameter values $k_m = 30$ ng/mL and $EC_{50} = \sqrt{10}$ ng/mL (see equation (2.8) and preceding paragraph).

Using this response term in combination with the experimental result, we have the relationship

$$R(p + 100) = 4R(p) \tag{2.16}$$

which means "response in the experimental case is equal to four times the response in the control case."

Expanding this relationship using the definition of $R(p)$, we have:

$$R(p+100) = 4R(p) \tag{2.17}$$

$$\frac{\beta(p+100)}{\gamma+\beta(p+100)} = 4\frac{\beta(p)}{\gamma+\beta(p)} \tag{2.18}$$

which we then solve for p (detailed algebra can be found in the following chapter, in section 3.5).

This gives us

$$p = 0.8415, -103.45 \tag{2.19}$$

Since the latter of these does not make sense as a physical quantity, we adopt the first as our approximate value for p_0:

$$p_0 = 0.8145 \text{ ng/mL}. \tag{2.20}$$

The control and experimental conditions from the experiment are plotted against the model dose response curve in Figure 2.4.

Initial Glial Progenitor Cell Density, r_0. Glial progenitors, r, have a baseline level of about $r_0 = 2.21 \times 10^6$ cells/mL. This was determined by counting glial progenitors labeled by an injection of immunofluorescent labeling proteins. 250 cells were found in a spherical volume of radius 300 μm = 0.03 cm, which gives us $\frac{250}{\left(\frac{4}{3}\right)\pi \cdot 0.03^3}$ cells/cm^3 or cells/mL (personal communication from Peter Canoll, June 2008). Evaluating this, we get approximately 2.21×10^6 cells/mL. In the human brain, glial progenitors have a maximum relative abundance of about 3-4% [79,87,88], and if we let 3% of our estimate for the normal cellularity of the brain represent glial progenitors, we also arrive at approximately 2×10^6. While our experiment takes place in rat brains, and not those of humans, this data confirms that our cell count based estimate provides a reasonable order of magnitude from which to start.

Boundary. Although the effect of this wounding event occurs locally and does not show an effect in a distant region of the brain, we take the whole brain as our domain, and the skull as the boundary. This best matches the actual biological setting. For simplicity, we simulate the model in one dimension, assuming spherical symmetry. The rat brain is approximately

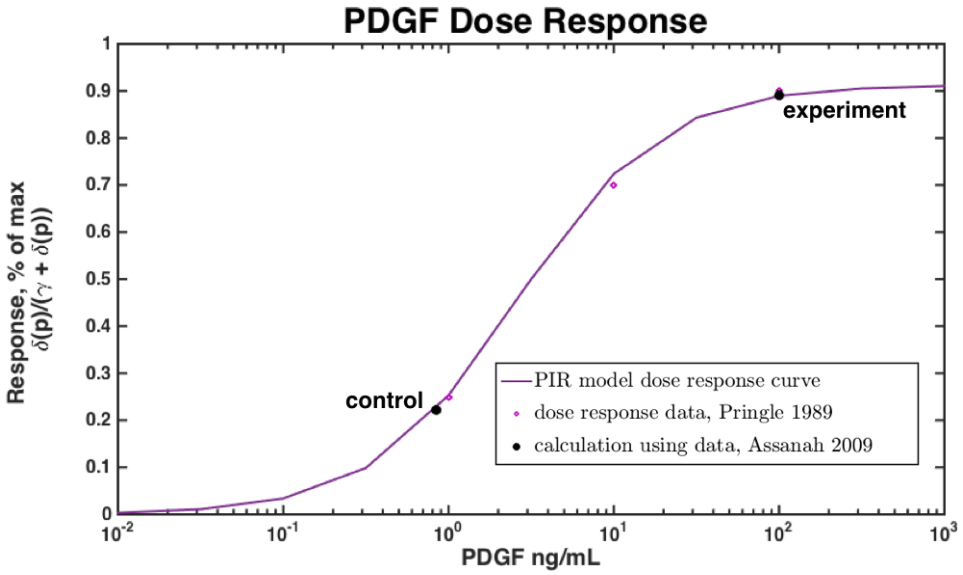

Figure 2.4: **Control and Experimental PDGF concentrations in relation to dose response curve.** Here we have plotted the value computed in section 2.2.2 as corresponding to the PDGF concentration due to wounding (2.20), as well as that for the experiment with 100 ng/mL exogenous PDGF added, on the dose response curve. It is easy to see that the response level of the experiment is four-fold higher than that of the control, as found in [10].

1 cm in diameter, so we have a no-flux boundary at $x = 1$, and the initiating event takes place in the center, at $x = 0$.

2.3 Analysis of the wounding model

In a reaction-diffusion model with two or more species on a finite domain, it is possible for the system to exhibit diffusion-driven instability [76]. Since we have the minimum number of species necessary, we should investigate whether there might be a parameter space for which we could see patterning occur in our model. To do this, we will do a linear stability analysis of the uniform steady state.

2.3.1 Uniform Steady State

To solve for the uniform steady states, we set the temporal and spatial derivatives in the equations (2.1) and (2.2) equal to 0 and solve for the variables, r and p.

Starting with (2.1), and using r^*, p^* to denote the steady state values of our variables, we have:

$$r_t = 0 = \rho_r \frac{\beta(p^*)}{\gamma + \beta(p^*)} r^* \left(1 - \frac{r^*}{K}\right) \tag{2.21}$$

The roots of this equation, given $p^* \neq 0$ are $r^* = 0, K$. For $p^* = 0$, r^* can be anything.

Looking at our other model equation (2.2) for other steady state solutions, we follow the same procedure and look at:

$$p_t = 0 = -q_r r^* \beta(p^*) \tag{2.22}$$

which is true for either $p^* = 0$ or $r^* = 0$. If $p^* = 0$, then r^* can be anything. If $r^* = 0$, then p^* can be anything. Thus, we have infinitely many steady states along the two lines, and write these steady states as $(r^*, p^*) = (r, 0)$ and $(0, p)$.

We also have the $r^* = K$ from the first equation, but in the second, if we have $r^* = K$, then we require $p^* = 0$. Thus, this is not a separate equilibrium solution.

Further, it is important to note that for certain negative values of p (note that these would be nonphysiologic, and are thus not in the model domain for simulations), we could be dividing by a zero and have an undefined solution. These values are at $p = -k_m$ and $p = -\gamma k_m/(1+\gamma)$, as can be seen by setting the denominators of $\beta(p)$ and of the downstream response term (2.15) equal to zero, and solving for p.

Briefly,

$$\beta(p) = \frac{p}{k_m + p}, \tag{2.23}$$

so when

$$k_m + p = 0 \implies p = -k_m \tag{2.24}$$

we have a zero denominator and equations (2.21) and (2.22) are undefined.

Similarly, our response term is

$$\frac{\beta(p)}{\gamma + \beta(p)}, \tag{2.25}$$

so when

$$\gamma + \beta(p) = \gamma + \frac{p}{k_m + p} = 0 \tag{2.26}$$

$$\implies \frac{p}{k_m + p} = -\gamma \tag{2.27}$$

$$\implies p = -\gamma\,(k_m + p) = -\gamma k_m - \gamma p \tag{2.28}$$

$$\implies p + \gamma p = p\,(1 + \gamma) = -\gamma k_m \tag{2.29}$$

$$\implies p = \frac{-\gamma k_m}{1 + \gamma} \tag{2.30}$$

then we have a zero in the denominator and (2.21) is undefined. Again note that $p < 0$ does not make sense physiologically, and we do not encounter any negative values of p during model simulations.

Thus we have nullclines at the following three lines:

$$r^* = 0, \quad r^* = K, \quad p^* = 0, \tag{2.31}$$

and lines of ill-definition at the following two lines:

$$p = \frac{-k_m \gamma}{1 + \gamma}, \quad p = -k_m. \tag{2.32}$$

Using these lines will be useful in the following section when we look at the eigenvalues of the linearized system.

Assuming we stay within the physiologic domain (i.e., $r \in [0, K]$ and $p \geq 0$), we see that there are multiple uniform steady state solutions to the model:

$$\text{Steady State 1: } (r^*, p^*) = (0, p),\ \forall p \geq 0 \tag{2.33}$$

$$\text{Steady State 2: } (r^*, p^*) = (r, 0),\ \forall r \in [0, K] \tag{2.34}$$

the latter of which includes the equilibrium point $(r^*, p^*) = (K, 0)$. For very large initial p_0, we see in the phase portrait that the solution is drawn toward $r = K$, and then to $p = 0$, making this a particularly noteworthy point on the line of equilibrium points $p = 0$.

2.3.2 Linear Stability - Spatially Homogeneous Perturbations

Using the steady states found in the previous section, we can now evaluate the linear stability of the uniform steady state to spatially homogenous perturbations. To do this, we first linearize the equations (2.1) and (2.2) about (r^*, p^*) using the vector

$$\overline{v}(t) = \begin{bmatrix} \hat{r}(t) \\ \hat{p}(t) \end{bmatrix} = \begin{bmatrix} r(t) - r^* \\ p(t) - p^* \end{bmatrix} \tag{2.35}$$

where $\hat{r}(t)$ and $\hat{p}(t)$ are spatially homogeneous perturbations, and where $|\overline{v}(t)|$ is assumed to be small.

Rearranging, we find $(r, p) = (\hat{r} - r^*, \hat{p} - p^*)$ and then substitute this into the model equations (2.1) and (2.2). Collecting terms of order $O(|\overline{v}(t)|)$, this gives us the linearized model equations:

$$\frac{\partial r}{\partial t} = R_r(r^*, p*)\hat{r} + R_p(r^*, p^*)\hat{p} \tag{2.36a}$$

$$\frac{\partial p}{\partial t} = P_r(r^*, p*)\hat{r} + P_p(r^*, p^*)\hat{p} \tag{2.36b}$$

where R and P denote the reaction terms of the model equations:

$$R = \rho_r \frac{\beta(p)}{\gamma + \beta(p)} r \left(1 - \frac{r}{K}\right), \tag{2.37}$$

$$P = -q_r r \beta(p), \tag{2.38}$$

and R_r, R_p, P_r, P_p are the partial derivatives of those, taken with respect to r or p, as indicated:

$$R_r(r^*, p*) = \rho_r \frac{\beta\left(p^*\right)}{\gamma + \beta\left(p^*\right)} \left(1 - \frac{2r^*}{K}\right) \tag{2.39}$$

$$R_p(r^*, p*) = \rho_r r^* \left(1 - \frac{r^*}{K}\right) \frac{\gamma k_m}{\left(k_m + p^*\right)^2 \left(\gamma + \beta\left(p^*\right)\right)^2} \tag{2.40}$$

$$P_r(r^*, p*) = -q_r \beta\left(p^*\right) \tag{2.41}$$

$$P_p(r^*, p*) = -q_r r^* \frac{k_m}{\left(k_m + p^*\right)^2}. \tag{2.42}$$

General solutions to (2.36) have the Fourier spectrum form:

$$\overline{w} \propto \overline{w}_0 \exp\{\lambda t\}, \tag{2.43}$$

where λ is an eigenvalue and $\overline{w}_0$ an eigenvector of the stability matrix A, which is the Jacobian matrix containing the partial derivatives of the reaction terms of equations (2.1) and (2.2), taken with respect to r and p, evaluated at the steady state, (r^*, p^*):

$$A = \begin{bmatrix} R_r & R_p \\ P_r & P_p \end{bmatrix}_{(r^*,p^*)} \tag{2.44}$$

$$= \begin{bmatrix} \rho_r \frac{\beta(p^*)}{\gamma+\beta(p^*)} \left(1 - \frac{2r^*}{K}\right) & \rho_r r^* \left(1 - \frac{r^*}{K}\right) \frac{\gamma k_m}{(k_m+p^*)^2(\gamma+\beta(p^*))^2} \\ -q_r \beta\left(p^*\right) & -q_r r^* \frac{k_m}{(k_m+p^*)^2} \end{bmatrix} \tag{2.45}$$

and satisfies

$$\lambda \overline{w}_0 = A \overline{w}_0. \tag{2.46}$$

In order for nontrivial solutions to exist, λ must satisfy:

$$|A - \lambda I| = \begin{vmatrix} R_r - \lambda & R_p \\ P_r & P_p - \lambda \end{vmatrix} = 0. \tag{2.47}$$

Expanding the determinant, we find

$$|A - \lambda I| = \left(R_r - \lambda\right)\left(P_p - \lambda\right) - R_p P_r \tag{2.48}$$

$$= \lambda^2 - \lambda\left(R_r + P_p\right) + \left(R_r P_p - R_p P_r\right) = 0 \tag{2.49}$$

$$= \lambda^2 - \lambda \operatorname{tr}(A) + |A| = 0. \tag{2.50}$$

Setting this equal to zero and using the quadratic formula, we find the eigenvalues

$$\lambda_1, \lambda_2 = \frac{1}{2}\left[\left(R_r + P_p\right) \pm \sqrt{\left(R_r + P_p\right)^2 - 4\left(R_r P_p - R_p P_r\right)}\right]. \tag{2.51}$$

$$= \frac{1}{2}\left[\operatorname{tr}(A) \pm \sqrt{(\operatorname{tr}(A))^2 - 4|A|}\right] \tag{2.52}$$

Now, when either $Re(\lambda_1) > 0$ or $Re(\lambda_2) > 0$, the uniform steady state (r^*, p^*) will be linearly unstable, since the perturbation $\overline{v}_0 \exp\{\lambda t\}$ grows exponentially with time, diverging

from the steady state. On the otherhand, if *both* $Re(\lambda_1) < 0$ and $Re(\lambda_1) < 0$ the perturbation will decay with time and return to the steady state.

Linear stability, meaning $Re(\lambda_{1,2}) < 0$, is guaranteed if and only if

$$\mathrm{tr}\,(A) = R_r + P_p < 0 \text{ and } |A| = R_r P_p - R_p P_r > 0. \tag{2.53}$$

If we evaluate A at $(r^*, p^*) = (0, p^*)$, then we have

$$A = \begin{pmatrix} \rho_r \frac{\beta(p^*)}{\gamma+\beta(p^*)} & 0 \\ -q_r \beta(p^*) & 0 \end{pmatrix}. \tag{2.54}$$

Thus, this gives

$$\mathrm{tr}(A) = \rho_r \frac{\beta(p^*)}{\gamma + \beta(p^*)} \tag{2.55}$$

and

$$\det(A) = |A| = 0, \tag{2.56}$$

which gives the eigenvalues, using (2.52),

$$\lambda_1, \lambda_2 = \frac{1}{2}\left[\left(\rho_r \frac{\beta(p^*)}{\gamma+\beta(p^*)}\right) \pm \sqrt{\left(\rho_r \frac{\beta(p^*)}{\gamma+\beta(p^*)}\right)^2}\right] \tag{2.57}$$

$$= \frac{1}{2}\rho_r \frac{\beta(p^*)}{\gamma+\beta(p^*)} \pm \rho_r \frac{\beta(p^*)}{\gamma+\beta(p^*)} \tag{2.58}$$

$$= \frac{1}{2} 2\rho_r \frac{\beta(p^*)}{\gamma+\beta(p^*)}, 0 \tag{2.59}$$

$$= \rho_r \frac{\beta(p^*)}{\gamma+\beta(p^*)}, 0. \tag{2.60}$$

We can look at various regions of p, between (and at) the nullcline (2.31) and lines of ill-definition (2.32) $p = 0, -\gamma k_m/(1+\gamma), -k_m$ to see what values the nonzero eigenvalue, λ_1 takes in those regimes:

$$\begin{array}{rcccl} p^* > 0 & \Longrightarrow & \beta(p^*) > 0, \frac{\beta(p^*)}{\gamma+\beta(p^*)} > 0 & \Longrightarrow & \lambda_1 > 0 \\ p^* = 0 & \Longrightarrow & \beta(p^*) = 0, \frac{\beta(p^*)}{\gamma+\beta(p^*)} = 0 & \Longrightarrow & \lambda_1 = 0 \\ \frac{-\gamma k_m}{1+\gamma} < p^* < 0 & \Longrightarrow & \beta(p^*) < 0, \frac{\beta(p^*)}{\gamma+\beta(p^*)} < 0 & \Longrightarrow & \lambda_1 < 0 \\ -k_m < p^* < \frac{-\gamma k_m}{1+\gamma} & \Longrightarrow & \beta(p^*) < 0, \frac{\beta(p^*)}{\gamma+\beta(p^*)} > 0 & \Longrightarrow & \lambda_1 > 0 \\ p^* < -k_m & \Longrightarrow & \beta(p^*) > 0, \frac{\beta(p^*)}{\gamma+\beta(p^*)} > 0 & \Longrightarrow & \lambda_1 > 0 \end{array} \tag{2.61}$$

Of course, when either $p^* = \frac{-\gamma k_m}{1+\gamma}$ or $p^* = -k_m$, then λ_1 is undefined (see (2.24) and (2.30) and surrounding text).

Thus, looking at the nonzero eigenvalue λ_1, we see that the line $r^* = 0$ is stable only for $\frac{-\gamma k_m}{1+\gamma} < p^* < 0$ (which corresponds with the phase diagram drawn with pplane, Figure 2.7, left panel.)

If we evaluate A at the other uniform steady state, $(r^*, p^*) = (r^*, 0)$, then

$$A = \begin{pmatrix} 0 & \rho_r r^* \left(1 - \frac{r^*}{K}\right) \frac{1}{\gamma k_m} \\ 0 & \frac{-q_r r^*}{k_m} \end{pmatrix}, \tag{2.62}$$

and therefore we have

$$\mathrm{tr}(A) = \frac{-q_r r^*}{k_m} \tag{2.63}$$

and

$$|A| = 0. \tag{2.64}$$

Again using (2.52), these give eigenvalues

$$\lambda_1, \lambda_2 = \frac{1}{2}\left[\left(\frac{-q_r r^*}{k_m}\right) \pm \sqrt{\left(\frac{-q_r r^*}{k_m}\right)^2}\right] \tag{2.65}$$

$$= \frac{1}{2}\left[\frac{-q_r r^*}{k_m} \pm \frac{-q_r r^*}{k_m}\right] \tag{2.66}$$

$$= \frac{1}{2} 2 \frac{-q_r r^*}{k_m}, 0 \tag{2.67}$$

$$\lambda_1, \lambda_2 = \frac{-q_r r^*}{k_m}, 0. \tag{2.68}$$

Looking at different regimes of r we see the values taken on by the nonzero eigenvalue λ_1:

$$\begin{aligned} r^* < 0 \quad &\Longrightarrow \quad \lambda_1 > 0 \\ r^* = 0 \quad &\Longrightarrow \quad \lambda_1 = 0 \\ r^* > 0 \quad &\Longrightarrow \quad \lambda_1 < 0 \end{aligned} \tag{2.69}$$

Thus, we have stability along the line $p^* = 0$ only for $r^* > 0$.

It is worth noting that each of these lines of equilibria have zero as an eigenvalue; zero-valued eigenvalues occur only when there is more than one equilibrium solution, and we have infinitely many points that satisfy the condition along the lines $p^* = 0$ and $r^* = 0$.

According to (2.61) and (2.69), we have linear stability to spatially homogeneous perturbations for the steady state (2.34), where $p^* = 0$. Since our initial condition r_0 is positive and (2.13) is an increasing function, we are never near the equilibrium solution at $r = 0$ in simulations, and have that r is strictly positive; therefore, stabilty at this steady state indicates that we have stability for the physiologically relevant model domain.

To illustrate these results, we have drawn a schematized phase diagram (Figure 2.5) and zoomed in on regions of the phase portrait with the software PPLANE (Figures 2.6 and 2.7).

2.3.3 Linear Stability - Spatially Heterogeneous Perturbations

Now that we have examined the stability of the model to spatially homogeneous perturbations, we now turn to the question of whether the uniform steady state that is stable to homogeneous perturbations (namely the equilibria $(r^* > 0, p^* = 0)$) could be driven unstable by diffusion.

To do this, we again linearize the system (2.13), (2.14) about steady state (r^*, p^*), but this time consider the spatially heterogenous perturbations

$$\overline{w}(x,t) = \begin{bmatrix} \hat{r}(x,t) \\ \hat{p}(x,t) \end{bmatrix} = \begin{bmatrix} r(x,t) - r^* \\ p(x,t) - p^* \end{bmatrix}. \tag{2.70}$$

Now our linearized model equations are, assuming a simplified *constant* diffusion coefficient for r,

$$\partial\overline{w}(x,t) = A\overline{w} + D\nabla^2\overline{w}, \tag{2.71}$$

where A is the stability matrix given in equation (2.44) or in expanded form, (2.45).

and D is a matrix containing constant diffusion coefficients of the model

$$D = \begin{bmatrix} D_r & 0 \\ 0 & D_p \end{bmatrix}. \tag{2.72}$$

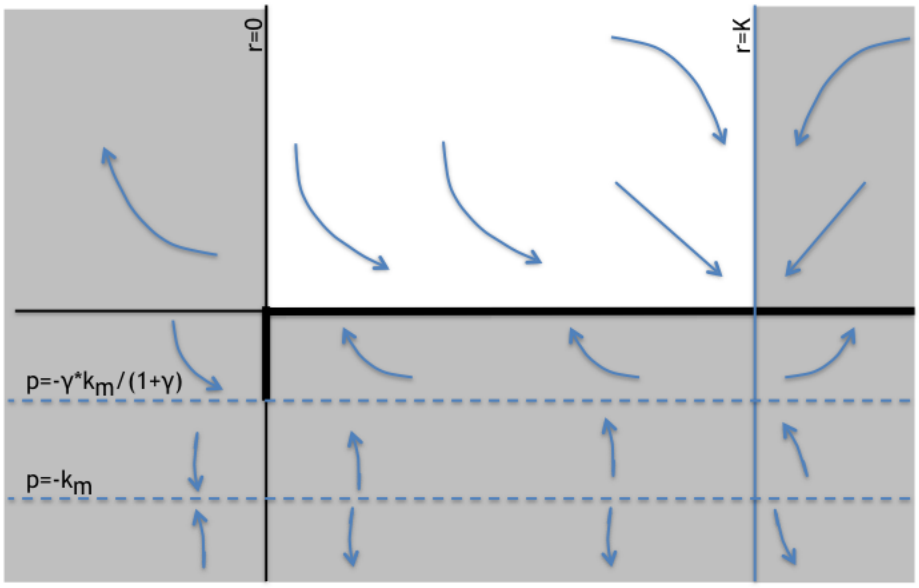

Figure 2.5: **Phase portrait.** Solid black lines represent uniform steady states. The thick black line represent stable steady states; the thinner black lines, unstable. Dashed blue lines represent values of p for which the model is undefined. The gray shaded regions indicate values of r and p that are outside the physiologic domain and includes the values that cause the model to be undefined. The solid blue line indicates the carrying capacity, K, which affects the direction field toward the stable steady state. Blue arrows represent the direction field. The line $p = 0$ for $r > 0$ is the steady state of most interest for physiologically relevant outcomes, since we have $p \geq 0$, and $r_0 \leq r \leq K$, with $r_0 > 0$.

Note that the *constant* D_r here is taken to be the maximum possible diffusion rate in the full model equation (2.13).

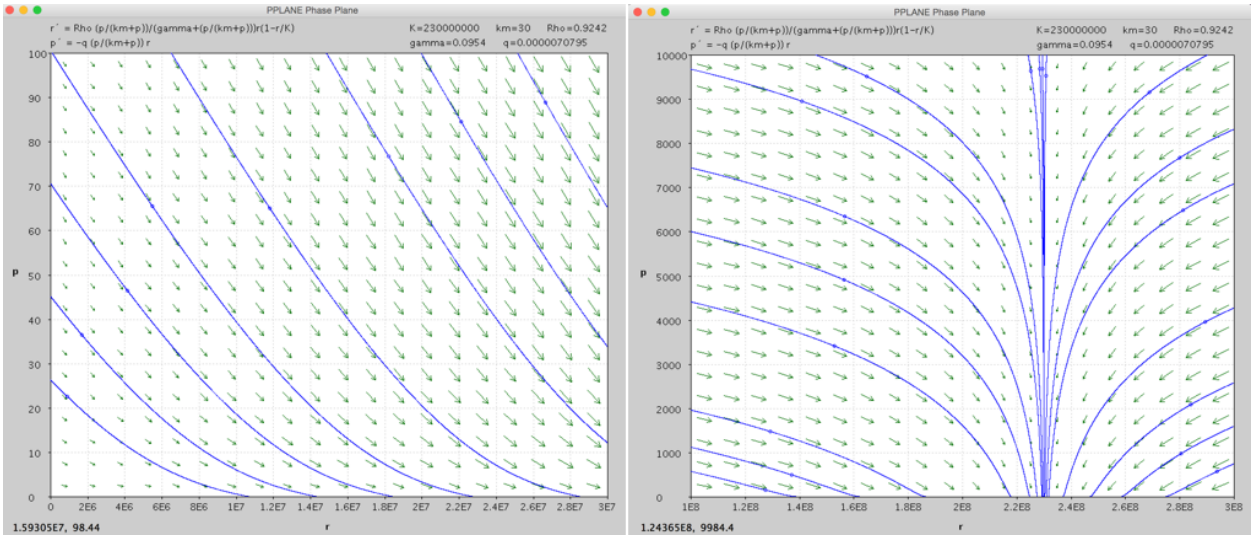

Figure 2.6: **Phase Diagram,** $p \geq 0$**.** These two plots show the phase plane for large p (high levels of PDGF). On the left: for initial positive PDGF, at low to moderate levels, r reaches some larger steady state value, but cannot reach the carrying capacity before the PDGF is depleted ($p = 0$). On the right: for sufficiently large p, the model attracts to $r = K$ (reaches carrying capacity), and then to $p = 0$ (PDGF becomes depleted).

Now, general solutions of the linearized system (2.71) can be written in the Fourier form

$$\overline{w}(x,t) = \sum_k c_k \exp\left(\lambda(k)t\right) W_k(x), \tag{2.73}$$

where the c_k are constants that can be found from initial conditions using Fourier analysis, the eigenvalues $\lambda(k)$ are the linear growth rates of perturbations, and the W_k are time independent eigenfunctions of the model equations.

Now for nontrivial solutions to (2.71) to exist, we must have eigenvalues that satisfy

$$\left|\lambda(k)I - A + Dk^2\right| = 0 \tag{2.74}$$

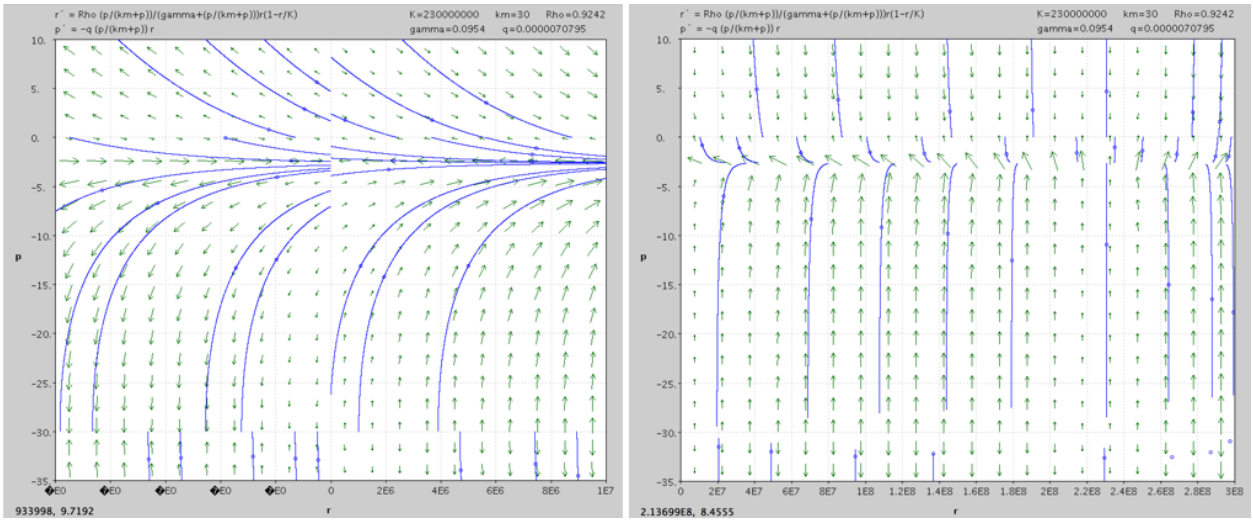

Figure 2.7: **Phase Diagram, $-35 \leq p \leq 10$.** These two phase planes are zoomed in to small p, positive and negative, enabling us to better see what happens near the nullcline at $p = 0$, and lines of ill-definition at $-\frac{\gamma k_m}{1+\gamma}, -k_m$. On the left, $r = 0$ is centered, so can see what happens for $r < 0$; can see that $r = 0$ is stable for $\frac{-\gamma k_m}{1+\gamma} < p < 0$, and unstable otherwise. On the right, $r > 0$, including $r = K$; notice that, given $r > 0$, if p goes slightly negative, it will attract back to $p = 0$, such that $p = 0$ attracts from both sides, so long as $p > \frac{-\gamma k_m}{1+\gamma}$. Since $p < 0$ is nonphysiologic, this is an important result.

Working with the simple version of A (2.44) for convenience:

$$\left|\lambda(k)I - A + Dk^2\right| = \begin{bmatrix} \lambda & 0 \\ 0 & \lambda \end{bmatrix} - \begin{bmatrix} R_r & R_p \\ P_r & P_p \end{bmatrix} + \begin{bmatrix} D_r & 0 \\ 0 & D_p \end{bmatrix} k^2 \tag{2.75}$$

$$= \begin{bmatrix} \lambda - R_r + D_r k^2 & -R_p \\ -P_r & \lambda - P_p + D_p k^2 \end{bmatrix} \tag{2.76}$$

$$\tag{2.77}$$

$$= \left(\lambda - R_r + D_r k^2\right)\left(\lambda - P_p + D_p k^2\right) - R_p P_r \tag{2.78}$$

$$= \lambda^2 + \lambda((D_r + D_p)k^2 - (R_r + P_p)) + D_r D_p k^4 - (R_r D_p + P_p D_r)k^2 + R_r P_p - R_p P_r \tag{2.79}$$

$$= \lambda^2 + \lambda\left((D_r + D_p)k^2 - \mathrm{tr}(A)\right) + D_r D_p k^4 - (R_r D_p + P_p D_r)k^2 + \det(A) \tag{2.80}$$

Since we only had stability for the uniform steady state (2.34) at $p^* = 0,\ r^* > 0$, we will look at A evaluated there (2.62) and its trace (2.63) and determinate (2.64) to evaluate the coefficients. The coefficients then become:

$$\text{for } \lambda^2 : 1 \tag{2.81}$$

$$\text{for } \lambda^1 : (D_r + D_p)k^2 + \frac{q_r r^*}{k_m} \tag{2.82}$$

$$\text{for } \lambda^0 : D_r D_p k^4 + \frac{q_r r^*}{k_m} D_r k^2 \tag{2.83}$$

Letting the coefficient for $\lambda^2 = a$, that for $\lambda^1 = b$, and that for $\lambda^0 = c$, we can use these coefficients in the quadratic formula

$$\lambda_{1,2} = \frac{-b \pm \sqrt{b^2 - 4ac}}{2a}, \tag{2.84}$$

which, since in our case $a = 1$, becomes

$$\lambda_{1,2} = \frac{1}{2}\left(-b \pm \sqrt{b^2 - 4c}\right). \tag{2.85}$$

First, we look at the argument of the square root, inserting our coeffients b and c and expanding:

$$\left((D_r + D_p)k^2 + \frac{q_r r^*}{k_m}\right)^2 - 4\left(D_r D_p k^4 + \frac{q_r r^*}{k_m} D_r k^2\right) \tag{2.86}$$

$$= (D_r + D_p)^2 k^4 + 2\frac{q_r r^*}{k_m}(D_r + D_p)k^2 + \left(\frac{q_r r^*}{k_m}\right)^2 - 4D_r D_p k^4 - 4\frac{q_r r^*}{k_m} D_r k^2 \tag{2.87}$$

$$= \left(D_r^2 + 2D_r D_p + D_p^2\right)k^4 + 2\frac{q_r r^*}{k_m}(D_r + D_p)k^2 + \left[\frac{q_r r^*}{k_m}\right]^2 - 4D_r D_p k^4 - 4\frac{q_r r^*}{k_m} D_r k^2 \tag{2.88}$$

Now, collecting by powers of k:

$$= \left(D_r^2 + 2D_r D_p + D_p^2 - 4D_r D_p\right)k^4 + \frac{q_r r^*}{k_m}(2D_r + 2D_p - 4D_r)k^2 + \left(\frac{q_r r^*}{k_m}\right)^2 \tag{2.89}$$

$$= \left(D_r^2 - 2D_rD_p + D_p^2\right) k^4 + \frac{q_r r^*}{k_m} \left(2D_p - 2D_r\right) k^2 + \left(\frac{q_r r^*}{k_m}\right)^2 \tag{2.90}$$

$$= \left(D_r - D_p\right)^2 k^4 - 2\frac{q_r r^*}{k_m} \left(D_r - D_p\right) k^2 + \left(\frac{q_r r^*}{k_m}\right)^2 \tag{2.91}$$

$$= \left(\left(D_r - D_p\right) k^2 - \frac{q_r r^*}{k_m}\right)^2 \tag{2.92}$$

Finally, we put this argument of the square root back into (2.85)

$$\lambda_{1,2} = \frac{1}{2}\left(-\left((D_r + D_p)k^2 + \frac{q_r r^*}{k_m}\right) \pm \sqrt{\left(\left(D_r - D_p\right) k^2 - \frac{q_r r^*}{k_m}\right)^2}\right) \tag{2.93}$$

$$= \frac{1}{2}\left(-\left((D_r + D_p)k^2 + \frac{q_r r^*}{k_m}\right) \pm \left(\left(D_r - D_p\right) k^2 - \frac{q_r r^*}{k_m}\right)\right) \tag{2.94}$$

$$= 0, \quad \frac{1}{2}\left(-2\left((D_r + D_p)k^2 + \frac{q_r r^*}{k_m}\right)\right) \tag{2.95}$$

$$= 0, \quad -(D_r + D_p)k^2 - \frac{q_r r^*}{k_m} \tag{2.96}$$

Since all our parameter values are positive, and we are looking at the steady state for which $r^* > 0$, then for $k \in \mathbb{R}$, we have one negative real-valued eigenvalue and one zero-valued eigenvalue. In this case, we do not have diffusion-driven instability.

2.4 Simulation Results

We solved the model numerically using the `pdepe` function in MATLAB, on a spherically symmetric domain, using the initial conditions given in 2.2.2. Our time steps were half days, and our spatial steps were $1/375 = 0.0027$ cm, which is equivalent to 27 μm.

There is an 11% increase in cell density directly at the wounding site relative to the baseline level of glial progenitors, as can be seen in Figure 2.8, which is reached by about 5 days after the injury (see Figure 2.9). The increased density near the wound site persists for the remainder of the simulation, which was 50 days; this is consistent with our understanding of gliotic scar formation in the control experiment [9].

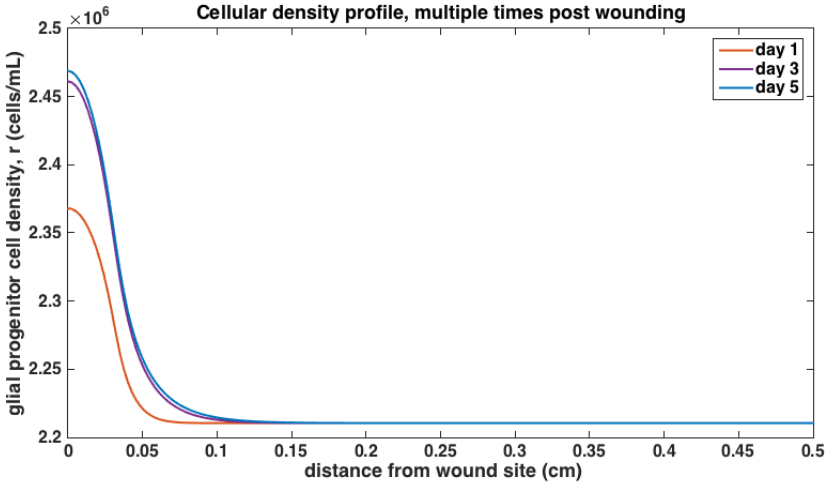

Figure 2.8: **Glial progenitor cells, r vs. brain radius.** Solving the model system numerically and looking at the glial progenitor cell density profile, we find good agreement between the simulation result and the experimental result. The simulated glial scar is less than 0.1 cm, or 1 mm (compare with Figure 2.1, where the scar appears to be about 0.5 mm. The densest region consists of $\approx 11\%$ more progenitor cells than the baseline.

The PDGF level correspondingly shows a rapid drop-off over the first 5 days (Figure 2.11), although at 5 days our model does not show that it is entirely depleted (Figure 2.10). The highest PDGF concentration at 5 days post wounding is $\approx 1.7\times10^{-3}$ ng/mL. Comparing with the dose response curve of the model in Figure 2.4, it is likely that this low concentration of PDGF, while nonzero, is insufficient to recruit further progenitor cell growth through increased cell division and migration. Since we have a large number of progenitor cells, we expect that this level will continue to decrease as those cells consume, but do not respond to, the PDGF.

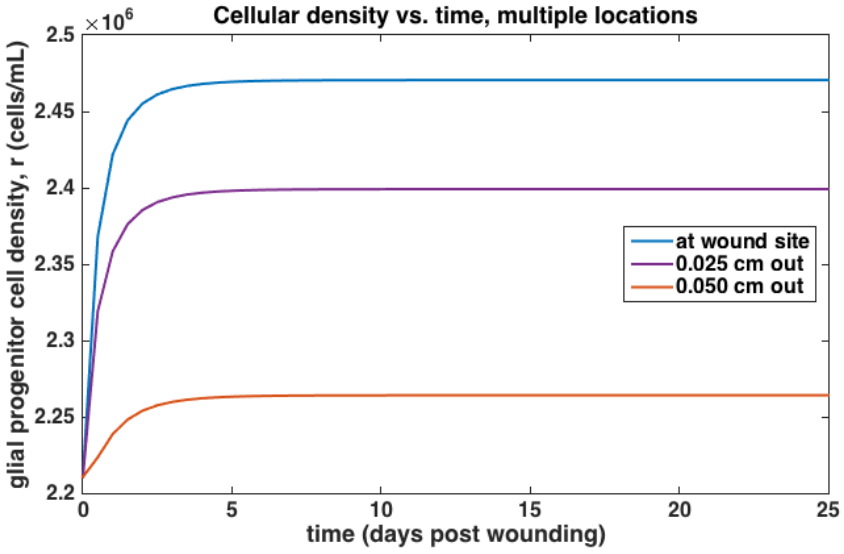

Figure 2.9: **Glial progenitor cells, r vs. time.** The progenitor cell density increases and reaches a maximum by about 5 days post injury at multiple distances from the wound site. This increased density persists for the remaining time of the simulation.

2.5 Conclusions

Our results show that it is possible to capture some of the biological effects of a single release of PDGF on the local tissue, and our very minimal model can describe limited local gliosis. Additionally, if we were stable to spatially homogeneous perturbations but not heterogeneous ones, we would anticipate that pattern formation could occur in the gliotic scar. However, we are unable to meet the conditions for this in any realistic (physiologic) parameter space. This is an uninteresting mathematical result, but is consistent with biological observations.

The relatively quick cessation of cellular recruitment means that the injury response we have modeled will not lead to any tissue pathology such as scarring. While this is a good thing biologically, this also reflects a limitation to our model. Many injury healing processes do in fact lead to pathological outcomes, and we explore this in the succeeding chapter

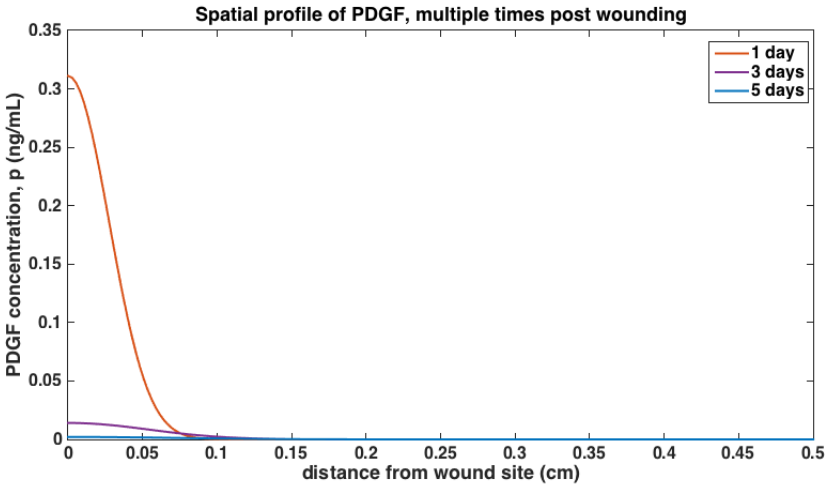

Figure 2.10: **PDGF, p vs. radius.** 5 days after the injury, we see that the highest level of PDGF in the domain is still near the site of the injury, but has spread outward and is a very small concentration $\approx 1.7 \times 10^{-3}$ ng/mL.

(Chapter 3). Further, this model also provides a basis for understanding a somewhat more complex model of PDGF–driven tumor growth in Chapter 4.

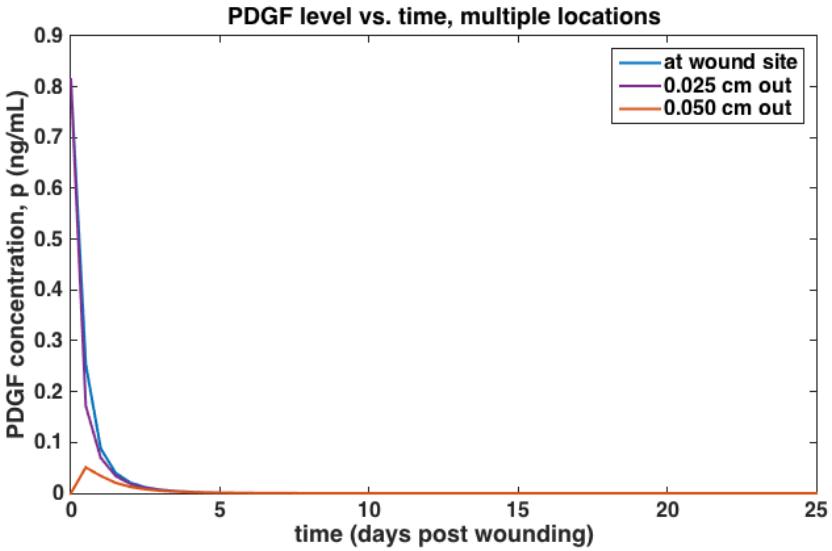

Figure 2.11: **PDGF, p vs. time.** At the wound site, the PDGF concentration decreases rapidly in the first day, and continues to decrease over time, approaching zero. Less is consumed when the concentration is lower, causing the decreased rate of PDGF depletion. Further from the wound site, at 0.05 cm, or0.5 mm, we see the PDGF increase due to diffusion moving the initially released PDGF to that location, and then a similar decrease subsequent to that, as it is taken up by local glial progenitors.

Chapter 3

VARYING PARACRINE PDGF SIGNALING DYNAMICS IN BRAIN TISSUE

This chapter consists of a paper submitted to the Journal of Theoretical Biology in September 2016.

Massey, S. C., Canoll, P., Swanson, K.R. Varying paracrine PDGF signaling dynamics in brain tissue. *Journal of Theoretical Biology*, in review, 2016.

Abstract

Paracrine PDGF signaling is involved in many processes in the body, both normal and pathological, including embryonic development, angiogenesis, and wound healing as well as liver fibrosis, atherosclerosis, and cancers. We explored this seemingly dual role of PDGF mathematically by modeling the release of PDGF in brain tissue and then varying the dynamics of this release. Resulting simulations show that by varying the dynamics of a PDGF source, our model predicts three possible outcomes: (1) localized, short duration of growth, (2) localized, chronic growth, and (3) widespread chronic growth. These results suggest that extended duration of paracrine PDGF signal during normal processes could potentially lead to pathologic conditions.

3.1 Introduction

Platelet-derived growth factor (PDGF) ligands and receptors are expressed by many cell types and are implicated in many processes in the human body—both beneficial and harmful. The cells that can produce PDGF are widespread and include vascular endothelial cells, smooth muscle cells, macrophages, and astrocytes [29, 43, 52, 85]. Cells that express the

receptors for these cells include a number of mesenchymal stem cells and stromal cells such as fibroblasts and oligodendroglial progenitor cells [4, 5, 42, 43, 86]. Because they are frequently found near each other, these two groups of cells, those producing PDGF and those that express the PDGF receptor, can thus communicate with each other in paracrine signaling loops, wherein one cell communicates to another nearby cell. This PDGF signal causes the receptive cells to divide, move, and sometimes differentiate [29, 36, 43]. Through these paracrine loops, PDGF plays a pivotal role in development [14, 45], contributes to angiogenesis and maintenance repair of blood vessels [38, 64], and in the central nervous system stimulates axonal remyelination through the proliferation, migration, and differentiation of oligodendroglial progenitor cells [1,82]. In addition to these beneficial roles, paracrine PDGF signaling is associated with many harmful pathologic conditions. For example, it is involved in the formation of scar tissue, being active in the processes of gliosis [102], liver fibrosis and steatosis [22], atherosclerosis [19, 86], renal diseases [18], and even Alzheimer's disease [66]. Overexpression of PDGF or PDGF receptors has been found in many cancers, as well, including glioblastoma [44, 60, 65, 109, 113], prostate carcinoma [108], chronic myelomonocytic leukemia [6], colorectal cancer [59, 77], and hepatocellular carcinoma [22, 115]. With many studies uncovering stromal involvement in a wide number of cancers [28, 40, 58], it is clear that paracrine signaling has broad importantance for cancer. PDGF is one contributor which we have sought to understand better in the context of cancer, but studying its normal role more fully can arguably give us an even greater picture of how paracrine PDGF signaling contributes to pathologies such as cancer.

Previously, we have explored some of the effects of paracrine PDGF in the brain by creating a mathematical model of PDGF–driven brain tumors, wherein paracrine PDGF drives the recruitment of oligodendroglial progenitor cells (OPCs) to form large, fast-growing tumors [67]. This mathematical model was based on the experimental results of Assanah, et. al. [9], where retrovirally transduced cells secreted PDGF-BB, stimulating the proliferation and migration of oligodendroglial progenitor cells (OPCs), thereby recruiting them to the tumors, which closely resembled human glioblastoma. This is consistent with findings that

OPCs express PDGFRα [81,110]. We modeled the transduced cell population dynamics, as well as that of the responding OPCs and unbound PDGF, and observed that levels of PDGF signal could affect the growth of the tumor, both in terms of size and the steepness of the density profile of invading cells [67,68]. This led us to question the role of PDGF signaling in a broader context. Since PDGF signaling is involved in the stroma of tumors as well as other diseased and normal tissue, we wanted to explore the threshold between these. Specifically, what defines the boundary between a healed wound versus a fibrotic scar or even neoplasia? When does a good thing become bad?

To help answer these questions, we set out to mathematically investigate the dynamics of PDGF secretion and responding cells using a minimal modeling approach that focuses only on the interplay between PDGF and a general target cell population, restricting ourselves to the brain. Our present model is an adaptation of our previous tumor model, wherein the source of PDGF is more nonspecific—we know that a number of cell types release PDGF in response to some stimulus, such as an injury event, but it is variable how much or for how long the cells do so. In reality, this is further complicated by the involvement of other signals, such as proinflammatory cytokines, which can modify PDGF release [48]. However, for the purpose of our present model, we let the PDGF source simply decay over time and set a maximum possible PDGF release amount. By varying these two parameters, we observe a wide array of possible outcomes in terms of the recruitment of cells, from small localized responses that stop growing in a matter of days, to extensive responses that continue growing for weeks.

3.2 Methods

To model the general process of PDGF signaling in the brain, we started with two equations from our prior PDGF-driven tumor model [67]—those describing the dynamics of PDGF and of recruited untransduced OPCs—and generalized them with a few modifications. Arguably the most critical change is that in this model we have a nonspecific localized PDGF source in the equation for PDGF concentration, with a secretion rate that decays over time. The

decay of this secretion activity is indicated by a rate parameter, λ, and through another parameter, S_{max}, we set the maximum value that the PDGF source may secrete. Another notable change is that we do not model any autocrine signaling, only paracrine signaling.

3.2.1 Model Equations

Our model is composed of two coupled PDEs. The first of our model reaction–diffusion equations (3.1) describes the change in PDGF concentration, represented by variable p, as a function of both the diffusion and consumption of PDGF. The second (3.2) describes the change in cell density, represented by variable r, over time and space as a function of PDGF–dependent migration and proliferation.

$$\overbrace{\frac{\partial p}{\partial t}}^{\substack{\text{rate of change of extracellular PDGF concentration}}} = \overbrace{\nabla \cdot (D_p \nabla p)}^{\substack{\text{diffusion of PDGF}}} - \underbrace{\overbrace{q_r}^{\substack{\text{rate of PDGF consumption by PDGFR+ cells}}} \overbrace{\beta(p)}^{\substack{\text{\% of cell receptors bound to PDGF}}} r}_{\substack{\text{consumption of PDGF by PDGFR+ cells}}} + \underbrace{\overbrace{S_{max} e^{-\lambda t}}^{\substack{\text{PDGF secretion dynamics}}} \overbrace{\left(\frac{r - r_0}{K}\right)}^{\substack{\text{location of elevated cells}}}}_{\substack{\text{PDGF source}}} \tag{3.1}$$

$$\overbrace{\frac{\partial r}{\partial t}}^{\substack{\text{rate of change of PDGFR+ cell density}}} = \overbrace{\nabla \cdot \left(\overline{D_r}(r,p) \nabla r\right)}^{\substack{\text{diffusion of PDGFR+ cells, depends on local PDGF concentration}}} + \overbrace{\overline{\rho_r}(r,p)\, r}^{\substack{\text{net proliferation of PDGFR+ cells}}} \tag{3.2}$$

The first term in the right–hand side of equation (3.1) describes the diffusion of PDGF at rate D_p. The second term describes the loss of PDGF due to consumption by the PDGF–responsive cells at rate q_r. This loss is also modified by a scaling term, $\beta(p)$ which defined in equation (3.5) and described in the text that follows the equation. Finally, the third term describes the secretion of PDGF at rate $S_{max} \exp\{-\lambda t\}$, where S_{max} is the max secretion rate. This secretion rate decays over time at rate λ, and we start with a nonzero initial condition for p, since we do not model the inciting event (see section 3.2.3). This whole term is scaled by the ratio of recruited cells to the carrying capacity. In this way, we indirectly capture the effects of other PDGF–secreting cells recruited to the site (by other signaling molecules) which may result in further release of PDGF. Mathematically, this also useful in

moving the source spatially away from its initial point source (see Section 3.2.3 for details about the initial conditions).

In equation (3.2), $\overline{D}_r(r,p)$ and $\overline{\rho}_r(r,p)$ are the diffusion and proliferation rates of the PDGF–responsive cells, respectively, which depend on the local concentration of PDGF, p, and the density of PDGF–responsive cells,r, as follows:

$$\overline{D}_r(r,p) = \overbrace{D_r}^{\substack{\text{max possible}\\ \text{diffusion}\\ \text{rate}}} \overbrace{\frac{\beta(p)}{\beta(EC_{50})+\beta(p)}}^{\substack{\text{downstream effect}\\ \text{of PDGF concentration}}} \overbrace{\left(1-\frac{r}{K}\right)}^{\substack{\text{density}\\ \text{limited}}} \tag{3.3}$$

$$\overline{\rho}_r(r,p) = \overbrace{\rho_r}^{\substack{\text{max possible}\\ \text{proliferation}\\ \text{rate}}} \overbrace{\frac{\beta(p)}{\beta(EC_{50})+\beta(p)}}^{\substack{\text{downstream effect}\\ \text{of PDGF concentration}}} \overbrace{\left(1-\frac{r}{K}\right)}^{\substack{\text{density}\\ \text{limited}}} \tag{3.4}$$

where

$$\beta(p) = \frac{p}{k_m+p}, \quad \beta(EC_{50}) = \frac{EC_{50}}{k_m+EC_{50}}. \tag{3.5}$$

The parameters D_r and ρ_r are the maximum values that can be attained by the diffusion rate and proliferation rate, respectively, when the density is low and the PDGF concentration is high. The scaling terms that implement the dependence on p and r are valued between zero and one, and act to reduce the rates of diffusion and proliferation when there is little PDGF present to stimulate these effects and/or limited space due to high cell density. In the latter, we use use a logistic growth term, $1 - r/K$, where K is the carrying capacity. The PDGF–dependent scaling term is derived in part from Michaelis–Menten binding kinetics, which gives us $\beta(p)$ (3.5). $\beta(p)$ is a direct application of Michaelis–Menten kinetics, where parameter k_m is the concentration of PDGF at which half maximal receptor binding occurs. We also wanted to capture the downstream effect of this bound PDGF on cellular proliferation and movement (downstream in terms of biochemical pathways). This is traditionally done with a pharmacodynamic model and an EC_{50} parameter— that is, the half maximal effective concentration—in place of k_m. To incorporate both the binding of PDGF and the downstream effect of bound PDGF on behavior together in one term, we devised a term that

utilized both parameters and fit the dose response data from [81]. (See Figure 3.1 which shows the curve generated by our downstream PDGF response term in relation to this data, as well as other data that we used for finding our initial condition, which is described in Section 3.2.3.)

3.2.2 Parameters

Most parameters are kept the same as those from the PDGF–driven tumor model (detailed derivation of these may be found in [67] and the associated supplement). Many of these parameters are OPC–specific; however, since we lack experimental data on the other cell types and are grouping OPCs together with other PDGF–responsive cells, we take these values as an approximation for the features of the combined pool of PDGF–responsive cells in our model. Additionally, we have two new parameters—those describing the dynamics of the PDGF source term, λ and S_{max}. There are many interacting components that may affect the secretion of PDGF, which we have not attempted to capture. Rather than describing the process exactly, we sought a simple term with as few parameters as possible that still allow us to capture the varied outcomes corresponding to different PDGF secretion dynamics. Because we have not connected these with distinct biological processes and because we wanted to examine the possibilities of a variety of PDGF signal dynamics, we first varied the two parameters over three orders of magnitude. This then allowed us to hone in on a parameter regime that yielded the most physiological results, which we explore in section 3.3. Parameter values are given in Table 3.1.

3.2.3 Initial and Boundary Conditions

For this model, we assume some arbitrary inciting event, such as an injury, sets everything in motion, causing an initial release of PDGF. We start our simulations shortly after PDGF has started to be released, thus avoiding the complexity of simulating the event itself, and use a nonzero initial condition for the PDGF.

Table 3.1: **Model Parameters and their Values.** Most of these parameters are derived in [67] and its supplemental material, as indicated. (*) Indicated parameters were varied across a range of values to explore their effect on simulation outcomes, as discussed in the results (Section 3.3).

Symbol	Definition	Value	Units	Source
D_r	max diffusion rate of recruited cells	5.8×10^{-5}	$\frac{cm^2}{day}$	[67]
D_p	diffusion rate of PDGF	5×10^{-4}	$\frac{cm^2}{day}$	[67, 105]
ρ_r	max proliferation rate of recruited cells	$\frac{ln(2)}{18/24}$	$\frac{1}{day}$	[67]
q_r	max rate of PDGF uptake by recruited cells	$10^{-5.15}$	$\frac{ng/cell}{day}$	[67]
K	cellular carrying capacity	2.3×10^8	$\frac{cells}{mL}$	[67]
k_m	[PDGF] at which half max binding occurs	30	$\frac{ng}{mL}$	[67, 81]
EC_{50}	[PDGF] achieving half max dose response	$10^{1/2}$	$\frac{ng}{mL}$	[67]
$O2a$	baseline population of OPCs in gray matter	2.2×10^6	$\frac{ng}{mL}$	[67]
S_{max}	maximum PDGF secretion	10 to 100	$\frac{ng/mL}{day}$	*
λ	decay of PDGF secretion	0.01 to 0.1	$\frac{1}{day}$	*

Initial PDGF concentration, p_0

To estimate the value for p_0, we utilize data on the proliferation rates of cells in brain tissue, with and without added PDGF [10]. Briefly, this experiment compares cellular proliferation of cells in rat brain tissue in acute slice culture with added exogenous PDGF (experimental condition), and without (control condition). The harvested tissue (without any added exogenous PDGF) has some level of PDGF due to the injury involved in removing it from the animal. Thus, by comparing the control and experimental conditions, we can estimate the PDGF released by the response to the injury. Specifically, it was observed that adding 100 ng/mL of PDGF to the experimental condition caused an approximately four-fold increase in proliferation rate of OPCs as compared to the control condition.

Interpreting this mathematically, they both start with some baseline amount, which we'll designate with variable p_0. Then the experimental case is given additional PDGF, so that the control has p_0 ng/mL PDGF, and the experimental condition has $p_0 + 100$ ng/mL PDGF. Response is measured in proliferation, a downstream effect of PDGF, so we can use our downstream effect response ratio from equations (3.3) and (3.4), which we write here as

$$R(p) = \frac{\beta(p)}{\beta(EC_{50}) + \beta(p)} \tag{3.6}$$

where $\beta(p)$ and $\beta(EC_{50})$ are given in equation (3.5), and we use the parameter values $k_m = 30$ ng/mL and $EC_{50} = \sqrt{10}$ ng/mL (as given in Table 3.1).

Using this response term in conjunction with the experimental result, we have the relationship

$$R(p_0 + 100) = 4R(p_0) \tag{3.7}$$

which means "the response observed in the experimental case is equal to four times the response observed in the control case." Expanding this relationship using the definition of $R(p)$ in (3.6), we have:

$$\frac{\beta(p_0 + 100)}{\beta(EC_{50}) + \beta(p_0 + 100)} = 4\frac{\beta(p_0)}{\beta(EC_{50}) + \beta(p_0)} \tag{3.8}$$

Through algebraic manipulations (see 3.5 for details), we arrive at a quadratic polynomial in p_0 with the following roots:

$$p_0 \approx 0.8415, -103.45 \tag{3.9}$$

Since the latter of these is non physiologic, we adopt the first root as our approximate value for p_0:

$$p_0 = 0.8415 \text{ ng/mL} \tag{3.10}$$

This computed value for the PDGF concentration in the control condition, and correspondingly the experimental condition, from the experiment in [10] are plotted against the model dose response curve $R(p)$ in Figure 3.1.

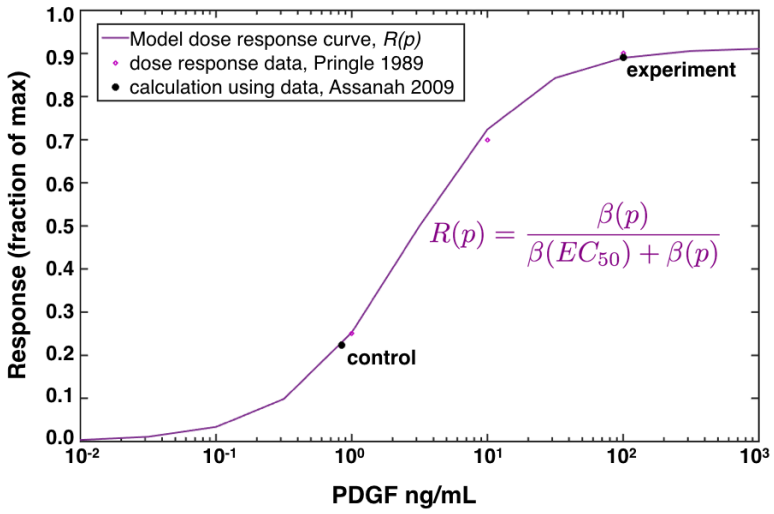

Figure 3.1: **Control and Experimental PDGF concentrations in relation to model dose response curve.** Here we have plotted the value computed in section 3.2.3 as corresponding to the PDGF concentration due to wounding (3.10), as well as that for the experiment with 100 ng/mL exogenous PDGF added, on the model dose response curve. It is easy to see that the response level of the experiment is four-fold higher than that of the control, as found in [10].

Initial PDGF–responsive cell density, r_0

Given that we are pooling a number of different cell populations together for our PDGF–responsive cells, it is a bit difficult to determine the total number of all the cells that are normally present, particularly those in blood vessel walls. However, OPCs have a widespread presence throughout the normal adult brain. In adult humans, glial progenitors have been estimated to have a relative abundance of about 3–4% [79,87,88], or 5–8% of all glial cells [57]. If we assume that 3% of estimated normal cellularity of the brain—which is about 80 million cells/mL averaged across all regions in humans [16]—represent glial progenitors, we arrive at approximately 2×10^6. In rat brain tissue, approximately 250 immunofluorescently labeled

OPCs were counted in a spherical volume of radius 300 μm = 0.03 cm (personal communication from Peter Canoll, June 2008). This gives us $\frac{250}{\left(\frac{4}{3}\right)\pi \cdot 0.03^3}$ cells/cm^3. Evaluating this, and noting that 1 cm^3= 1 mL, we get approximately 2.21×10^6 cells/mL. While this is a bit higher than the other estimate, it is in the same general order of magnitude, and is probably closer to the total number of PDGF–responsive cells which go beyond just the OPCs. Thus, we take 2.21×10^6 cells/mL as a reasonable estimate for the average baseline density of PDGF–responsive cells throughout the brain.

Boundary

We take the whole brain as our domain, and the skull as the boundary, as this best matches the actual biological setting. For simplicity, we simulate the model in one dimension, assuming spherical symmetry. Generalizing the volume of the rat brain to a sphere, we find that it is approximately 1 cm in radius. Thus, our domain is

$$x \in [0, 1], \tag{3.11}$$

where we assume that the injury takes place in the center, at $x = 0$.

Further, we assume that the boundary representing the skull at $x = 1$ allows neither PDGF nor OPCs to leave the brain, giving us a no-flux boundary condition:

$$\begin{bmatrix} \overline{D}_r \\ D_p \end{bmatrix} \nabla \begin{bmatrix} r \\ p \end{bmatrix} \cdot \mathbf{n} = 0, \tag{3.12}$$

where $\mathbf{n}$ denotes the normal vector on the boundary.

3.2.4 Numerical solution.

We solved the model numerically using the `pdepe` function in MATLAB® (MATLAB Release 2015a, The MathWorks, Inc., Natick, Massachusetts, United States), in one dimension on a spherically symmetric domain, using the boundary conditions and initial conditions given in

section 3.2.3. The `pdepe` funtion uses `ode15s` for time integration, enabling it to handle any stiffness from the diffusion terms by adjusting the time step appropriately. In our simulations, we specified solutions to be recorded at time intervals of half days up to $t_f = 250$ days, and our spatial steps were $1/375 = 0.0027$ cm, which is equivalent to 27 μm—slightly more than the diameter of an oligodendroglial progenitor cell. Our codes may be found here: `https://github.com/scmassey/varied_paracrine_PDGF_dynamics`.

3.2.5 Thresholding to look at growth.

In order to measure changes in the growth of lesions comprised of recruited PDGF–responsive cells, we defined a threshold for each simulation to help us identify the "leading edge" of the lesion in a way that would accommodate the wide variation in maximum cell densities attained by the lesions across our simulations. To do this, for each simulation, we first found the maximum cell density at any of the spatial locations of our domain at a later time point (after the cells have had some time to build up):

$$max_r = \max(r(t = 45 \text{ days}, x)). \tag{3.13}$$

Then, we set our threshold to be 50% of the difference between this maximum and the baseline number of cells above the baseline number of the cells:

$$\text{threshold} = 0.5(max_r - r_0) + r_0. \tag{3.14}$$

Using this *threshold* we found the outer most location (recalling that our x domain is a radius) where this value was attained or exceeded at all time points for each simulation, and used this information to make growth comparisons.

3.3 Simulation Results

Model simulations were run across a range of parameter values for the PDGF source term. We varied S_{max}, the maximum level of PDGF secretion, from 10 to 100 ng/mL/day in increments of 10, and varied λ, the decay rate of PDGF secretion activity, from 0.01 to 0.1

days^{-1} in increments of 0.01. The output of these 100 simulations are compared in terms of the growth dynamics of the lesions created by cells responding to the PDGF signal, which were most easily visualized in heatmaps. We also looked at the individual simulations from different regions of the heatmaps to better resolve the indicated differences in these dynamics.

3.3.1 Smaller PDGF secretion activity decay rate, λ, and larger maximum PDGF secretion level, S_{max}, parameters in PDGF source term cause extensive and chronic growth.

For each simulation, we used the technique described in section 3.2.5 to determine the outer edge of the lesion at each time point. Comparing these locations, we found the duration of growth until it was very slow—less than one cell diameter per five days—or when it reached a fatal size, defined as 0.5 cm radius, and display these for all simulations in a heatmap (Figure 3.2A). The lesion radii corresponding to these times are shown in another heatmap (Figure 3.2B). From the heatmap in Figure 3.2A, we observe that for smaller decay rates, λ, in combination with larger maximum value for the source concentration, S_{max}, the resulting higher and persistent PDGF signal causes stimulation of cells for upwards of 40 days. Similar trends are seen in the size of lesions as well in Figure 3.2B, with the larger lesions corresponding to smaller values of the decay rate of secretion activity, λ, and larger values of the maximum PDGF secretion level, S_{max}. It is notable between these two heatmaps that the transition from short growth times to long growth times is more gradual, while that from small radii to large radii is more sharp (compare Figure 3.2A and B).

3.3.2 PDGF secretion activity decay rate, λ, has a more pronounced effect than the maximum PDGF secretion level, S_{max}.

While both the decay rate and maximum level of PDGF source must work in concert to get very large lesions to form, we see that decay rate is more influential on both the overall size of the lesions of PDGF–responsive cells and the length of time for which that distribution expands radially. This can be seen most clearly from the left-most columns of the heat maps, which correspond to smaller decay rates, λ. The lighter shades indicate greater time

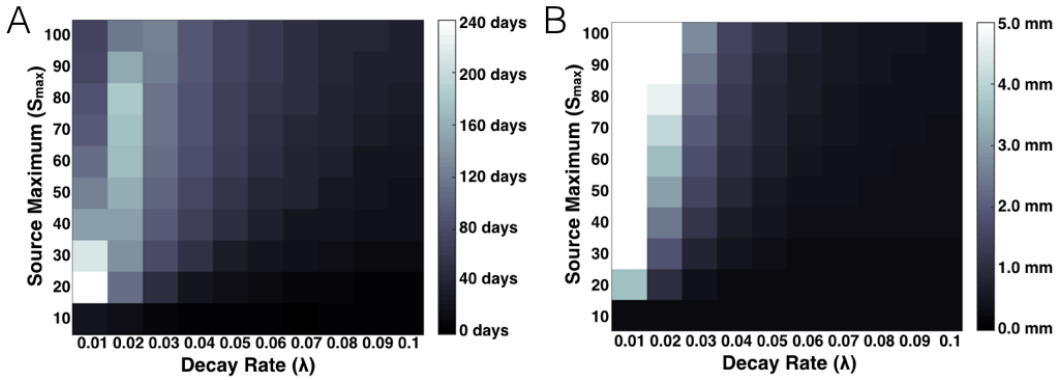

Figure 3.2: **Time elapsed until lesion expansion slows to less than one cell diameter in five days or lethal size reached and corresponding lesion sizes at those times.** Simulations were run across a range of maximum PDGF source (S_{max}) and decay rate (λ) parameters until the outward expansion of the 50% cell density region slows to less than one cell diameter in five days (that is, 10 μm/ 5 days $= 4 \times 10^{-5}$ cm/day), or lethal size is reached (defined as 0.5 cm = 5 mm radius). The length of time until either criterion has been reached for each simulation is given in (A), and the radii of simulated lesions' regions of 50% cell density at these times is shown in (B). Higher values correspond with lighter shades, as indicated by the color axes. Values in (A) that are greater than 40 days indicate *chronic* lesions, and values in (B) that are greater than 1 mm indicate *large* lesions.

duration in Figure 3.2A and bigger radius in Figure 3.2B. These appear to cluster in the three left-most columns for all but the smallest value of S_{max}.

3.3.3 Paracrine PDGF signaling dynamics lead to three possible growth outcomes.

Combining our results together into one picture, we see three growth regimes caused by the PDGF secretion (Figure 3.3). Since experimental models of brain injury response have shown reactive OPCs distributed within 0.3 to 2 mm of the site of injury, with rapid OPC division continuing for seven to 14 days [39,84], we consider active growth continuing beyond

40 days to be "chronic." We also consider lesions larger than 1 mm in radius to be "large," since that is 10% of the brain radius. The lower right corners of the heat maps in Figure 3.2 and the overlaid heatmaps in Figure 3.3A thus correspond to simulated lesions that are small and acute. In the middle of these heatmaps, simulated lesions are small but chronic. And the upper right corner/left–most columns correpond to simulated lesions that are both large and chronic. To see examples of these, we focused on three simulations, one from each of these regions, labeled 1–3 in Figure 3.3A to indicate the corresponding values of parameters λ and S_{max}. We plotted the location of the lesion "edge" (the 50% maximum cell density as computed in section 3.2.5) versus time for three different simulations (Figure 3.3B). These curves are labeled 1–3 to correspond with simulations indicated in panel A. From these curves, it is easy to see that the growth dynamics of simulations in the middle region (labeled 2) are small—not much bigger than that from the lower right region—yet take longer before they stop growing. The curve labeled 3 is much larger, highlighting the sharp transition from small to large lesions indicated by the heat map in Figure 3.2B.

To further illustrate the differences in growth between these three different growth types, we plotted the density of PDGF–responsive cells vs time at the center of the lesion (Figure 3.3C) and vs the radius of our domain at the end of simulation time ($t_f = 250$ days). Thus we see that not only is the spatial extent of the lesions of PDGF–responsive cells larger for the small λ values, but also the density of these lesions is larger. The PDGF levels that the specified parameter values for these three simulations are plotted in Figure 3.4.

3.4 Conclusions

Overall, our results suggest that variations in paracrine PDGF secretion can create very dramatic effects in brain tissue. Modulating this paracrine PDGF signal in simulations, we see three growth regimes, as detailed in results section 3.3.3. In the first, PDGF is released in response to some signal, causing a short burst of growth for PDGF–receptive cells. This growth is limited both in time and in spatial extent. The second involves a longer duration of elevated PDGF signal, causing a corresponding increase in time duration of the PDGF–

stimulation of cell growth. However, the spatial extent of this effect in terms of lesion growth is still limited. Finally, in the third regime, there is sustained PDGF secretion at high levels, causing both long time duration and large spatial extent of lesion growth. These various cellular responses to paracrine PDGF that we observe for the different parameter values suggest possible connections with physiological processes. For example, the first type of PDGF signal and response, with small size and short duration, is similar to what we might see in the healing of a small wound, such as a small brain stab injury or dermal cut. The second, with limited size, but longer duration, is perhaps what we might see with an injury healing process that leaves a scar (localized fibrosis or gliosis). The third regime with its more extreme size and time duration might correspond to PDGF signaling in neoplastic processes.

Notably, there are some findings that support these suggested connections. One study looked at brain stab wounds in rodents and found that measurable PDGF-B was noted around days 3 and 4 post injury and that the spatial distribution of the PDGF matched that of the resulting glial scar [102]. Another recent study found that vascular insufficiency led to *chronic gliosis* in an animal model of brain tissue transplantation [11]. It is quite likely that the sustained levels of angiogenic factors released in response to the insufficiency, including PDGF, caused the recruitment of more than just vascular endothelial and smooth muscle cells, but also oligodendroglial progenitor cells and fibroblasts, which in turn gave rise to the chronic gliosis. Finally, animal studies have shown that increased paracrine PDGF signaling can lead to the formation of tumors that resemble glioblastoma [9, 35], and PDGF signaling has been shown to play a role in human glioblastoma [44, 60, 65, 109, 113].

Our model also suggests that the duration of elevated PDGF signal is generally more impactful than the level of that signal. This suggests that looking upstream at the causes of extended paracrine PDGF signaling maybe more impactful in combacting the potentially ill effects of excessive PDGF signal. Currently, anti–PDGF therapy is aimed at the receptor inhibition level, but these therapies have side effects and have to be given for extended lengths of time. Future modeling work might be best aimed at incorporating the inflammatory

cytokine signaling upstream that can cause secretion of PDGF and understanding how to modulate those signals appropriately.

Since PDGF recruits oligodendroglial progenitors, fibroblasts, and vascular endothelial cells in the brain, there could be implications for angiogenesis and fibrotic changes—i.e., not just the extent of response and its chronicity, but also the "badness" of the resulting affected tissue. Further, it seems likely that similar results may be found for other tissues as well as other growth factors. Recent studies have shown that stromal changes such as fibrosis can drive tumor invasion [28], and there have even been case reports of patients with traumatic brain injuries that years later become sites of glioblastoma, most recently in [107]. These highlight the need to better understand normal stroma function in tissues, and mathematical models further exploring this interplay between a variety of growth factors and stromal cell types could be especially useful for the medical community moving forward. Antiangiogenic therapies (which inhibit growth factor receptors) given to cancer patients have sometimes caused severe side effects, including hypertension, skin lesions, intestinal perforations, hemorrhaging, and even heart failure [25, 33]. On the other hand PDGF and other growth factors given to surgical patients to facilitate healing [5,15,116] could potentially lead to scarring or worse. We are already manipulating PDGF and other growth factors in human patients without fully understanding how to balance its effects—more research is needed to ensure that future growth factor modulating therapies are optimized for patients needs.

3.5 Appendix: Details of derivation of p_0

Recall from Section 3.2.3 that we have the following relationship:

$$R(p_0 + 100) = 4R(p_0) \tag{3.15}$$

which describes the increased activity of one condition of cells that has added exogenous PDGF relative to others that lack this added PDGF. Given that they are still active, and have been injured during tissue removal, we asume that there is a shared baseline amount

of PDGF, p_0.

Expanding this relationship using the definition of $R(p)$ in (3.6), we have:

$$R(p_0 + 100) = 4R(p_0) \tag{3.16}$$

$$\frac{\beta(p_0 + 100)}{\beta(EC_{50}) + \beta(p_0 + 100)} = 4\frac{\beta(p_0)}{\beta(EC_{50}) + \beta(p_0)} \tag{3.17}$$

Since $\beta(EC_{50})$ is a constant, for notational simplicity we set $\gamma = \beta(EC_{50})$ throughout the following algebra. This lets us write

$$\frac{\beta(p_0 + 100)}{\gamma + \beta(p_0 + 100)} = 4\frac{\beta(p_0)}{\gamma + \beta(p_0)} \tag{3.18}$$

Then we can cross multiply the denominators and expand the β terms:

$$\beta(p_0 + 100)\left(\gamma + \beta(p_0)\right) = 4\beta(p_0)\left(\beta(p_0 + 100) + 100\right) \tag{3.19}$$

$$\frac{p_0 + 100}{k_m + p_0 + 100}\left(\gamma + \frac{p_0}{k_m + p_0}\right) = 4\frac{p_0}{k_m + p_0}\left(\gamma + \frac{p_0 + 100}{k_m + p_0 + 100}\right) \tag{3.20}$$

$$\gamma\frac{p_0 + 100}{k_m + p_0 + 100} + \frac{p_0^2 + 100p_0}{(k_m + p_0 + 100)(k_m + p_0)} = 4\gamma\frac{p_0}{k_m + p_0} + 4\frac{p_0^2 + 100p_0}{(k_m + p_0 + 100)(k_m + p_0)} \tag{3.21}$$

Move all terms to one side for simplicity:

$$4\gamma\frac{p_0}{k_m + p_0} - \gamma\frac{p_0 100}{k_m + p_0 + 100} + 3\frac{p_0^2 + 100p_0}{(k_m + p_0 + 100)(k_m + p_0)} = 0. \tag{3.22}$$

Now, multiply both sides by $k_m + p_0$ and $k_m + p_0 + 100$:

$$4\gamma p_0\left(k_m + p_0 + 100\right) - \gamma\left(p_0 + 100\right)\left(k_m + p_0\right) + 3\left(p_0^2 + 100p_0\right) = 0. \tag{3.23}$$

Expanding and then collecting by powers of p_0:

$$4\gamma p_0 k_m + 4\gamma p_0^2 + 400\gamma p_0 - \gamma k_m p_0 + \gamma p_0^2 + 100\gamma k_m + 100\gamma p_0 + 3p_0^2 + 300p_0 = 0 \tag{3.24}$$

$$\left(4\gamma - \gamma + 3\right)p_0^2 + \left(4\gamma k_m + 400\gamma - \gamma k_m - 100\gamma + 300\right)p_0 - 100\gamma k_m = 0 \tag{3.25}$$

$$\left(3\gamma + 3\right)p_0^2 + \left(3\gamma k_m + 300\gamma + 300\right)p_0 - 100\gamma k_m = 0. \tag{3.26}$$

Now we can use the quadratic formula to find the roots of this equation, letting

$$a = 3\gamma + 3 \tag{3.27}$$

$$b = 3\gamma k_m + 300\gamma + 300 \tag{3.28}$$

$$c = -100\gamma k_m \tag{3.29}$$

for the formula

$$p_0 = \frac{-b \pm \sqrt{b^2 - 4ac}}{2a}.$$

Recalling that we use parameter values $k_m = 30$ ng/mL and $EC_{50} = \sqrt{10}$, such that $\gamma = \frac{EC_{50}}{k_m + EC_{50}} = \frac{\sqrt{10}}{30+\sqrt{10}}$, this computes to (in decimal approximation):

$$p_0 \approx 0.8415, -103.45 \tag{3.30}$$

The latter of these does not make sense as a physical quantity, so we adopt the first as our approximate value for p_0:

$$p_0 = 0.8415 \text{ ng/mL}. \tag{3.31}$$

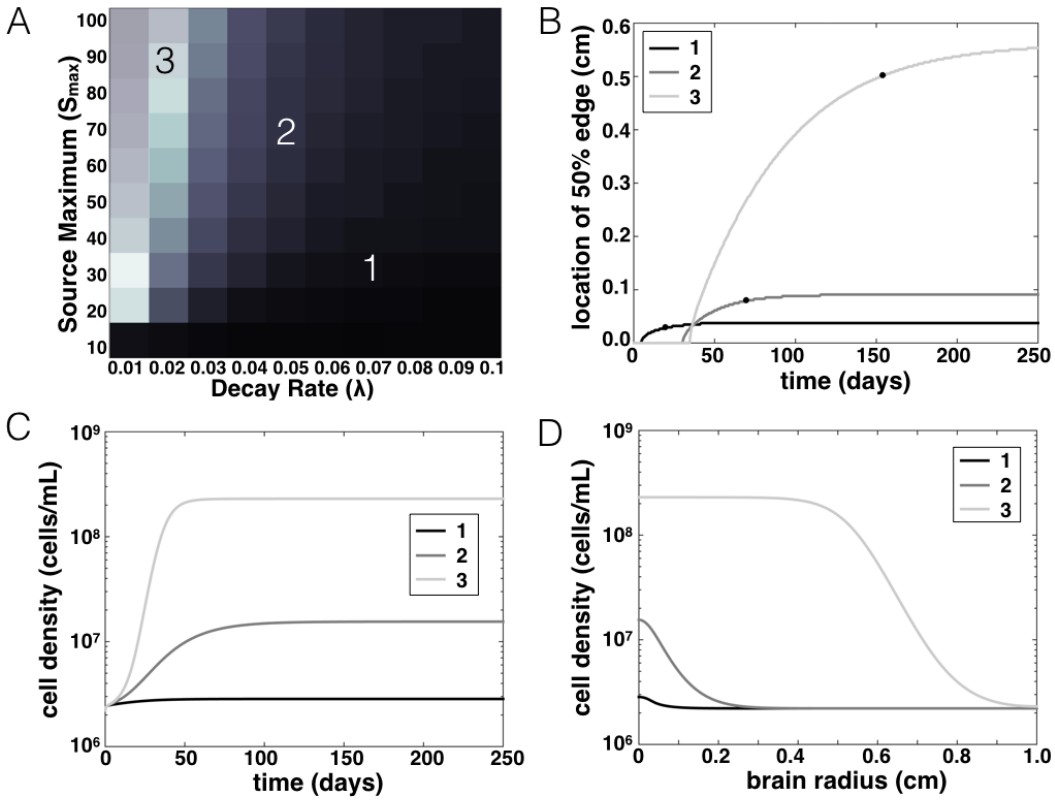

Figure 3.3: **Growth regimes from combined heatmaps.** A. Overlaying the heatmaps of Figure 3.2 create a picture of three growth regimes in our simulations, depending on the PDGF growth parameters: (1) limited growth, short duration; (2) limited growth, long duration; and (3) extensive growth, long duration. The numbered squares correspond to the simulations plotted in panels B-D. B. Curves show the growth of the edge of the 50% cell density region of simulated lesions versus time for three simulations indicated in (A). Black dots show when and what size the simulation was when its growth rate was less than 4×10^{-5} cm/day, or in the case of (3), fatal size was reached. C. Cell density at the center of the lesion (near the inciting event location) versus time, for simulations from the three different growth regimes as indicated in (A). D. Cell denisty at the end of simulation time (250 days) vs radius of the rat brain, our spatial domain, for three simulations as indicated in (A).

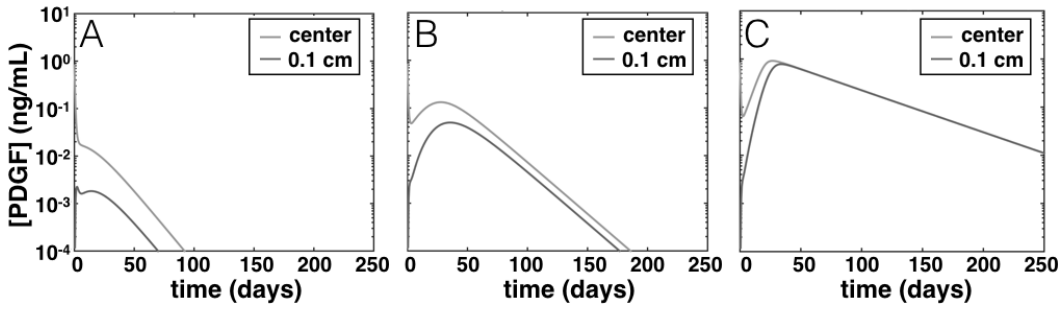

Figure 3.4: **PDGF concentration versus time for multiple simulations.** These curves show the PDGF levels as they change over time at both the center of the domain and at 0.1 cm radius for three different simulation. Notice that PDGF decreases initially as OPCs are recruited to the site and consume PDGF, then it increases, as the uptick in recruited OPCs expands the lesion size and creates inflammatory feedback, increasing the secretion of PDGF. Eventually a a tipping point is reached where the consumption of PDGF by recruited OPCs exceeds the secretion of PDGF, and the PDGF concentration decreases monotonically thenceforth. A. PDGF concentration vs. time from a simulation corresponding with the dark regions of both heatmaps in Figure 3.2A and B (labeled on Figure 3.3D as 1). B. PDGF concentration vs. time from a simulation corresponding with the middle of both heatmaps—midtones in Figure 3.2A and dark in panel B (labeled on Figure 3.3D as 2). C. PDGF concentration vs. time from a simulation corresponding with the light regions of both heatmaps in Figure 3.2A and B (labeled on Figure 3.3D as 3).

Chapter 4

PROLIFERATION–INVASION–RECRUITMENT MODEL OF EXPERIMENTAL BRAIN TUMOR

In the previous section, we discussed the development of a model of brain tissue wounding in rodents. Wounds were the result of injections of a null retrovirus (expressing nothing). Now, we turn to the case where we have a more interesting retrovirus, one that causes the upregulation of PDGF.

This chapter consists of a paper published in the Journal of the Royal Society Interface and the paper's accompanying supplemental material.

Massey, S. C., Assanah, M. C., Lopez, K. A., Canoll, P, and Swanson, K. R. Glial progenitor cell recruitment drives aggressive glioma growth: mathematical and experimental modelling. *Journal of The Royal Society Interface*, 9(73):17571766, 2012.

Abstract.

Currently available glioma treatments remain unsuccessful at prolonging disease-free remission. Recent evidence suggests that tumour recruitment of glial progenitor cells by platelet-derived growth factor (PDGF) may play a role in the development and progression of these tumours. Building upon our recent experimental results and previous proliferationinvasion (PI) reactiondiffusion model, in this study, we created a proliferationinvasionrecruitment (PIR) model that includes a mechanism for progenitor cell recruitment, wherein paracrine PDGF signalling stimulates migration and proliferation of progenitors derived from the local brain environment. Parametrizing this mathematical model with data obtained from the PDGF-driven rat glioma model, we explored the consequences of recruitment, using the PIR model to compare the effects of high versus low PDGF secretion rates on tumour growth

and invasion dynamics. The mathematical model predicts correlation between high levels of recruitment and both increased radial velocity of expansion on magnetic resonance imaging and less diffusely invasive edges. Thus, the PIR model predicts that PDGF levels correlate with tumour aggres- siveness, and results are consistent with both human and experimental data, demonstrating that the effects of progenitor cell recruitment provide a novel mechanism to explain the variability in the rates of proliferation and dispersion observed in human gliomas.

4.1 Introduction.

Gliomas are incurable primary brain tumors noted for their ability to invade neighboring brain tissue, giving rise to diffusely infiltrative lesions that extend beyond the boundaries of radiographically identifiable tumor. Relatively little work has focused on the leading edge behavior of human tumors in vivo, primarily due to the lack of tools to explore these areas of low density invasion through imaging or even histopathology. Given the dominant, perhaps defining, role of these diffusely infiltrating cells in the malignant character of gliomas, combined with emerging data from work in animal models of glioma [9, 10, 35], we propose that the interactions of these diffuse cells with the surrounding tissue is key to understanding how gliomas initiate, form, progress and become fatal.

As with many other cancers, gliomas are rich in growth factors, setting up for autocrine and paracrine signaling loops between tumor cells and the non-neoplastic cells in the local environment [44, 50, 109]. Tumor-induced angiogenesis is a particularly relevant example in which an assortment of growth factors (including VEGF, PDGF, and others) stimulates local vasculature, via paracrine signaling, to expand through vascular cell recruitment [7, 23, 44, 46, 50, 109]. In addition to those directly related to angiogenesis, a variety of growth factors has been found to be over-expressed in gliomas [50] with their level of over-expression generally increasing with grade [109]. Specifically, Majumdar et al. found that expression of PDGF in human gliomas increased with grade [65].

Animal studies have shown that injecting PDGF expressing retrovirus into the brains

of neonatal or adult rodents will induce the formation of gliomas [9, 10, 27, 113] and retroviruses that express higher levels of PDGF drive the formation of more rapidly growing and higher-grade gliomas with robust vascular proliferation and necrosis [44, 55, 90]. Our PDGF-induced animal model exhibits tumor growth that is very consistent (allowing us to collect the dynamic data needed to parameterize our model), and further, it recapitulates the infiltration patterns and histologic features seen in human GBM, in contrast to most xenograft models and C6 glioma cell line models [90]. Most remarkably, tumors induced by high levels of PDGF are primarily composed of recruited uninfected glial progenitors that have been stimulated to proliferate via paracrine PDGF signaling. More recently, Lopez et al. have shown that, when implanted into adult nude rat brains, human primary glioma cells, freshly isolated from glioblastoma specimens, can recruit and stimulate the massive expansion of rodent-derived glial progenitors, providing proof that human glioma cells also have the capacity to recruit progenitors via paracrine signaling [60]. However, the effect that progenitor cell recruitment has on the overall dynamics of glioma growth is not known. To address this question we have developed a novel mathematical model (the PIR model) to explore the consequences of cellular recruitment, focusing on the role of PDGF paracrine signal interacting with glial progenitors, since the recruitment effects of this particular factor have been well-characterized [60].

Human gliomas show a range of growth patterns ranging from well-circumscribed, highly vascularized tumors to diffusely infiltrating lesions with little or no vascular proliferation [61], and little is known about the cellular mechanisms or growth dynamics that give rise to these different histological patterns. Our prior mathematical modeling work focused on the proliferative and migratory contributions of cancer cells to tumor growth, for which the key components are net rates of cellular proliferation and invasion/migration. This Proliferation-Invasion (PI) model has been applied to human glioma patients and has revealed that these different patterns can be well explained by varying only these net rates of glioma cell motility and proliferation [41]. Further, the PI model has been shown to be predictive of prognosis [112], treatment outcome [95,100], and disease distribution observed on autopsy [99], making

the PI model a good base upon which to introduce greater levels of biological complexity, such as glial progenitor recruitment.

Given the evidence in the animal models of Assanah, et al. and Shih, et al. [9, 90], and given that human glioma cells can recruit progenitors [60], it is likely that recruitment is playing a role in human gliomas, though this role and its relevance to the human disease is unclear. Extending the framework of the PI model to investigate the consequences of recruitment enables us to bridge micro- and macroscopic spatial scales, and connect the effects of the cellular level phenomenon with observations at the MRI imaging level (often the only means available to follow glioma in clinic). Through the PI model, we have demonstrated the existence of a range of net proliferation and diffusion rates in human gliomas [41], which have been treated as intrinsic features of individual patients tumor cells. In this present study, we set out to examine and characterize the extent to which adding paracrine-driven recruitment to our established PI model would change the observed growth dynamics, and whether this new Proliferation-Invasion-Recruitment (PIR) model could provide an explanation for the differences in the observed range of net growth parameters (refer to Section 4.2 for PIR model information). Experimental estimations of the model parameters, including observed proliferation and diffusion rates, and validation of the model predictions are provided by the PDGF-driven rat glioma model described in Assanah et. al., 2006 [9].

4.2 Proliferation-Invasion-Recruitment (PIR) Model.

To explore the role of progenitor cell recruitment in the PDGF-driven glioma models (as we have schematized in Figure 4.1A), we have pursued a bio-mathematical modeling strategy that follows the same formalism and retains the key characteristics of our Proliferation-Invasion (PI) model that have been so successfully applied to human and experimental data. These key characteristics include an extensive diffuse invasion pattern and a linear radial expansion pattern seen on imaging (over extended periods of time). We have extended this bio-mathematical model to include interactions with the environment, focusing on the effects of paracrine PDGF stimulation on the glial progenitor population that is widely distributed

throughout the brain. The PIR model provides a tool to examine the effects of paracrine PDGF signaling (Figure 4.1B) on both the composition and dynamics of glioma growth and invasion.

In developing the model, we assume the following about the recruitment process: first, **PDGF-IRES- GFP** infected progenitors (c) secrete **PDGF** (p). Then, **PDGF** can diffuse a short distance into the local environment before binding to PDGF receptors (see Supplement for details on parameterization of PDGF diffusion rate and other model parameters). PDGFR+ glial progenitor cells (including both infected and uninfected PDGFRa+ cells) bind and consume the available free **PDGF**, experiencing paracrine stimulation. The **PDGF** acts as a motogen (D_c, and D_r) and mitogen (ρ_c and ρ_r) for the **retrovirally-transformed** (c) and **recruitable** (r) glial progenitor cells, respectively, in a dose-dependent fashion [7, 10, 81, 110]. In addition, the retrovirally-transformed, PDGF-secreting, glial progenitors experience *autocrine stimulation* by PDGF at a base level ($p_{autocrine}$) above and beyond the free PDGF (p) available to them in the environment, up to receptor saturation. For modeling purposes, $p_{autocrine}$ is a constant, to enable us to focus specifically on the effect of paracrine signaling changes in PDGF (p). Recruited glial progenitors remain dependent on paracrine PDGF stimulation, such that those which have migrated into regions of lower PDGF concentration will show a corresponding decrease in *migration* (D_r) and *proliferation* (ρ_r).

4.3 Simulation Results

4.3.1 Time-lapse microscopy provides a direct measure of cell dispersion ($D_{c,r}$) and proliferaiton ($\rho_{c,r}$).

Estimates of the dispersal parameters (D_c and D_r) of PDGF-secreting and recruited progenitors were obtained from analysis of time-lapse microscopy of these progenitors migrating in acute slice cultures. Focusing on the migration at the infiltrative edge of the tumor (where

there is no necrosis), we plotted individual cell tracks to a common origin (Figure 4.2D), and the mean squared distances (MSD) traveled by the two progenitor types (retrovirally-transformed (c) and recruitable (r) progenitors) were calculated and plotted against time (Figure 4.2C). The slope of the MSD vs. time provides an estimate of the equivalent diffusion coefficient D for each progenitor cell population [89].

Time-lapse microscopy was also effective for obtaining the proliferation rate parameter. This analysis showed that approximately 2% of progenitors at the infiltrative margins of the tumor underwent mitosis every hour (giving a cell cycle time of approximately 50 hours). *In vitro* studies have shown that PDGF stimulated glial progenitors can proliferate with cell cycle times as fast as 10-20 hours [114]. Since our observations were made at the invading edge of the tumor for clearer visualization of individual cells and cellular proliferation rate is dose-responsive to local PDGF levels [81, 110], we have assumed that the longer cycle time is likely due to the decreased PDGF level in this region. The overall result of having such a dose-response relationship is that we have effective proliferation rates that are slower at lower PDGF concentrations and reach maximal proliferation rates only at saturating levels of PDGF, provided there is sufficient space. Details regarding the modeling of PDGF responsiveness to simulate local proliferation and diffusion rates are in the Supplemental Material (Figures S1 and S2), as are those on the parameterization of the proliferation dose-response curve of PDGF (Figure S3).

4.3.2 Radial expansion rates observed on MRI and predicted by the PIR model are consistent with human data.

Gliomas do not have a well-defined outer edge because they are governed by diffusive growth processes [61].Thus, to look at overall tumor expansion in the model in comparison with that observed from imaging studies, we fix a cellular density to approximate the edge of the

visible portion of the tumor on an MRI scan. We used $c + r + n = 0.16K$ for approximating T2, and $0.80K$ for approximating T1gd MRI modalities, as done previously in our simulations of human GBM [61]. Radial velocity measured from human glioblastoma serial MRIs varies from 2-7 cm/year for the majority of patients, with outliers ranging from immeasurably/imperceptibly slow to very fast (10+ cm/year) among different patients, with those patients that have more than two measurement time points maintaining an approximately linear radial expansion [41, 101]. Given this data, we compared the human radial velocities to those obtained from serial MRI of the rat brain and PIR model simulated velocity. Serial MRI data was available for one rat; measurement indicated a linear radial velocity of 62 μm/day, which is equivalent to 2.3 cm/year, for this individual (Figure 4.3). PIR model simulations yield linear radial velocities as well (Figure 4.4C), with those simulated tumors which have no recruitment growing at a rate of about 40 μm/day after initial appearance on MRI, and those with high levels of recruitment approaching an apparent max rate of 85 μm/day (Figure 4.4A). Converting to the cm/ year units used in comparing human glioma velocities, these are = 1.464 cm/yr and 3.11 cm/yr, respectively. Although these velocities are quite fast relative to the size of the rat brain, and thus likely account for their mortality by about day 20, they are on the low end of the human velocity range [41, 101]. These results suggest that differences in the degree to which glioma cells stimulate migration and proliferation of non-neoplastic glia in the surrounding brain tissue can explain the differences in glioma growth rates that have been observed in the human disease.

4.3.3 Paracrine PDGF-mediated recruitment creates a less diffusely infiltrating lesion.

Comparing the distribution of cell densities across the tumor radius at a fixed time (20 days post infection, Figure 4.4C) demonstrated that tumor size is larger for tumors with more recruitment (i.e., higher values of η_c), with the smallest tumor being the case of no paracrine PDGF signal, as expected. However, comparing the distribution of tumor cell densities across the tumor radius for a fixed size on simulated T2 MRI (see Supplemental Material,

for details on MRI simulation) revealed surprising effects on the overall growth pattern. As PDGF secretion rate increases, the slope of the cell density vs tumor curves at the edge of the tumor become markedly steeper, resulting in a more circumscribed, less diffusely infiltrative growth pattern (Figure 4.4B,D). Thus, the model predicts that gliomas with more robust paracrine stimulation of the non-neoplastic glia will develop a more rapidly growing, but less invasive tumor. That is, it has a steeper invasive profile, a result that was not intuitively obvious prior to the mathematical model, which formalizes the consequences of recruitment and specific cell-cell interaction on overall tumor growth.

4.3.4 Paracrine PDGF signaling affects the distribution and growth patterns of infected cells and recruited cells differently.

The difference in infiltration of tumor cells at the leading edge in response to variation in PDGF secretion rate, among tumors of *fixed size* on MRI, is most robust for the PDGF-expressing cells (Figure 4.5A,B). According to the model simulations, higher rates of PDGF secretion (and greater recruitment) result in a smaller margin of diffusing retrovirus-infected progenitors. Specifically, adding recruitment to the PI model results in a steeper cell density distribution (Figure 4.4A,D) that grows more slowly (Figure 4.4A,C). The difference in total tumor radius (including the infiltrating edge) between PI simulations having no PDGF secretion (no recruitment) and the highest rate of secretion (highest recruitment) is 1 mm, or 10% of the approximately 1 cm rat brain radius (Figure 4.5A). The distribution of uninfected glial progenitors responds differently to changes in PDGF secretion rate. High levels of PDGF secretion cause more recruitment, increasing the density of these recruited progenitors at the center of the tumor, but do not alter the radius of this recruited population distribution, which remains constant for a fixed observed tumor size on MRI (Figure 4.5B). Given that external PDGF secretion is required for recruitment to take place in this model, there is no change in uninfected glial progenitor density in tumors with no paracrine signaling component.

At a *fixed time* post infection, higher levels of PDGF secretion cause a drop in infected cell density just beyond the center (Figure 4.5C) that corresponds to an increase in uninfected progenitors in the same region (Figure 4.5D). Thus, according to the model, recruitment causes a region of tumor to fill-up (become more hypercellular) at a faster rate than it would via proliferation of PDGF-IRES-GFP+ infected progenitors alone. For fixed time, both the infected and recruited glial progenitor populations (Figures 4.5C and D, respectively) have a larger radius of infiltration, indicating that both cell types have increased proliferation and migration rates due to increased PDGF secretion. This is expected, since both populations are responsive to paracrine PDGF stimulation.

4.3.5 PIR model confirmation via simulation of fluorescent micrographs.

In Figure 4.6, we used the PIR model to generate simulations and render them as discrete realizations approximating fluorescence microscopy of tumor cross-sections (details are in the Supplemental Material), which we then compared with actual fluorescence microscopy images and data. Using our parameter estimates, we found good agreement between the experimental cell density curve and the model simulation. We calculated the Pearson product moment correlation coefficients between curves of similar cell type to be 0.988 for infected cells, 0.998 for recruited cells, and 0.997 for the normal cells, all of which correspond to p-values of less than 0.0001, with 14 degrees of freedom.

4.4 Discussion.

Our combined experimental and mathematical investigations revealed that the addition of a PDGF-mediated recruitment mechanism to the PI model, with two populations of tumor cells, results in simulated and observed growth dynamics that are consistent with observations of human gliomas. Both the radial expansion velocities and the linear pattern of growth seen at the threshold of MRI-detectability in model simulations are similar to those observed in human serial MRI studies [41, 95, 101]. In combination, these two results provide

additional support to our hypothesis that glial progenitor recruitment plays a role in the progression of human gliomas. Moreover, as with the PI model, the PIR mathematical model makes predictions of tumor cell density and distribution that extend beyond the boundaries detected by MRI.

As a result of recruitment, simulations of tumors varying only the PDGF secretion rate (the mechanism for recruitment), show a wide range of growth patterns. Under conditions with little or no PDGF secretion, simulated tumors exhibited significantly slower yet more diffusely infiltrative growth, reminiscent of gliomatosis cerebri. In contrast, under conditions with high levels of PDGF secretion tumors expanded more rapidly and had increased hypercellularity toward the infiltrative edge (Figures 4.4C,D). Moreover, analysis of human gliomas shows that PDGF levels correlate with tumor grade (higher grade tumors express higher levels of PDGF) [44], and animal model studies using PDGF-expressing retrovirus have also shown that higher levels of PDGF will drive faster growing tumors [90]. Thus, while it is presently not well understood why some gliomas are aggressive and grow rapidly, whereas others grow slowly and do not progress for many years, our results demonstrate that differences in the levels of paracrine PDGF stimulation of recruited glial progenitors provides a possible cause for the observed differences in growth dynamics among human glioma patients [41].

In silico, high levels of PDGF secretion, in combination with recruited cell dependence on PDGF, give a more circumscribed tumor with a cell density gradient that is steeper than without recruitment (see Figures 4.4B,D and 4.5). Additionally, the PDGF-driven increase in migration/invasion appears to contribute to increases in the rate of the radial expansion of the overall tumor (see Figure 4.4A,B). Because both the extent and the rate of tumor invasion are indicative of patient prognosis ([41] and [80, 101], respectively), we hypothesize that more aggressive gliomas are more likely to involve significant recruitment, with greater growth factor upregulation, leading to the steeper invasive profile, greater heterogeneity, and

faster time course to death associated with higher grade gliomas and GBM.

Given the results of this study, we expect that blocking PDGF signaling would lead to slower growth in gliomas expressing PDGF and PDGFR, both through slowing proliferation and migration of tumor cells, as well as inhibiting progenitor cell recruitment. The PIR model suggests that small-molecule targeted therapies which affect paracrine signaling pathways (but not autocrine) would lead to more slowly growing tumors with a more diffuse overall tumor growth pattern (though it would not stop tumor growth, only alter it, since autocrine effects would allow for some proliferation of the infected progenitor cells). Furthermore, this could extend to other paracrine signaling pathways in the glioma microenvironment. Already, clinical trials have shown that treating GBMs with the VEGF-inhibitor Avastin can give rise to recurrence with a very diffusely invasive growth pattern [78]. Together, these results suggest that inhibition of secreted growth factors, such as PDGF or VEGF, can have significant effects on the patterns and dynamics of tumor growth, but will not be sufficient to stop it. However, combining these with other types of therapy, such as inhibitors of glioma cell migration, may have more profound effects on overall tumor growth and survival. Mathematical models, such as the PIR model, can provide a powerful tool to interpret and predict the effects of such combination therapies.

In this context, it should be further noted that recent work by Fomchenko et al. has demonstrated that recruited cells can acquire genetic alterations and become tumorigenic in their own right [34]. In future studies, modeling, such as that presented here could be used to better understand and predict how such complex interactions with the microenvironment can affect the overall growth of the tumor. While the relevance of the PDGF-induced animal model to the human disease is not entirely clear, the PIR model or similar tools that allow for dynamic insight into the interaction of tumor cells with the environment may be critical to developing effective treatment strategies for glioma patients. Future refinements we intend to pursue that would help in this endeavor include adding hypoxia and angiogenesis, and

developing a treatment model to fully understand the role of paracrine signaling inhibitors on the tumor microenvironment. Coupled to this, we would like to explore the outcome of fitting the PI model to MRI data from the rodent model of recruitment, to look for patterns that may predict whether recruitment might be happening in a subset of human glioma patients.

4.5 Methods.

To build the model, we extended the PI model [41] to include recruitment. Note that the PIR model becomes the PI model when recruitment is taken away. Setting PDGF secretion rate η_c to 0 results in a static population of uninfected progenitor cells (r), and the equation for the infected cells, c, with proliferation and invasion terms, becomes the original PI equation. The p remains at its 0 initial condition, reflecting that there is no paracrine PDGF, and causing the population of uninfected progenitors, r, to remain at baseline. The n equation simply continues to keep track of the non-progenitor cells (ie, those normally present cells that we do not consider to be contributing to the tumor in the model), though we have not done this in the original PI model. (Detailed model equations are provided in the Supplemental Material.)

One of the most critical steps in bio-mathematical model development is the inclusion of parameters for which values already exist or can be obtained, in order to ensure that the model has immediate applicability. While the methods of model creation in terms of equations are included in Section 4.2, we present here our methods for obtaining some of the model parameters experimentally, as this was also necessary to complete our model and enabled us to make accurate simulations. (Supplemental Table S1 of parameters and their values, and additional details on parameterization of the biomathematical model, can be found in the Supplemental Material.)

The experimental brain tumors were generated by infecting glial progenitors with PDGF expressing retrovirus and control retrovirus, as previous described [9,10]. The two retroviruses express different fluorescent reporters, allowing us to simultaneously monitor the behavior of PDGF expressing glial progenitor cells (shown as green in Figure 4.2) and recruited glial progenitors (shown as red in Figure 4.2). The tumors that formed were composed of a mixed population of red and green cells, and immunohistochemical analysis showed that both populations express PDGFRa (data not shown). At 10 days post-injection (dpi) animals were anesthetized with Ketamine-Xylazine, decapitated and 300μ m thick coronal brain sections were taken at the level of the injection site and maintained in serum-free medium for the duration of the experiment. Time-lapse microscopy was performed on these acute brain slices using Nikon TE2000 inverted fluorescent microscope equipped with a stage mounted incubator, a digital camera. Images were captured every 3 minutes. The migratory paths of individual RED and Green cells were tracked over the course of seven hours using METAMORPH image analysis system (molecular devices), as described in [10, 12]. We also used time-lapse microscopy to directly monitor the mitotic activity of RED and GREEN cells in the acute slices of the PDGF-driven brain tumors. Proliferation rates were determined by counting the number of tracked cells that underwent mitosis during the course of the time-lapse experiment. As is the case with the analysis of cell migration, the analysis of cell proliferation was limited to cells at the infiltrative margins of the tumor, where the density of retrovirus-labeled cells was low enough to allow for clear visualization of individual dividing cells.

MRI analysis was performed at 5, 10, and 17 days post infection (dpi). Prior to imaging the animals were anesthetized and immobilized in a Plexiglas frame and T2 flair images were collected from a magnetic resonance imaging (MRI) unit with a 1.5 T magnet.

All procedures were approved by the institutional Animal Care and Use Committee of Columbia University, and performed in accordance with the institutional policies.

The authors gratefully acknowledge the support of the McDonnell Foundation (KRS, SCM), the National Science Foundation Graduate Research Fellowship grant DGE-0781824 (SCM), NIH grants R01-NS060752 (KRS, SCM) and U54-CA143570 (KRS, SCM), the University of Washington's Academic Pathology Fund (KRS), and NIH grant K08-NS045070 (PC, MA and KL).

4.6 Supplemental Material

4.6.1 Software used for analysis.

Simulations were executed in Matlab, as follows:
1. set parameter values, initial conditions, and boundary conditions;
2. use Matlab partial differential equations solver (pdepe) to generate simulations of the model with the parameter values, initial conditions, and boundary conditions established in 1; and
3. using standard Matlab plotting routines, visualize and analyze output and plot to display computed results.

Note that for step (2) when numerically solving the model equations, which contain diffusion terms, it is important to ensure that the step size is chosen to be appropriately small in order to avoid getting a negative numerical approximation in the diffusion term (the diffusion coefficient depends on the cellular variables), as this would lead to an ill-posed backwards heat equation. During simulations we altered the tolerance of the solver and confirmed that we did not ever have a negative diffusion coefficient during the iterative solution process (ie, the total cell population did not exceed the carrying capacity see Equations in the section below).

4.6.2 Model simulations of MRI and microscopy to explore consequences of recruitment and examine model fit.

To visualize results in relation to tumor appearance on MRI, we looked at cell densities at and above the thresholds detected by MRI, where 16% of the carrying capacity is associated with enhancement on T2 MRI, and 80% is associated with T1gd [41]. In silico fluorescence microscopy is based on simulation cell densities along the tumor radius at a fixed time. We set the cell radius to 10 μm, and determined the proportions of the various cell types at spatial points along the tumor radius, making the cellular distribution along the circumference at a particular radial distance uniformly random. Both of these techniques allowed us to make comparisons with experimental rat data, and MRI to compare mathematical model data with data from the rat model and from human patients.

4.6.3 The Equations.

The equations for the two progenitor cell types, infected, c, and uninfected recruitable, r, are nearly identical. Their net rates of dispersal, D, and proliferation, ρ, depend on the local concentration of PDGF (p) and the population density of their respective cell types, c or r, (4.1) and (4.2). Note that net proliferation of these cell types is scaled logistically to reflect the limitation of cell division under densities that are near the carrying capacity. That is, when the local cell density ($c + r + n$) nears the carrying capacity of tissue, the net proliferation term approaches zero, as high proliferation rates are countered by proportionately increased cell death due to competition for limited resources. Net dispersal rates are also scaled logistically, in this case to reflect decreased movement in dense regions of tumor.

$$\overbrace{\frac{\partial c}{\partial t}}^{\substack{\text{rate of}\\ \text{change of}\\ \text{infected}\\ \text{cell}\\ \text{density}}} = \overbrace{\nabla \cdot \left(\overline{D_c}\left(c, r, p + p_{autocrine}\right)\right) \nabla c}^{\substack{\text{dispersal of infected}\\ \text{cells, depends on local}\\ \text{pdgf concentration}}} + \underbrace{\overbrace{\overline{\rho_c}\left(p + p_{autocrine}\right)}^{\substack{\text{pdgf dependent}\\ \text{exponential net}\\ \text{proliferation at}\\ \text{low cell density}}} c \overbrace{\left(1 - \frac{c + r + n}{K}\right)}^{\substack{\text{limit net proliferation}\\ \text{when space is limited}}}}_{\text{net proliferation of infected cells}} - \overbrace{\nabla \cdot \left(\overline{\chi}\left(c, r, p\right) \nabla p\right) c}^{\substack{\text{net chemotaxis}\\ \text{dependent on}\\ \text{local cell density and}\\ \text{PDGF concentration}}} \tag{4.1}$$

$$\overbrace{\frac{\partial r}{\partial t}}^{\substack{\text{rate of}\\ \text{change of}\\ \text{recruitable}\\ \text{cell}\\ \text{density}}} = \overbrace{\nabla \cdot \left(\overline{D_r}\left(c, r, p\right)\right) \nabla r}^{\substack{\text{dispersal of recruitable}\\ \text{cells, depends on local}\\ \text{PDGF concentration}}} + \underbrace{\overbrace{\overline{\rho_r}\left(p\right) r}^{\substack{\text{PDGF dependent}\\ \text{exponential net}\\ \text{proliferation at}\\ \text{low cell density}}} \overbrace{\left(1 - \frac{c + r + n}{K}\right)}^{\substack{\text{limit net proliferation}\\ \text{when space is limited}}}}_{\text{net proliferation of recruitable cells}} - \overbrace{\nabla \cdot \left(\overline{\chi}\left(c, r, p\right) \nabla p\right) r}^{\substack{\text{net chemotaxis}\\ \text{dependent on}\\ \text{local cell density and}\\ \text{PDGF concentration}}} \tag{4.2}$$

Our model equation for PDGF, p, accounts for the gross production of PDGF secreted into the extracellular environment at rate η_c, and loss due to consumption through receptor binding and internalization (4.3). We originally included a decay term in this equation, but exploration of the decay rate of PDGF revealed that even setting this value very high (with half-life on the order of approximately one hour) had no observable effect on the simulations of the model. Consumption terms are scaled by the percentage of receptors that are activated by (i.e., bound to) PDGF for each progenitor type depending on the local concentration of PDGF, $\delta_c(p)$ and $\delta_r(p)$, and the number of each cell type, to represent total consumption.

$$\overbrace{\frac{\partial p}{\partial t}}^{\substack{\text{rate of}\\ \text{change of}\\ \text{extracellular}\\ \text{(free) PDGF}\\ \text{concentration}}} = \overbrace{\nabla \cdot \left(D_p \nabla p\right)}^{\substack{\text{dispersal}\\ \text{of PDGF}}} + \overbrace{\eta_c c}^{\substack{\text{gross}\\ \text{production}\\ \text{of PDGF}\\ \text{by}\\ \text{infected}\\ \text{cells}}} - \underbrace{\overbrace{q_r}^{\substack{\text{rate of}\\ \text{PDGF}\\ \text{consumption}\\ \text{by recruited}\\ \text{cells}}} \overbrace{\delta\left(p\right)}^{\substack{\text{percent}\\ \text{receptors}\\ \text{bound}\\ \text{to free}\\ \text{PDGF}}} r}_{\substack{\text{gross consumption of}\\ \text{PDGF by recruited cells}}} - \underbrace{\overbrace{q_c}^{\substack{\text{rate of}\\ \text{PDGF}\\ \text{consumption}\\ \text{by infected}\\ \text{cells}}} \overbrace{\delta\left(p\right)}^{\substack{\text{percent}\\ \text{receptors}\\ \text{bound}\\ \text{to free}\\ \text{PDGF}}} \overbrace{\left(1 - \frac{p_{autocrine}}{k_m + p_{autocrine}}\right)}^{\substack{\text{receptor availability for}\\ \text{binding free PDGF,}\\ \text{depending on autocrine}\\ \text{PDGF signal}}} c}_{\text{gross consumption of PDGF by infected cells}} \tag{4.3}$$

The final equation for the remaining normal (n) cells that are not influenced directly by PDGF is simply a decay term such that as the total local density of progenitors goes up, the density of the normal cells decreases proportionately due to cell death (4.4), reflecting the effects of competition for limited resources.

$$\overbrace{\frac{\partial n}{\partial t}}^{\substack{\text{rate of change}\\ \text{of normal}\\ \text{cell density}}} = \overbrace{-\lambda\left(c+r\right)n}^{\substack{\text{replacement of normal}\\ \text{cells with infected and}\\ \text{recruited olig2+ cells}}} \tag{4.4}$$

Definitions of remaining terms.

The proliferation, diffusion, and chemotaxis terms depend on both free extracellular PDGF, p, and autocrine PDGF (for the infected progenitors), $p_{autocrine}$, as follows:

$$\overbrace{\overline{\rho_c}\left(p+p_{autocrine}\right)}^{\substack{\text{net proliferation rate}\\ \text{of infected cells}}} = \overbrace{\rho_c}^{\substack{\text{maximum}\\ \text{possible}\\ \text{proliferation}\\ \text{rate}}} \overbrace{\left(\frac{\delta\left(p+p_{autocrine}\right)}{\gamma+\delta\left(p+p_{autocrine}\right)}\right)}^{\substack{\text{scaling based on actual percentage}\\ \text{of activated receptors and}\\ \text{downstream PDGF effect}}} \tag{4.5}$$

$$\overbrace{\overline{\rho_r}\left(p\right)}^{\substack{\text{net proliferation rate}\\ \text{of recruitable cells}}} = \overbrace{\rho_r}^{\substack{\text{maximum}\\ \text{possible}\\ \text{proliferation}\\ \text{rate}}} \overbrace{\left(\frac{\delta\left(p\right)}{\gamma+\delta\left(p\right)}\right)}^{\substack{\text{scaling based on actual percentage}\\ \text{of activated receptors and}\\ \text{downstream PDGF effect}}} \tag{4.6}$$

$$\overbrace{\overline{D_c}\left(c,r,p+p_{autocrine}\right)}^{\substack{\text{net diffusion rate}\\ \text{of infected cells}}} = \overbrace{D_c}^{\substack{\text{maximum}\\ \text{possible}\\ \text{diffusion}\\ \text{rate}}} \overbrace{\left(\frac{\delta\left(p+p_{autocrine}\right)}{\gamma+\delta\left(p+p_{autocrine}\right)}\right)}^{\substack{\text{scaling based on actual percentage}\\ \text{of activated receptors and}\\ \text{downstream PDGF effect}}} \overbrace{\left(1-\frac{c+r+n}{K}\right)}^{\substack{\text{scale by available}\\ \text{space in the tissue}}} \tag{4.7}$$

$$\overbrace{\overline{D_r}\left(c,r,p\right)}^{\text{net diffusion rate of recruited cells}} = \overbrace{D_r}^{\substack{\text{maximum possible} \\ \text{diffusion rate}}} \overbrace{\left(\frac{\delta\left(p\right)}{\gamma+\delta\left(p\right)}\right)}^{\substack{\text{scaling based on actual percentage} \\ \text{of activated receptors and} \\ \text{downstream PDGF effect}}} \overbrace{\left(1-\frac{c+r+n}{K}\right)}^{\substack{\text{scale by available} \\ \text{space in the tissue}}} \tag{4.8}$$

$$\overbrace{\overline{\chi}\left(c,r,p\right)}^{\text{net chemotaxis rate}} = \overbrace{\chi}^{\substack{\text{maximum} \\ \text{chemotaxis} \\ \text{rate}}} \overbrace{\left(\frac{\delta\left(p\right)}{\gamma+\delta\left(p\right)}\right)}^{\substack{\text{scaling by actual percentage} \\ \text{of activated receptors}}} \overbrace{\left(1-fracc+r+nK\right)}^{\substack{\text{scale by available} \\ \text{space in the tissue}}} \tag{4.9}$$

where $\delta\left(p\right)=\frac{p}{k_m+p}$, $\delta\left(p+p_{autocrine}\right)=\frac{p+p_{autocrine}}{k_m+p+p_{autocrine}}$, and $\gamma=\delta\left(EC_{50}\right)=\frac{EC_{50}}{k_m+EC_{50}}$.

Since the diffusion coefficients in (4.7) and (4.8) are logistic, and depend on the model cell population variables relative to the carrying capacity, it is important to ensure that when numerically solving the system, the total cell population does not exceed the carrying capacity, as this would result in a negative diffusion term, and thus become an ill-posed backwards heat equation. Physically, it is not possible for cells to exceed the space containing them, which is the basis of the carrying capacity. Additionally, this would not happen when solving the system analytically, using the physically relevant small initial conditions we have used here to represent the actual system (or any initial conditions that do not exceed the carrying capacity, which would not physically make sense). However, it is possible that the approximations to c, r, and n could have a small error that would make them too large, if care is not taken, as discussed in the software used section above.

Dose-responsiveness. Our choice of dose responsiveness to PDGF was due to the observations reported in [7, 81, 110], which demonstrated that glial progenitor cells exhibit increasing proliferation and migration rates under conditions of greater levels of PDGF, in a dose-responsive manner. Furthermore, we have shown that PDGF stimulates both the proliferation and migration rates of tumor cells (pQ-PDGF-IRES-GFP infected cells and uninfected olig2+ PDGFRα+ glial progenitor cells that are recruited) in acute brain slices

[10]. We modeled this PDGF dose-responsive behavior following Michaelis-Menten dose-response kinetics. That is, at the leading edge of the tumor, it is expected that less PDGF will be secreted (due to the small number of infected cells in that region) and, as a result, there will be lower net rates of proliferation and migration for both infected and uninfected glial progenitor cells. To verify that our terms were having the desired effect, we used data on the amount of PDGF at locations and times of interest to visualize the net proliferation and diffusion rates resulting from the amount of PDGF (Figures S 4.8 and S 4.9).

For subplots A and B of figures S 4.8 and S 4.9, note that the cells never actually attain the maximal rates specified by our parameterized values for $\rho_{c,r}$ and $D_{c,r}$, as a result of the dose-response terms. Further, the choice of this term reflects the variation between the effects of low levels of PDGF on net migration and proliferation rates at the leading edge of the tumor (where the time lapse microscopy data was obtained), versus those of high levels of PDGF stimulation in the center of the tumor (where cells were too dense to measure). Looking at the plots in figure S 4.8, we can see that early on, at the center of the tumor (A)and converting net proliferation rate units to cell cycle units under the assumption of minimal cell deaththe cell cycle is about 20 hours (similar to that observed during rat embryonic development [114]. After running simulations to 10 days post infection (B) and looking at 0.15 cm from the center of the tumor (which is the same location and time post infection that was used to make observations of these experimental tumors in a tissue slice), however, has a cell cycle time of about 55 hours (see the description of $\rho_{c,r}$ parameterization in the main text).

In figures S 4.8 and S 4.9, subplots B and D, even though there are very high levels of PDGF, proliferation and diffusion rates toward the center of the tumor are low, due to the effects of extremely high cell density in this region. A cells ability to migrate and proliferate is limited by the availability of resources, including space and nutrients. Under conditions of extreme cell density, there is fierce competition for these resources. Thus, very few would

actually obtain enough resources to display near maximal rates of proliferation and migration. Further out, there is more room and still high levels of stimulation by PDGF, resulting in a peak of attained rates of proliferation and migration that decreases for cells even further away, since while they have sufficient room, they have less PDGF stimulation.

4.6.4 Derivation of carrying capacity,K, and rate of death of normal cells due to tumor expansion,λ.

Assuming the radius of one cell to be 10 μm (which yields a cell volume of approximately $4.189 * 10^3$ μm^3), we have at most $K = (\frac{1 \text{ cell}}{4.189*10^3 \mu\text{m}^3} * (\frac{10^4 \mu\text{m}}{1 \text{ cm}})^3 = \frac{1 \text{ cell}}{4.189*10^3 \mu\text{m}^3} * \frac{10^{12} \mu\text{m}^3}{1 \text{ cm}^3} = \frac{2.39*10^8 \text{ cells}}{1 \text{ cm}^3}$, or, since 1 mL = 1cm^3, $K = 2.39 * 10^8$ cells/mL in the tissue.

The rate of death of the normal brain cells, λ, was chosen to be the inverse of this, per day, giving a death probability of 100% when $c + r$ is equal to the carrying capacity, K, and one that is small for $c + r$ that is much smaller than K (such as for r_0, the initial population of glial progenitor cells); units of "per day" chosen to correspond to the time units of the model.

4.6.5 Model parameterization: k_m and EC_{50},PDGF concentrations inducing half-maximal receptor activation and downstream effects, respectively.

Referring to data in [81], we derived our values for the PDGF concentration at which half-maximal receptor activation occurs using the $EC_{50} = 10^{1/2}$ (reported in the dose-response curve of progenitors incorporating BrdU in [81]). We then simulated the experiment done by Pringle, et al. [81], for various values of k_m, which altered the steepness of the doseresponse curve. The simulated curve that best fit the data (by nonlinear least squares) for PDGF-BB in [81] corresponded to a k_m of 30 ng/mL.

4.6.6 Model parameterization: D_p, diffusion of extracellular PDGF.

Our value for the net PDGF diffusion rate came in part from the values for diffusion of EGF and albumin in rat cortical slices, which were 0.0448 cm^2/day (converted from $5.18 * 10^{-7}$ cm^2/s, in [105] and 0.015 cm^2/day for bovine albumin [103]. This gave us an approximation for parameter D_p, around which we varied the value a few orders of magnitude above and below. Since we assume that p is consumed very quickly due to being in a region dense with cells expressing PDGFRs, we reason that net diffusion of PDGF would appear slower than it would in a tissue with fewer receptors and cells to consume the growth factor. In particular, the tumor is on a spatial scale of millimeters, with amount of to time diffuse out of the local tissue on the order of hours or days, while spacing between cells is on the scale of micrometers. Thus, we suppose that the likelihood that much PDGF would diffuse out of the bulk of the tumor rather than interacting with a receptor is low overall. Additional binding of PDGF to extracellular matrix could further decrease the apparent diffusion coefficient. At lower levels, D_p did not play a large role in determining the outcome of our model, so we primarily focused on a value that was of reasonable magnitude and was not so low as to result in numerical instability (as was the case for values of D_p lower than $5.0 * 10^{-4}$ cm^2/day) when solving the model equations. Since this parameter does influence the dynamics of the model, further experimental work to better determine this value could improve model accuracy.

4.6.7 Model parameterization: χ, rate of chemotaxis.

Numerous studies have evaluated chemotaxis of cells in the presence of PDGF [7,36,106,117]. It is clear from these studies that PDGF has a chemotactic effect; however, we were not able to experimentally distinguish between chemotactic and diffusive movement of the cells. Therefore, we minimized the effect of chemotaxis in the present investigation. The windrose

plots from cell tracking data are consistent with diffusive movement, so we allowed this to dominate the movement of cells in the model.

In the near future, we hope to better understand the different contributions of the two types of movement, through simulating tumors on a 2D mouse brain map using the CLAWPACK software package. This has allowed us to implement a Strang splitting and numerically solve the advective chemotaxis component of the model using flux differencing. This work is still on-going.

4.6.8 Model parameterization: PDGF production rate, η_c, level of autocrine PDGF signal, $p_{autocrine}$, and consumption rates by both PDGF-IRES-GFP+ infected cells, q_c, and uninfected glial progenitor cells, q_r.

Our estimates of the rates of PDGF secretion and consumption were made in the following manner. We began by making the simplifying assumption that the rate PDGF consumption in paracrine loops for both infected and uninfected glial progenitors (q_c and q_r, respectively) is the same. This is reasonable given that their only difference is the PDGF-expressing retrovirus, and at this time biological data does not exist to indicate that it affects consumption of PDGF differently from a non-infected glial progenitor.

We obtained the net rate of PDGF accumulation into the media from experiments with confluent PDGF-IRES-GFP+ cells over 24 hours [9]. We estimated that this value of 29.2 ± 7.4 ng/mL to be approximately equivalent to 10^{-7} ng/cell/day, using our value for carrying capacity K. Since we do not have methods for measuring the gross rate of PDGF secretion (η_c)–this is something that needs to be developed–we varied this value over several orders of magnitude, using values that are not inconsistent with the measured accumulation of PDGF in confluent dishes. This also served as a means of understanding the effects of recruitment. Picking one possible gross secretion rate (choose $\eta_c = 10^{-5}$) of them, , only the PDGF consumption rate and the level of autocrine signal ($p_{autocrine}$), remained to be determined.

Varying these two parameters with all the others fixed, we compared the resulting simulation outcomes with empirical data from the experimental rat model. That is, we matched the simulated size on MRI and the radial velocity of total tumor cells (both PDGF-IRES-GFP+ and uninfected glial progenitors) determined by the model (resultant from varying these two parameters) to the spherical radius and radial velocity derived from measurements of T2 flair MRI images of one rat at days 5, 10, and 17 post infection with the retrovirus (see Figure 4.3 in the main text).

This last component of parameterization is not without pitfalls. Note that only one rat had MRI imaging done in this study, and that this rats tumor grew more slowly than was observed on average. Furthermore, as a result of this parameter fitting, PDGF levels in simulations accumulate far above k_m and persist at these high levels in the center of the tumor. While the normal concentration of unbound PDGF in the extracellular space is not presently known, these simulated levels are much higher than we expected, given that the k_m is only 30 ng PDGF/mL of extracellular space. Since the attained in silico concentration of PDGF can be well above saturating levels, much of this additional PDGF does little to increase the net diffusion and net proliferation rates displayed by the cells. That is, the tumor could persist in similar growth patterns at PDGF amounts below these high levels. Thus, in further experimentation, MRI data from more rats is indicated to facilitate more thorough estimation of these parameters. Additionally, more knowledge about possible PDGF receptor upregulation and PDGF degradation in brain tissues, as well as techniques to evaluate the actual concentration of PDGF in extracellular space, would aid in the verification or improvement of the model, ensuring that the source and sink of PDGF into and out of the extracellular space is properly accounted for.

4.6.9 Source for initial conditions.

Our values for the initial density of total cells (which is expressed as 35% of the carrying capacity) and total glial progenitors come from cell counting data from a sample region of tissue that was in a $\frac{4}{3} * \pi * 0.03^3$ mL volume . From the experimental model, we counted that about 250 cells were transduced (expressed GFP), in a sphere of radius 300 μm = 0.03 cm. Studies revealed that the virus infected cells within a 300 μm radial sphere (surrounding the point of injection), with more than 90% of the glial progenitors in this region being infected. We ran simulations with this varying from 90 to 99%, and the results best matched the MRI data (in terms of size at the 5, 10, and 17 day appearance) when using 99% of glial progenitors infected inside this volume. Given that we assumed a high efficiency of infection (i.e., that almost all of the glial progenitors in that region were infected with the virus), we extrapolated this as the approximate number of glial progenitors in the white matter. As shown in the Parameter Table S1, this value is 250 cells per $\frac{4}{3} * pi * 0.03^3$) volume of the 0.03 cm radius sphere in $\text{cm}^3 = 2.2105 * 10^6$ cells/cm^3. Moreover this corresponds fairly well with some of the literature which give various quantifications of the normal density of glial progenitors in adult humans. Roy et al. give an upper limit of 4% of adult human white matter, and Nunes et al. give a value of approximately 3% of adult human white matter being progenitors [79, 87]. Taking a different approach, Rhee et al. estimate the number of glial prognitors in the adult human non-neoplastic brain parenchyma to be 10 million [83]. If we let 3% of our estimate for the normal cellularity of the brain represent glial progenitors, we also arrive at approximately $2 * 10^6$. The model simulates the case for rat however, so we would stress that this is not a rigorous derivation but was used to give an order of magnitude. Further work would need to be done to determine this value in the rat brain and corroborate what we observed with counting GFP expressing cells shortly after infection.

The number of initial "normal" cells (n_0) is simply the difference between the value of the initial density of total cells and the initial number of glial progenitor cells. Since our model

is initiated by infection we assume that at time = 0, c_0 the initial number of infected glial progenitors is equal to 0.99$*$ the total number of glial progenitors inside the 300 μm radius sphere, and 0 outside that sphere. The remaining glial progenitors that are not infected give the initial condition for the uninfected glial progenitors, r_0.Lastly, since the usual amount of PDGF in the extracellular space of healthy brain tissue is presently unknown, we chose to set this value to zero, basing this estimate on the apparent absence of proliferation and diffusion of glial progenitors in healthy brain.

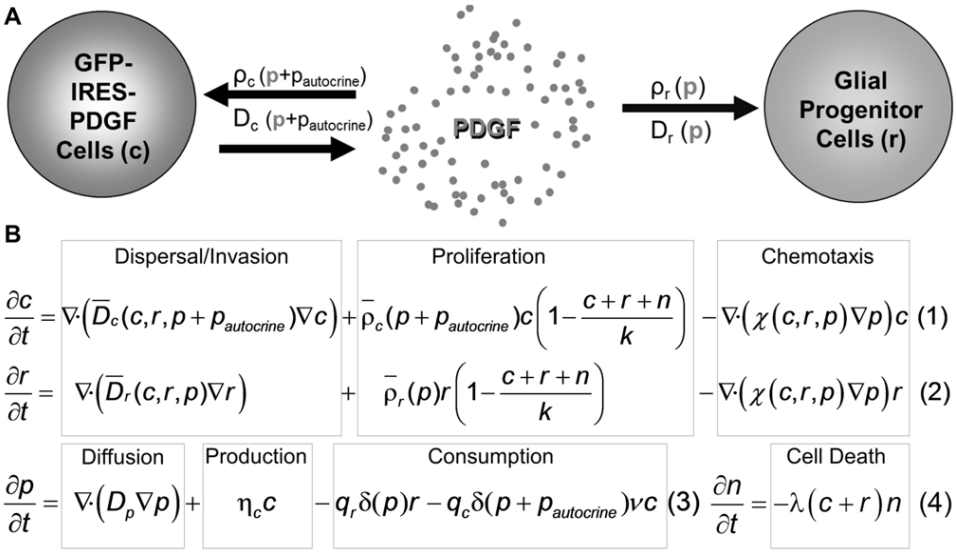

Figure 4.1: **PIR Model. A. Model Schematic.** The flow chart shows the main components of our model: c, the population of glial progenitor cells that are infected with PDGF-expressing retrovirus, r, the glial progenitors that are recruited and do not have the retroviral infection, and p, the free PDGF in the extracellular space (ECS). An injection of the retrovirus initiates the c population. These cells secrete p at rate η_c into the ECS, and p is, in turn, taken up and consumed by the c and r populations at rates q_c and q_r, respectively. Uptake of p by c and r results in increased cellular proliferation (ρ_c and ρ_r) and dispersal (D_c and D_r) in a dose-dependent manner. In addition to the paracrine stimulation from p, the infected c cells experience autocrine PDGF stimulation in concentration $p_{autocrine}$. **B. Model Equations.** The equations for the infected (c) and uninfected recruitable (r) progenitor cells account for the movement and growth of the respective cell populations. Their rates of diffusion and proliferation, D and ρ, depend on the local concentration of PDGF (p) and population density (Eqn. 1 and 2). Eqn. 3 accounts for the secretion of PDGF (p) into the extracellular environment at rate η_c, and loss of p due to consumption by c and r cells at rates q_c and q_r, respectively, scaled by the percentage of PDGF receptors that are activated (δ), and, for infected progenitors only, the percentage of receptors that are not already in use for autocrine signaling, but rather are available for binding free PDGF, ν. The final equation for the remaining brain cells (n) (which includes neurons and other white matter cells) reflects their proportionate decrease in local density via cell death, as those of c and r increase and fill the available space (Eqn. 4).

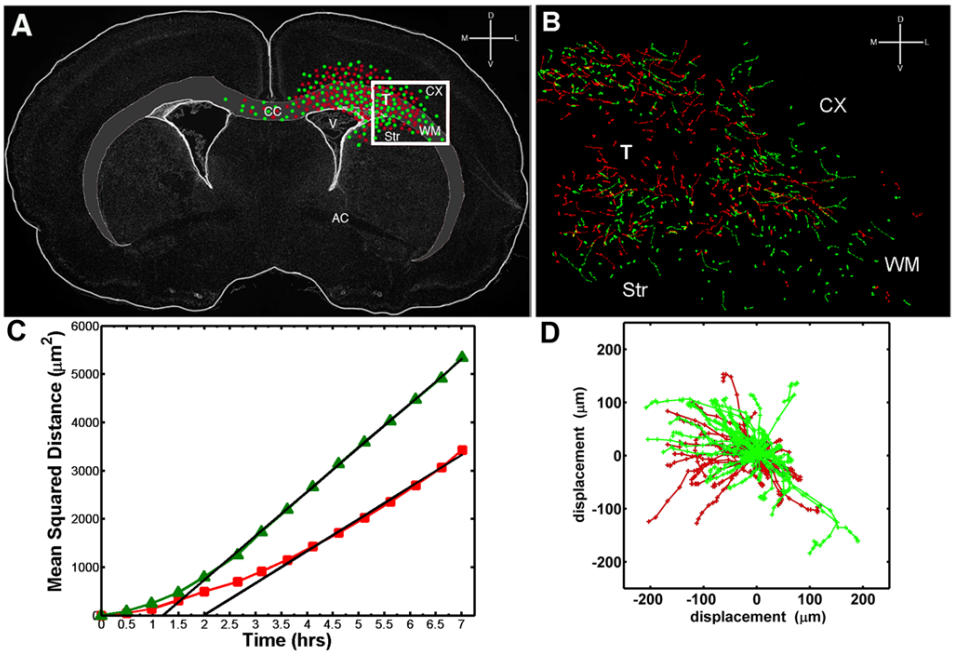

Figure 4.2: **Tracking the migration of PDGF expressing and recruited progenitors by time-lapse microscopy.** 300 μm thick slice cultures were generated at 10 days post co-injection with PDGF expressing retrovirus and control retrovirus and 2 color time-lapse microscopy was performed for 7 hours to monitor the migration of PDGF expressing cells and recruited progenitors. The migratory paths of individual cells was tracked using METAMORPH image analysis system. **A.** A schematic representation of the coronal brain slice showing the tumor location and the distribution of PDGF expressing cells (green dots) and recruited progenitor cells (red dots). The box represents the region of the slice that was filmed by time-lapse microscopy (T=tumor, CX=cortex, WM=white matter, CC=corpus callosum, Str=striatum). **B.** The green and red lines represent the migratory paths of PDGF expressing cells (green lines) and recruited progenitors (red lines). **C.** Mean Squared Distance traveled by the PDGF expressing cells (green lines) and recruited progenitors (red lines). **D.** Windrose plot showing the tracks of cells from (B) plotted with a common origin.

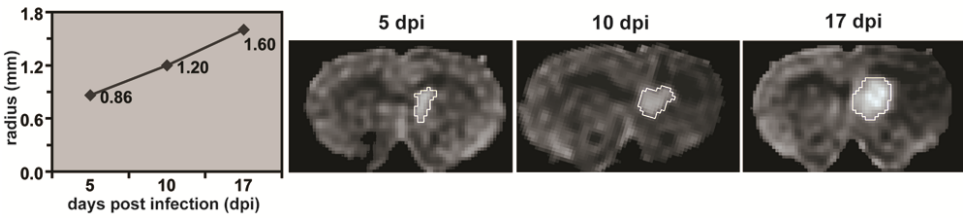

Figure 4.3: **Serial FLAIR MRIs** showing growth of PDGF-IRES-GFP induced rat tumor with a linear radial expansion rate of approximately 62 μm/day (or 2.3 cm/yr), which is consistent with the velocities observed in humans (3).

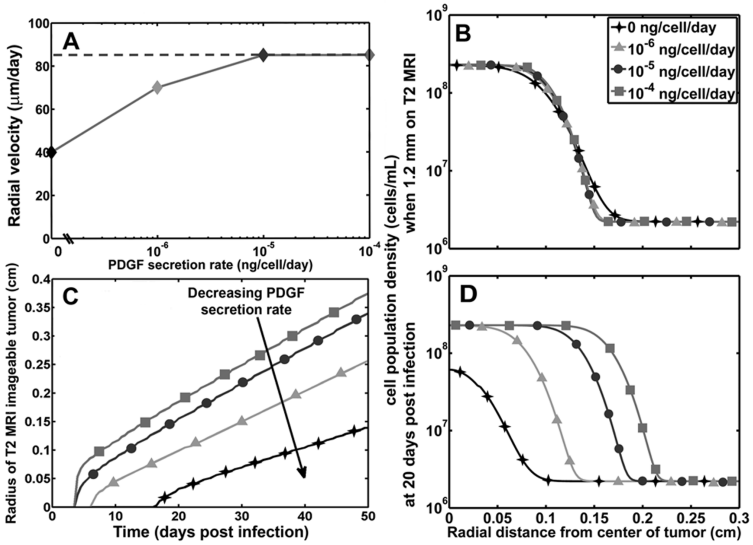

Figure 4.4: **Variations in net PDGF secretion rate alter tumor growth pattern and rate. A.** Radial velocity given by the rate of radial tumor growth on simulated MRI. The dashed gray line (at approx. 85 μm/day) indicates the observed threshold of maximum radial velocity attained for model simulations. A PDGF secretion rate of 0 ng/cell/day indicates that no recruitment can happen; a rate of 10^{-5} ng/cell/day was measured experimentally. Notably, our data indicate that recruitment does not lead to infinitely increasing radial growth, but rather, is consistent with human GBM dynamics. **B.** When the simulated tumors reach a certain fixed size on MRI, the slope of the true edge of the tumor varies with the rate of PDGF secretion. Increased secretion results in a steeper edge, indicating a somewhat less infiltrative edge at higher levels of paracrine PDGF signaling. While this is subtle, the edge of the tumor (that is, the region spanning the point from where the cell density drops from its highest level to the point it reaches its lowest) spans a full 1.5 mm for the tumor with no paracrine PDGF signaling, while that of the highest paracrine signaling spans only 0.75 mm, cutting this region in half. **C.** Plot of the T2 MR-imageable tumor radius vs. time shows that within 3 days of initial appearance on T2 MRI, tumors reach and maintain linear radial expansion, regardless of the degree of recruitment taking place in these tumors. **D.** Looking at the same set of tumors as in (B) at a fixed time (20 days) post infection, the tumors with higher net rates of PDGF secretion grew much more within that time, extending the tumor radius further at all densities above the baseline olig2+ glial progenitors in the brain.

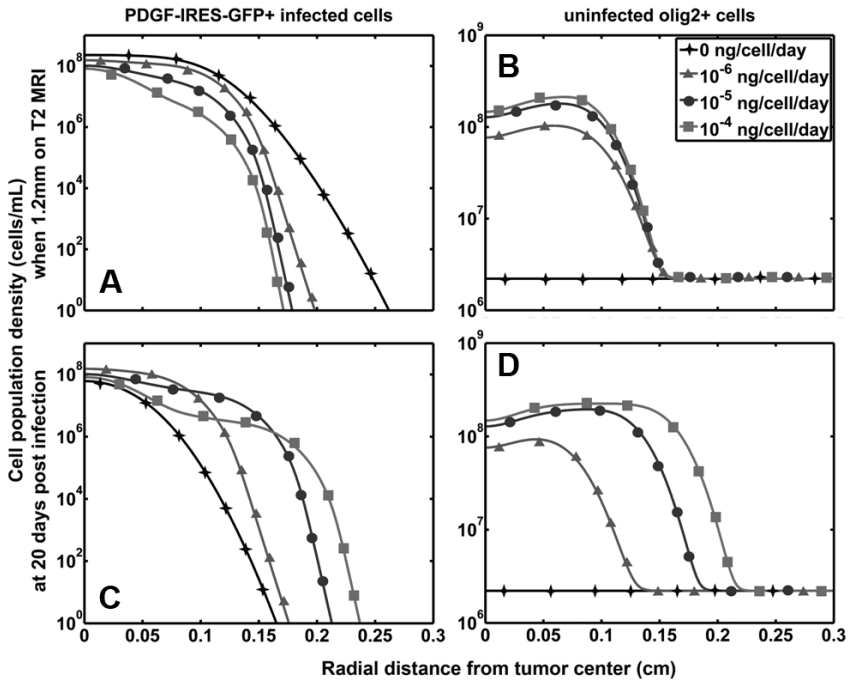

Figure 4.5: **Distributions of cell population densities vs. the radial distance from the center of the tumor at different levels of recruitment via PDGF secretion.** The first column (**A** and **C**) shows data for the PDGF-IRES-GFP+ (infected) cells and the other column (**B** and **D**) shows data for the uninfected olig2+ (recruited) cells. The top row shows the cell densities at the time at which the tumor radius is 1.2 mm on T2 MRI (fixed size on MRI), while the bottom row shows these at 20 days post infection (fixed time). The legend in (B) applies to all plots and shows the rate of PDGF secretion by the PDGF-IRESGFP+ infected cells, such that the increasing trend runs from the low value at 0 ng/cell/day to the high value, 10-4 ng/cell/day. Note that the plots for uninfected olig2+ cells (B and D) have constant population densities for the tumors with no secretion of PDGF. This is because without free PDGF available to circulate in paracrine signaling loops, no recruitment can take place, causing these recruitable cells to remain at their usual density in healthy brain matter. (See text for further details regarding these results.)

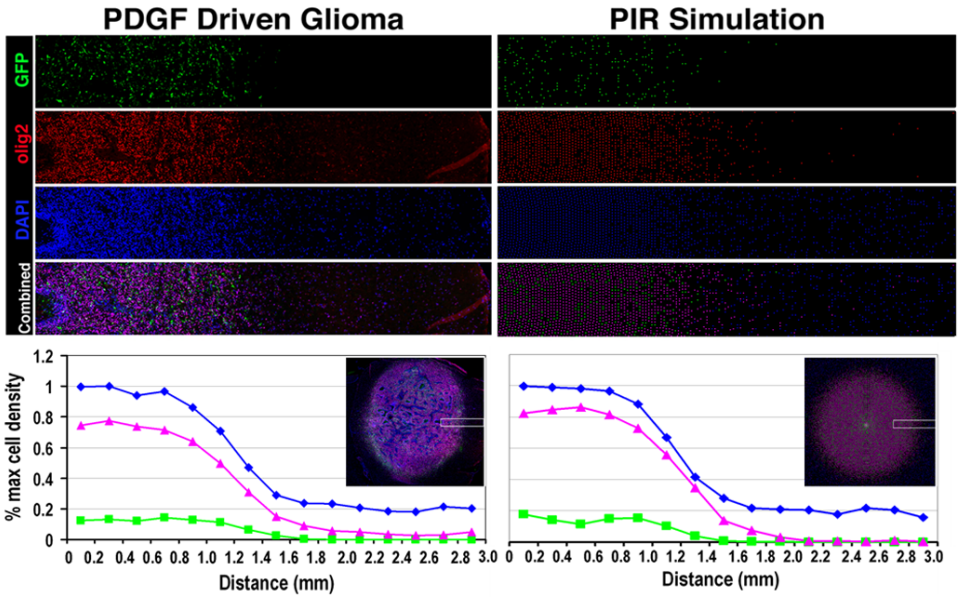

Figure 4.6: **Fluorescent micrograph compared with PIR simulation.** The color separated micrographs on the left side show the distribution and abundance of PDGF expressing cells (green), olig2+ glial progenitors (red) and the total DAPI+ nuclei (blue) within a 3 mm by 0.5 mm strip at the infiltrative edge of PDGF driven glioma. The corresponding images on the right side show the distribution and abundance of cells in a corresponding region of a simulated tumor generated by the PIR model (again, PDGF expressing cells are green, progenitors red, and all cell nuclei, blue). The graphs on the bottom show the actual (left) and simulated (right) percent measurements of each cell population within the 3 mm strip at the tumor's edge. The insets show the entire PDGF-driven tumor (left) and simulation (right) indicating the region of the tumor and simulation from which the strips were taken (white boxes).

Parameter	Definition	Value	Units
D_c	max diffusion rate of infected cells	$5.8*10^{-5}$	cm^2/day
D_r	max diffusion rate of recruited cells	$5.8*10^{-5}$	cm^2/day
D_p	diffusion rate of PDGF molecules	$5.0*10^{-4}$	cm^2/day
ρ_c	max proliferation rate of infected cells	ln(2)/(18/24)	$days^{-1}$
ρ_r	max proliferation rate of infected cells	ln(2)/(18/24)	$days^{-1}$
k	carrying capacity	$2.3*10^8$	cells/mL
λ	death rate (inverse of carrying capacity per time)	10^{-8}	mL/cell/day
η_c	gross secretion rate of PDGF by infected cells	10^{-5}	ng PDGF/cell/day
q_c	consumption of PDGF by infected cells	$10^{-5.15}$	ng PDGF/cell/day
q_r	consumption of PDGF by recruited cells	$10^{-5.15}$	ng PDGF/cell/day
$p_{autocrine}$	amount of autocrine signal	1	ng/mL
EC_{50}	half max downstream effects	$10^{1/2}$	ng/mL
k_m	half max receptor activation	30	ng/mL
χ	rate of chemotaxis of cells toward PDGF source	10^{-8}	$cm^2/day/ng$ PDGF
Initial Conditions - cell values are for the infected tissue volume within a 300 μm = 0.03 cm radius sphere			
O2a	number of glial progenitor cells	$250/((4/3)*\pi*0.03^3)$	cells/mL
n0	number of cells that are not glial progenitors	0.35*k-O2a	cells/mL
c0	number of infected glial progenitors	0.99*O2a	cells/mL
r0	number of uninfected glial progenitors remaining	O2a-c0	cells/mL
p0	amount of paracrine PDGF expressed	0	ng/mL

Figure 4.7: **Supplement Table S1. Model parameters and initial conditions.** Experimental and literature sources for $D_{c,r}$ and $\rho_{c,r}$ are described in the main text; all others are discussed in the supplemental material.

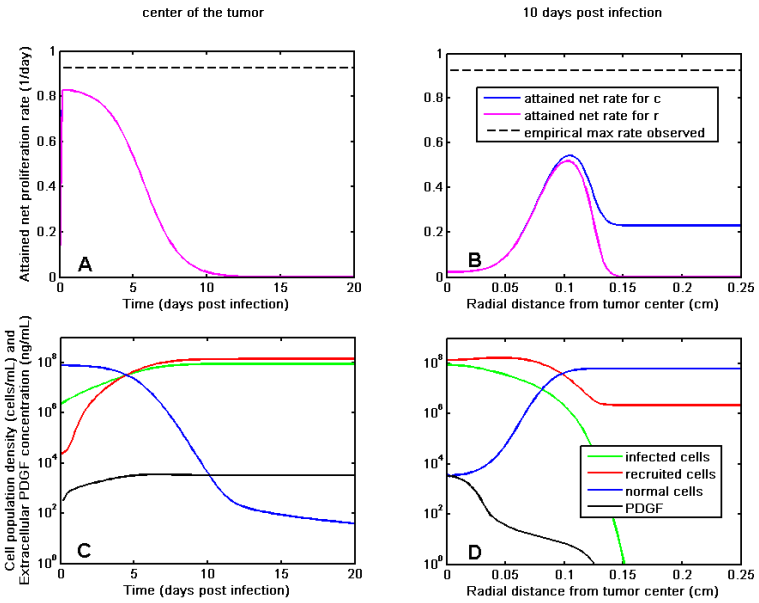

Figure 4.8: **Attained net proliferation rates due to dose response terms as compared to parameterized maximums.** Panels **A** and **B**: Attained proliferation rate vs. (**A**) days post infection at the center of the tumor, and (**B**) radial distance from tumor center at 10 days post infection. Black dashed lines represent the parameter value for the maximum possible net proliferation rate (i.e., $\rho_{c,r}$) that could occur under very high levels of PDGF stimulation. Blue and magenta curves represent the highest actual proliferation rate attained during the simulation by the infected and recruited cells, respectively. Note that in **A** the blue curve is hidden entirely by the magenta curve as they are nearly identical. Notice also in **B** that although the blue curve extends out to the full edge of the rat brain, this is not reflective of the number of infected cells there (compare with panel **D**), but rather the rate of proliferation any infected cell in that region undergoes.That is, while there are very few pioneering infected cells and no measurable PDGF molecules in the extracellular space at 0.25 cm out from the center of the tumor, any infected cell there will proliferate at the level shown, due to its own autocrine PDGF stimulation. Panels **C** and **D**: Tumor cell population densities and extracellular PDGF concentration vs. (**C**) days post infection, and (**D**) the radial distance from the center of the tumor. The green line represents the PDGF-IRES-GFP+ infected tumor cells, the red line represents recruited glial progenitor cells, the blue line represents the remaining brain cells, and the black line represents the concentration of PDGF.

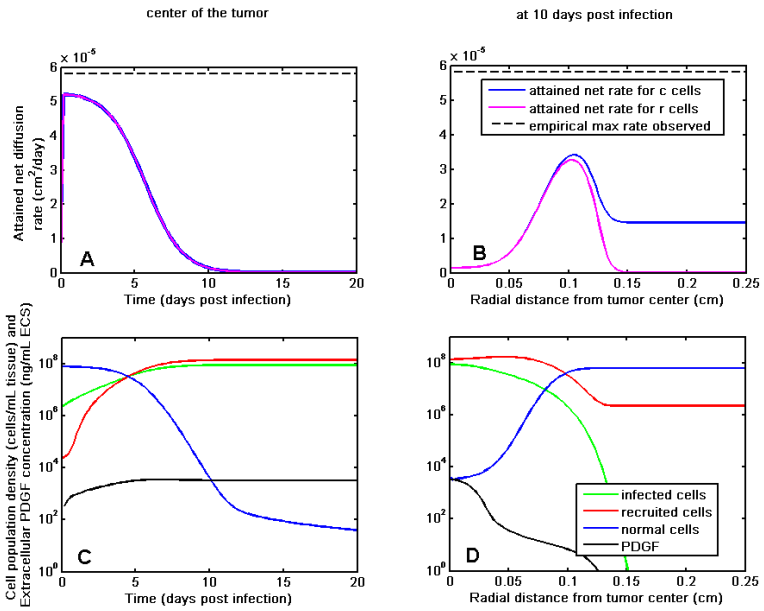

Figure 4.9: **Supplemental Figure S2. Attained net diffusion rates due to dose response terms as compared to parameterized maximum rates. A.** The attained diffusion rate vs. days post infection at the center of the tumor. The black dashed line here again represents the maximal diffusion rate that would be possible, while the blue and red curves (the latter of which is directly behind the former, due to the fact that they are nearly identical) represent the highest diffusion rates actually attained by the recruited and infected cells, respectively, at this location and these times in the simulated tumor, due to the shape of the dose response term. **B.** Attained diffusion rate vs. the radial distance from the tumors center at 10 days post infection. Here the black dashed line represents the maximum diffusion rate possible (the value of our parameters $D_{c,r}$), while the blue and magenta curves represent the highest diffusion rates that were actually reached by the recruited and infected cells, respectively, at the specified locations after the tumor has grown for 10 days in silico. **C.** Tumor cell population densities and extracellular PDGF concentration vs. days post infection. Here the green line represents the PDGF-IRES-GFP+ infected tumor cells, the red line represents recruited glial progenitor cells, the blue line represents the remaining brain cells, and the black line represents the concentration of PDGF. **D.** Tumor cell population densities and extracellular PDGF concentration vs. the radial distance from the center of the tumor. The colored lines represent the same entities as in (C).

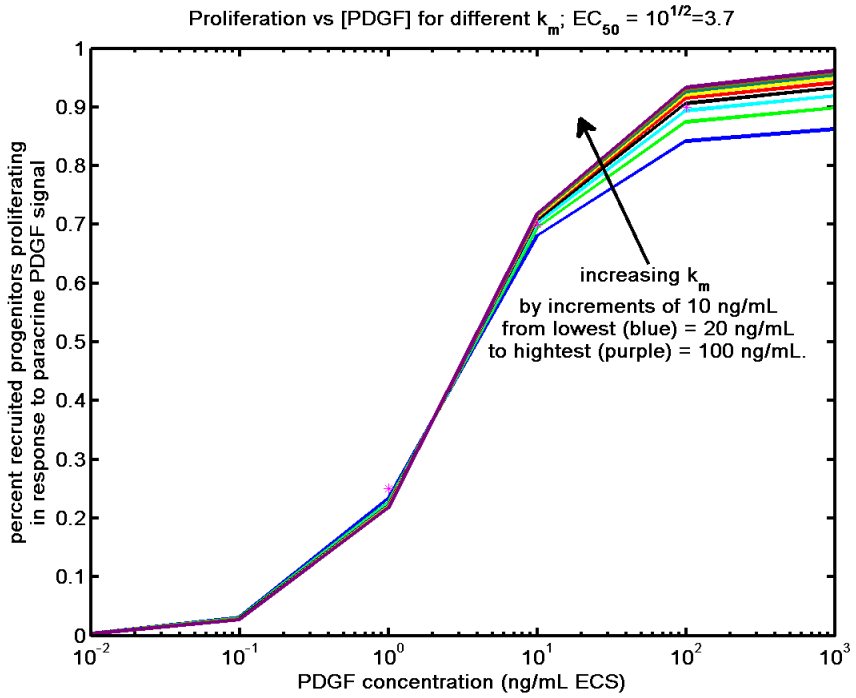

Figure 4.10: **Supplemental Figure S3. Percent progenitors proliferating in response to PDGF concentration levels for varied km values.** This image shows a simulated version of the experiment done in [81], as discussed in the supplemental text on km and EC50 parameterization. The colored curves represent dose response curves for the given EC50 at different levels of km, with blue being the lowest km, purple being the highest, and the black arrow indicating the order of increasing km. The magenta points indicate the data points on the curve in [81]. Higher km results in a steeper slope, and the variation of slope is particularly noticeable at higher PDGF concentrations. Since the data point for the lowest PDGF concentration (1 ng/mL) is closest to the low value of km and the highest data point is closest to the cyan curve (representing 40 ng/mL), we took the green curve (30 ng/mL), which passes through the mid value data point along with the cyan, as the closest approximation to the data in [81].

Chapter 5

DATA ANALYSIS AND PARAMETERIZATION OF PROLIFERATION–INVASION–RECRUITMENT MODEL

Model parameterization is often one of the most challenging components of biomathematical modeling. In our case, we were very fortunate to develop our model in close collaboration with an experimentalist. This enabled us to determine a number of parameters through direct analysis of experimental data. Here I will detail how this was done, as well as discuss parameterization for those parameters which were not amenable to experimental determination.

5.1 Derivation of parameters relating tumor expansion and overall brain.

These parameters were found through computation, based on the size and space requirements of cells in the brain. We use an average cell size of 10 μm radius, leaning towards the size of the smaller glial cells and glial progenitors. Further, we assume a spherical geometry of those cells (glial cells and progenitors), even though neurons have complicated geometry. These assumptions are made on the expectation that areas of dense tumor in our model with be comprised primarily of glial progenitors and few, if any, neurons. Thus, using the smaller cell size with a simple spherical geometry is reasonable.

5.1.1 Carrying Capacity, K.

Assuming the radius of one cell to be approximately 10 μm (which yields a cell volume of approximately $4.189 * 10^3$ μm^3), we can have at most

$$K = \frac{1 \text{ cell}}{4.189 \times 10^3 \mu\text{m}^3} \cdot \left(\frac{10^4 \mu\text{m}}{1 \text{ cm}} \right)^3 \tag{5.1}$$

$$= \frac{1 \text{ cell}}{4.189 \times 10^3 \mu\text{m}^3} \cdot \frac{10^{12} \mu\text{m}^3}{1 \text{ cm}^3} \tag{5.2}$$

$$= \frac{2.39 \times 10^8 \text{ cells}}{1 \text{ cm}^3}, \tag{5.3}$$

or in words, 2.39×10^8 cells per cubic centimeter of brain tissue. This is approximately three times the normal cellularity of the brain, which is approximately 8×10^7 cells/mL [16]. However, tumor regions are denser than normal brain [61], and normal brain areas contains neurons, which are much larger than the glia and glial progenitor cells. Thus, we expect the carrying capacity of a tumor to be higher than the normal cellularity.

Noting that 1 mL = 1 cm^3, we can write this maximum cellular density as

$$K = 2.39 \times 10^8 \text{cells/mL} \tag{5.4}$$

and take K as the carrying capacity for all cells in the tissue combined.

5.1.2 Death rate of non tumor cells, λ.

The overall death rate of the normal (nontumor) brain cells is determined by $-\lambda(c + r)$, where $c + r$ is the total tumor cell density (comprised of both transduced OPCs, c, and recruited OPCs, r). Thus, the death rate will be higher in areas of high tumor cell density, and in areas of little or no tumor, the death rate will be small or zero.

We would like for the death rate $-\lambda(c+r)$ to be near -1 when the tumor cell density is near the carrying capacity (i.e., $c + r \approx K$), so we chose λ to be the inverse of the carrying capacity in magnitude, in units of days^{-1}:

$$\lambda = 1 \times 10^{-8} \text{ days}^{-1} \tag{5.5}$$

where the units of "per day" were chosen to correspond to the time units of the model.

5.2 PDGF parameters

These parameters were among the most difficult to estimate, primarily because we are bridging the molecular scale with the cellular scale and there are limited experimental techniques

available to determine these. We begin with those that were based in literature sources, and end with those about which we mostly made educated guesses, as we will detail.

5.2.1 Michaelis-Menten parameters, k_m and EC_{50}

Parameters k_m and EC_{50} indicate the PDGF concentrations inducing half-maximal receptor activation and downstream effects, respectively. Referring to data in [81], we derived our values for the PDGF concentration at which half-maximal receptor activation occurs using the $EC_{50} = 10^{1/2}$ (reported in the dose-response curve of progenitors incorporating BrdU in [81]). We then simulated the experiment done by Pringle, et al. [81], for various values of k_m, which altered the steepness of the doseresponse curve. The simulated curve that best fit the data (by nonlinear least squares) for PDGF-BB in [81] corresponded to a k_m of 30 ng/mL. Figures of these dose response curves (both simulated and the data we compared to) can be found in chapter 2, see Figure 2.3.

5.2.2 Extracellular PDGF dispersion, D_p.

Our value for the net PDGF diffusion rate came in part from the values for diffusion of EGF and albumin in rat cortical slices, which were 0.0448 cm^2/day (converted from $5.18 * 10^{-7}$ cm^2/s, in [105] and 0.015 cm^2/day for bovine albumin [103]. This gave us an approximation for parameter D_p, around which we varied the value a few orders of magnitude above and below. Since we assume that p is consumed very quickly due to being in a region dense with cells expressing PDGFRs, we reason that net diffusion of PDGF would appear slower than it would in a tissue with fewer receptors and cells to consume the growth factor. In particular, the tumor is on a spatial scale of millimeters, with amount of to time diffuse out of the local tissue on the order of hours or days, while spacing between cells is on the scale of micrometers. Thus, we suppose that the likelihood that much PDGF would diffuse out of the bulk of the tumor rather than interacting with a receptor is low overall. Additional binding of PDGF to extracellular matrix could further decrease the apparent diffusion coefficient. At lower levels, D_p did not play a large role in determining the outcome

of our model, so we primarily focused on a value that was of reasonable magnitude and was not so low as to result in numerical instability (as was the case for values of D_p lower than $5.0 * 10^{-4}$ cm^2/day) when solving the model equations. Since this parameter does influence the dynamics of the model (see Figures 6.4 and 6.5 in the sensitivity analysis of Chapter 6), further experimental work to better determine this value could improve model accuracy.

5.2.3 PDGF signalling parameters: production rate, η_c, autocrine signal, $p_{autocrine}$, and consumption rates, q_c, q_r.

Production rate, η_c.

We obtained the net rate of PDGF accumulation into the media from experiments with confluent PDGF-IRES-GFP+ cells over 24 hours [9]. We estimated that this value of 29.2 ± 7.4 ng/mL to be approximately equivalent to a *net* secretion rate of 10^{-7} ng/cell/day, using our value for carrying capacity K. Since we do not have methods for measuring the *gross* rate of PDGF secretion—this is something that has yet to be developed experimentally—we varied the value of this parameter, η_c, over several orders of magnitude in simulations, using values that were larger than the aforementioned measured net accumulation of PDGF in confluent dishes.

Selecting one possible gross secretion rate, $\eta_c = 10^{-5}$, only the PDGF consumption rates q_c and q_r and the level of autocrine signal ($p_{autocrine}$), remained to be determined.

Consumption rates q_c, q_r, and autocrine PDGF signal level $p_{autocrine}$.

We began by making the simplifying assumption that the gross rate of PDGF consumption in paracrine loops for both infected and uninfected glial progenitors (q_c and q_r, respectively) is the same. This is reasonable given that their only difference is the production or not of the PDGF-expressing retrovirus (not a difference in expression of PDGF receptor expression), and at this time biological data does not exist to indicate that secretion of PDGF ligand by a cell affects its consumption of PDGF differently from that of a glial progenitor that does

not secrete the ligand. Thus, we denote the shared parameter value as $q_{c,r}$.

Now, we do assume that the overall behavior of transduced glial progenitor cells, c, is a bit different from that of the recruited progenitors, r, attributing this to autocrine stimulation rather than a difference in paracrine stimulation, with parameter $p_{autocrine}$ denoting the level of PDGF participating in this autocrine signalling.

Varying these two parameters, $p_{autocrine}$ and $q_{c,r}$, with all the others fixed, we compared the resulting simulation outcomes with empirical data from the experimental rat model. That is, we matched the simulated size on MRI and the radial velocity of total tumor cells (both PDGF-IRES-GFP+ and uninfected glial progenitors) determined by the model (resultant from varying these two parameters) to the spherical radius and radial velocity derived from measurements of T2 flair MRI images of one rat at days 5, 10, and 17 post infection with the retrovirus (see Figure 4.3).

This last component of parameterization is not without pitfalls. Note that only one rat had MRI imaging done in this study, and that this rats tumor grew more slowly than was observed on average. Furthermore, as a result of this parameter fitting, PDGF levels in simulations accumulate far above k_m at the densest regions of the tumor (at the center) and persist at these high levels in the center of the tumor. This is also higher than the net PDGF amount found in the experiment with confluent cells, though this is a different environment than that of a tumor. The concentration of unbound PDGF in the extracellular space of tumors or even normal brain tissue is not presently known and cannot be measured at this time with existing technology.

Since the attained *in silico* concentration of PDGF can be well-above saturating levels, much of this additional PDGF does little to increase the net diffusion and net proliferation rates displayed by the cells. That is, the tumor could persist in similar growth patterns at PDGF amounts well-below these high levels. Because we relied on the limited MRI data to help parameterize the model, additional MRI data from more animals is indicated in future experimentation to facilitate a more robust estimation of these parameters. Additionally, more knowledge about possible PDGF receptor upregulation and PDGF degradation in brain

tissues, as well as techniques to evaluate the actual concentration of PDGF in extracellular space, would aid in the verification or improvement of these model parameters, ensuring that the source and sink of PDGF into and out of the extracellular space is properly accounted for in the model.

5.3 Cell Tracking to Determine Proliferation and Diffusion Rates

Parameterization of motility and prolieferation rates of cells differs greatly from that of the other parameters described heretofore. Unlike those, these parameter values are grounded in ample data obtained from the tracking of individual cells in acute brain slices from experimental tumors. The technique used for obtaining these parameters was described briefly in [67], which is reprinted in Chapter 4. Here we expand on the details of this data analysis.

5.3.1 Quantification of Diffusion Rate

The most extensive data available to us was of cellular motility, in the form of fluorescence microscopy cell tracking. Briefly, this procedure entailed obtaining acute brain slices from anaesthetized rats with PDGF-driven experimental tumors, which were maintained in serum-free medium during imaging in a stage-mounted incubator. These slices were 300 μm thick and taken in the coronal plane intersecting the injection point. Furthermore, the transduced and recruited cells in the tumors were labeled to express two distinct fluorophores: green fluorescent protein (GFP) and a red fluorescent protein (m-Cherry), respectively. This enabled us to observe both populations simultaneously.

Images were taken with a digital camera mounted to the microscope every 3 minutes, for seven hours or longer. Following image acquisition, the migratory paths of the fluorescently labeled cells were tracked using the Metamorph image analysis system (see [10,12] for further detail). Note that the analysis of cellular migration was limited to cells at the infiltrative margins of the tumor, where the density of retrovirus-labeled cells was low enough to allow for clear visualization of individual cells using this technique.

Once the migration paths were tracked, the x– and y–coordinates of each tracked cell, at

each of the time points, was imported into MATLAB so that we could determine the mean squared displacement (MSD) traveled versus time for each cell. In determining the MSD, we compute the distance travelled from the cells starting position (the origin). One way to visualize this is to place the cell tracks on a coordinate plane, with all tracks sharing a common origin, in a *wind rose* plot (see Figure 4.2D in Chapter 4). In a wind rose plot, we see the cells move outward from this common origin as we look at later time points.

The squared displacement between each cells position at timepoints $t > 0$ and their starting position at time $t = 0$, the common origin, is computed and averaged to obtain the MSD. Putting it more mathematically, we have (x, y) coordinates at each time point for each tracked cell. The squared displacement for a given cell track at arbitrary time t is

$$SD_t = (x_t - x_0)^2 + (y_t - y_0)^2. \tag{5.6}$$

If we have already adjusted the data to give the tracks a common origin at $(0, 0)$, then this simplifies to

$$SD_t = (x_t - 0)^2 + (y_t - 0)^2 \tag{5.7}$$

$$SD_t = (x_t)^2 + (y_t)^2 \tag{5.8}$$

which conveniently allows us to work with the vectors of data for each cell track. That is, for each cell track, we can get a vector of squared displacement, $SD = [SD_1, SD_2, ..., SD_t, ..]$, at each time point after $t = 0$ by squaring each element of $\vec{x}$ and $\vec{y}$, then adding them element-wise.

Then, to get the *mean* squared displacement, we average the SD vectors across all cells at each timepoint:

$$MSD_t = \frac{SD_t^{Track1} + SD_t^{Track2} + \cdot + SD_t^{TrackN}}{N} \tag{5.9}$$

or we can do this for all timepoints at once:

$$MSD = \frac{SD_{Track1} + SD_{Track2} + \cdot + SD_{TrackN}}{N} \tag{5.10}$$

This was done for both the red cell population (recruited) and the green cell population (transduced) to obtain their MSD versus time curves, as shown in Chapter 4 in Figure 4.2C.

Note that MSD versus time curves for random walks and biased random walks are non-linear at early time points. This is because any travel between 2 points looks like a straight line, and the square of this linear displacement is a parabolic curve. For our data, since we are looking mostly in a white matter region, where there is known to be more directionality to the movement of cells [24], the cells have a tendency to move in straighter paths. Thus, it is unsurprising to see some nonlinearity in our MSD curves for the first few time points (see Figure 4.2C). At later time points, however, the MSD curves are linear, the slopes of which provide estimates for the diffusion rates of the two cell populations.

Thus, we fit a line to the linear portion of each curve, and take the slopes of the linear fits as the diffusion rates for each cell population. This gave 920 μm^2 as the diffusion rate for the transduced population, and 660 μm^2 for the recruited population. Because we do not have any evidence to suggest that there is any difference between the two cells other than the ability of transduced cells to produce PDGF, we attribute the increased diffusion rate of the transduced cells to an autocrine PDGF signal. In our model, the diffusion rate is allowed to vary, depending on the level of local PDGF signal and on the local cell density. Based on these observed differences in rate, we added a parameter representing the additional autocrine stimulation that transduced cells experience, $p_{autocrine}$, and determined that the maximum possible rate (the parameter used) was likely the same if they were under the same levels of PDGF stimulation. Figure 4.9B shows how the diffusion rates differ at the leading edge of the tumor (corresponding with where the data was collected) at 10 days of simulated tumor growth.

5.3.2 Quantification of Proliferation Rate

Time-lapse microscopy was also effective for obtaining the proliferation rate parameter, allowing direct monitoring of the mitotic activity of RED and GREEN labeled cells in the acute slices of the PDGF-driven brain tumors. Proliferation rates were determined by counting the

number of tracked cells that underwent mitosis during the course of the time-lapse experiment. As is the case with the analysis of cell migration, the analysis of cell proliferation was limited to cells at the infiltrative margins of the tumor, where the density of retrovirus-labeled cells was low enough to allow for clear visualization of individual dividing cells.

This analysis showed that approximately 2% of progenitors at the infiltrative margins of the tumor underwent mitosis every hour (giving a cell cycle time of approximately 50 hours). *In vitro* studies have shown that PDGF stimulated glial progenitors can proliferate with cell cycle times as fast as 10-20 hours [114]. Since our observations were made at the invading edge of the tumor for clearer visualization of individual cells and cellular proliferation rate is dose-responsive to local PDGF levels [81, 110], we have assumed that the longer cycle time is likely due to the decreased PDGF level in this region. The overall result of having such a dose-response relationship is that we have effective proliferation rates that are slower at lower PDGF concentrations and reach maximal proliferation rates only at saturating levels of PDGF, provided there is sufficient space.

5.4 Extending Cell Tracking Analysis to Compare Anti-Invasive Therapies

In addition to parameterizing the Proliferation–Invasion–Recruitment (PIR) model of Chapter 4, the cell tracking technique described in Section 5.3.1 was also to look at the effect of different anti-invasive agents on the migration of cells in collaboration with researchers at Columbia University.

5.4.1 Experimental Data

The experimentalists looked at several different tumor types, all caused by transduction of glial progenitor cells with retroviruses causing expression of either epidermal growth factor receptor (EGFR) or platelet-derived growth factor (PDGF). Animals who received the EGFR-expressing virus developed tumors that resemble human gliomas; those who received a co-injection of both viruses developed tumors that resemble gliomatosis cerebri—an extremely invasive brain tumor that is not amenable to surgical resection. Removing brain

tissue from the animals, they then applied various potential therapeutics to assess their efficacy in reducing the invasion of tumor cells, tracking fluorescently labeled cells as described above in Section 5.3.1.

Looking at thirteen conditions spread across the two experimental tumor types, in which most had > 100 individual cells that were tracked every 15 minutes for 18 hours, resulted in an abundance of cell position time series data. Analyzing this data was key to quantifying the effect of each of the agents, helping to assess which might be most promising in reducing the invasiveness of tumors. (For more details about the agents tested and the biology of tumor cell invasion, please see [49].)

5.4.2 Population Level Analysis

Initially following the procedure we used for the PIR model data in Section 5.3.1, individual cell tracks from time-lapse microscopy were plotted to a common origin to generate wind rose plots for spatial comparison of the effective spread of the cells across experimental conditions. We then computed the mean squared displacement (MSD) for the tracked cells within each experimental condition, as shown in Figures 5.1 and 5.2. The wind roses show the overall spread of the cells and give a qualitative sense of how the cells were affected by the various agents, while the MSD vs time curves and their associated esimated diffusion rates give a more quantitative picture of the effect.

However, there are outliers that are clearly visible in the wind roses, which show greater persistence in their movement. The technique used above does not adequately consider those, which may be important in understanding how to best stop tumor cell invasion. To really determine whether an agent was effective, we needed more than an overall population diffusion coefficient—we needed to characterize the movement of individual cells, thereby allowing us to see the full spectrum of responses within each condition.

5.4.3 Individual Cell Analysis

To fit individual cells, we first found the squared diplacements, SD, between all time points. That is, for the displacement at a time interval of length T, we combined data from all time points t_a, t_b, with $t_b > t_a$, such that $t_b - t_a = T$. We then averaged the squared diplacements corresponding with each unique T, giving us a mean squared displacement, MSD and as-

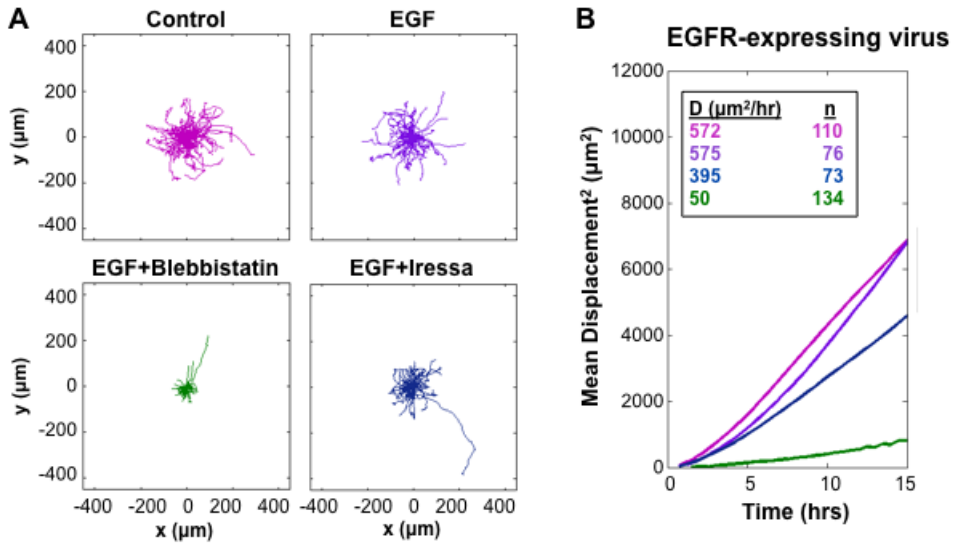

Figure 5.1: **Cells Tracked in EGFR–driven Experimental Tumors. A.** Wind rose plots of cell tracks from experimental tumors treated with indicated agents or from the control condition. These show qualitatively that blebbistatin results in the greatest descrease of movement overall. **B.** Mean squared displacement versus time and resulting diffusion coeffcients for the four groups indicated in (A). The legend shows the diffusion coefficients for each treatment, D, as well as the number of cells tracked in that treatment, n. The colors of the lines and the D, n values match the colors of cell tracks in the windroses, with pink, purple, blue, and green indicating Control, EGF, EGF+Iressa and EGF+Blebbistatin, respectively. The D values provide quantitative measures of cellular movement within the treatment groups.

signed weights to these. The weights simply indicate the number of combinations of t_a and t_b differences that resulted in a particular T and thus the number of SD values that were averaged to obtain the MSD, that corresponds with that given T. Generally, values at shorter time intervals were more heavily weighted than those at longer time intervals, since more combinations of data points were possible to get the same short interval length. However, this was not the case for cells whose x,y–positions were noted at inexact time intervals.

Following the approach in [92], we applied a weighted nonlinear regression (using the weights just described) to fit this data to a model relating cell speed and persistence time, s and P, respectively, with the mean squared displacement, MSD:

$$MSD = s^2 P^2 \left(\frac{T}{P} - 1 + e^{\frac{T}{P}} \right), \tag{5.11}$$

where T indicates the time interval corresponding to the squared displacement. This was done for each individual tracked cell. Examples are shown in Figure 5.3.

Having the speed and persistence times, we can then compute the diffusion coefficient for an individual cell using the following relation:

$$D = \frac{s^2 P}{n}, \tag{5.12}$$

where n is the dimension of the space in which the cells were followed. In our case, we use $n = 2$, since cells were followed in a slice of tissue. There is some thickness to the slice, but movement in that plane is neglible, being on the order of several cell widths. Table 5.1 summarizes the individual cell tracking data, where we report the averages of the individual cell speeds, persistence times, and individually computed diffusion rates (using (5.12)) within each condition. We also give the spread of the data in the form of the median absolute deviation (MAD), which is defined as

$$MAD = \text{median}(\text{abs}(X_i - \text{median}(X))) \tag{5.13}$$

where X is a set of data, and X_i is an individual datum of that set. We chose this statistic because it is robust, not relying on the data conforming to any particular distribution, and can handle any extreme outliers without excessively skewing the deviation.

5.4.4 Conclusion.

Our analysis quantified the effects of various anti-invasive agents on these experimental tumors, and showed that those acting on myosin-II, which acts upstream of the EGFR and PDGF pathways, were most effective at reducing the diffusion of cells. Drugs that directly inhibited these pathways were less effective or could be overcome, likely due to redundancies in these growth factor pathways. We also note that in reality, we have a biased random walk due to anisotropic diffusion along white matter tracts in the brain. This leads to both increased persistence times, and can appear as more nonlinearity in MSD versus time curves. Since some MSD curves were more nonlinear, this provided a way of estimating D that does not rely on identifying a linear portion of the MSD curve, making it more useful overall. Being able to characterize and determine the statistical significance of the changes on cellular diffusion in each condition enabled us and our collaborators to arrive at this conclusion.

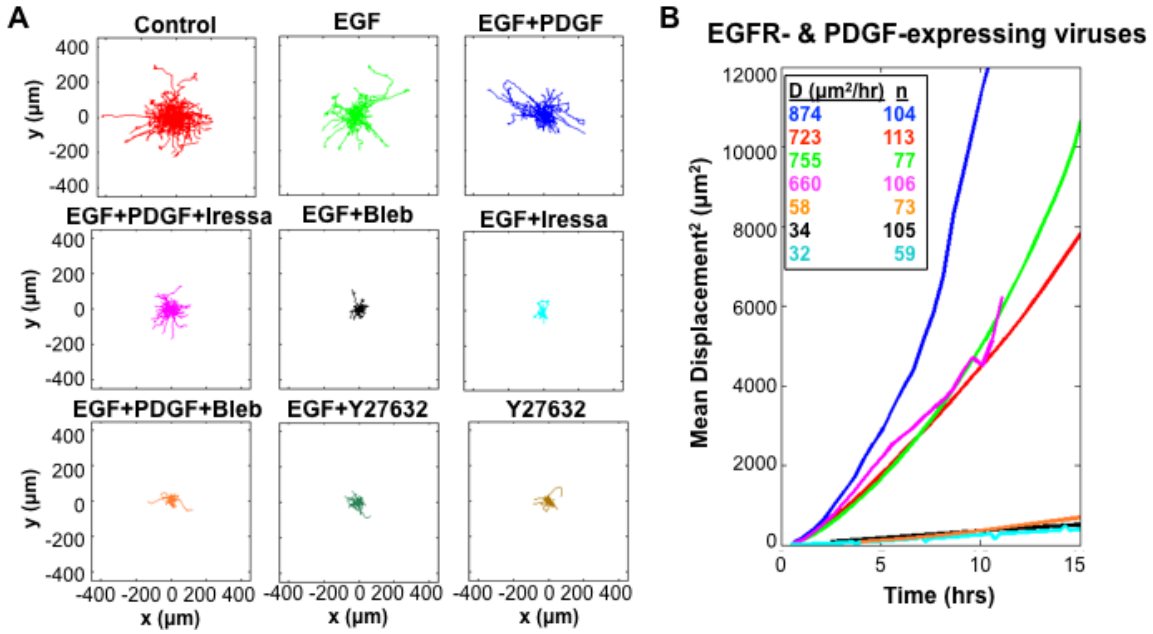

Figure 5.2: **Cells Tracked in PDGF– and EGFR–driven Experimental Gliomatosis Cerebri. A.** Wind rose plots of cell tracks from experimental gliomatosis in the indicated treatment groups. These show that a number of treatment groups resulted in reduced overall cellular movement. **B.** Mean squared displacement versus time and resulting diffusion coefficients for the treatment groups indicated in (A). The legend shows the diffusion coefficients for each treatment, D, as well as the number of cells tracked in that treatment, n. The colors of the lines and the D, n values match the colors of cell tracks in the windroses, with red, green, blue, pink, black, cyan, and orange corresponding to Control, EGF, EGF+PDGF, EGF+PDGF+Iressa, EGF+Blebbistatin, EGF+Iressa, and EGF+PDGF+Blebbistatin, respectively. The conditions Y27632 and EGF+Y27632 have MSD curves that are hidden by the other curves at the bottom of the plot, and for other reasons our collaborators chose to exclude these from further analysis. The D values show quantitatively the degree to which agents have reduced the movement of the cells as compared to the cells of the other treatment groups.

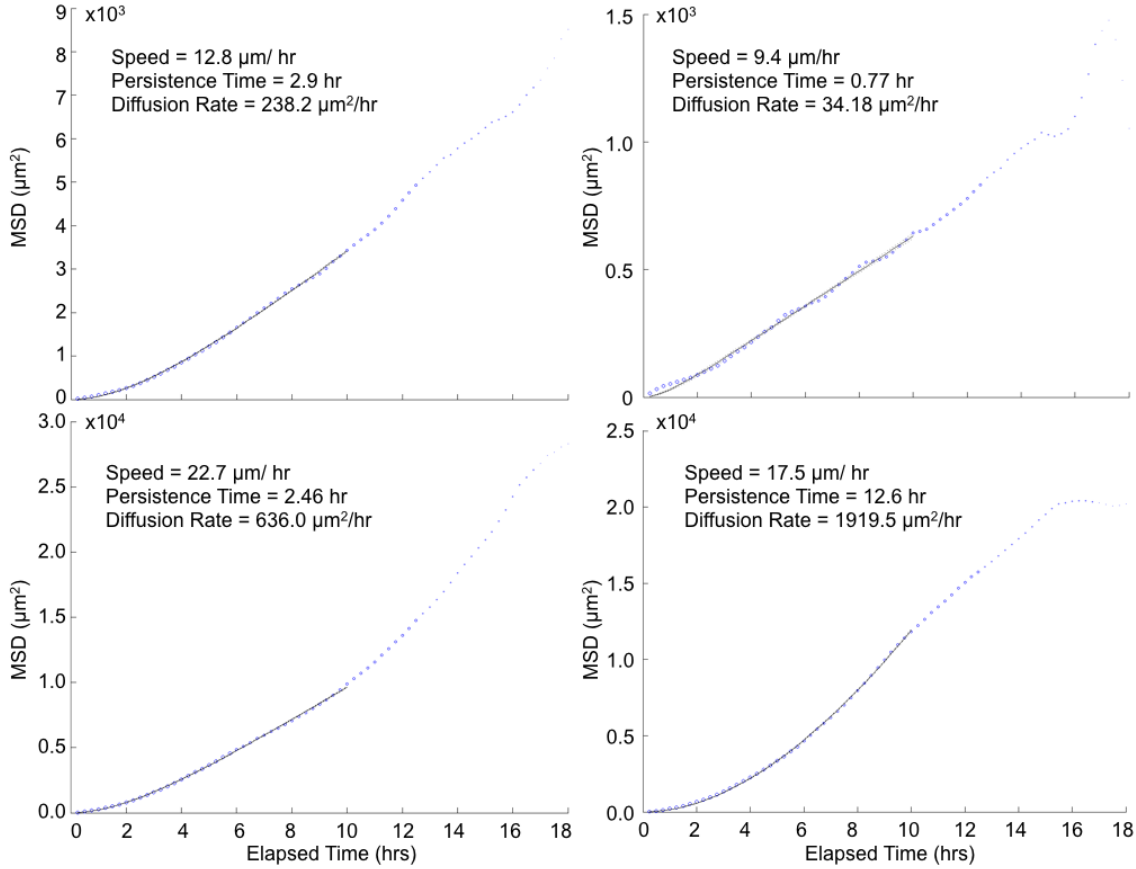

Figure 5.3: **Characterization of Individual Cell Movement.** These four plots show MSD versus time interval lengths for four individual cells. The blue circles are actual data, with larger circles indicating greater weights. The black line is the fit from the weighted nonlinear regression, which corresponds with the individual speed and persistence measures. These two parameters were then used to obtain the cell–specific diffusion rate. Note that all four cells are from the control EGFR–driven tumors; these examples were selected to help show the range of movement patterns exhibited by individual cells within a single condition.

Table 5.1: **Summary of Individual Cell Fit Parameters.** Estimates of individual cell speeds and persistence times, as well as the individually computed diffusion rates (using equation (5.12)) are averaged within each condition, as given. To show the variation within each condition, we also report the median average deviation (MAD), calculated using equation (5.13).

Condition	N	Speed (μm/hr) Mean±MAD	Persistence (hr) Mean±MAD	Diffusion (μm^2/hr) Mean±MAD
GLIOMATOSIS				
Control	50	27.04 ± 8.75	5.04 ± 1.79	469.7 ± 176.9
EGF	33	22.90 ± 7.17	4.02 ± 1.48	476.1 ± 196.3
EGF+PDGF	24	15.83 ± 4.41	5.35 ± 1.27	409.4 ± 135.3
EGF+PDGF+Iressa	35	18.80 ± 8.22	5.36 ± 2.10	314.1 ± 117.4
EGF+PDGF+Blebbistatin	36	5.79 ± 2.45	3.45 ± 2.00	27.46 ± 11.42
EGF+Blebbistatin	41	6.07 ± 1.94	6.73 ± 1.62	41.71 ± 11.30
EGF+Iressa	24	3.18 ± 1.20	12.98 ± 2.00	48.43 ± 8.94
EGF+Y27632	41	5.61 ± 1.87	9.49 ± 2.05	96.46 ± 21.90
Y27632	53	4.98 ± 1.21	7.59 ± 2.21	61.53 ± 4.98
TUMOR				
Control	61	27.90 ± 6.96	66.25 ± 1.36	999.0 ± 209.1
EGF	46	11.71 ± 4.29	17.27 ± 3.65	1024.3 ± 160.2
EGF+Iressa	42	12.50 ± 4.10	52.72 ± 1.94	458.0 ± 144.6
EGF+Blebbistatin	87	3.52 ± 1.22	15.87 ± 6.21	83.16 ± 21.21
EGF+Y27632	23	11.61 ± 4.10	3.65 ± 1.39	196.1 ± 58.19
rac	125	6.36 ± 2.47	5.45 ± 1.40	60.59 ± 23.08
ml7	103	7.48 ± 2.44	30.09 ± 1.54	331.5 ± 18.82
arp	32	21.03 ± 8.38	15.83 ± 1.08	2596.9 ± 195.8

Chapter 6

SENSITIVITY ANALYSIS OF PROLIFERATION–INVASION–RECRUITMENT MODEL

6.1 Introduction

We have shown how we developed the proliferation–invasion–recruitment (PIR) model in chapter 4. We've also discussed how we parameterized the model (where possible) with experimental data in chapter 5, and examined the linear stability of the model in chapter A. Now, let's turn to analyzing the sensitivity of the model to changes in our parameters.

As we developed the model, we tried to minimize the number of biologically undetermined parameters in our equations, and then applied sensitivity analysis to determine which parameters' uncertainty most affected the variance of solutions.

There are various methods to examine the uncertainty and sensitivity of models to parameters. The variance-based or sampling methods include a spectrum between one-at-a-time methods, where the full range of possible values of one parameter are examined (while all other parameters are all held fixed), to full factorial sampling, where every possible pairing of parameter values is used in simulations. The draw backs of these are clear: one-at-time and local methods do not look at the full input space and cannot examine interactions between inputs, yet the other extreme is computationally taxing and inefficient, with N samples per parameter and M parameters requiring N^M simulation runs. Other methods include regression analysis, which may be appropriate for linear model response, and emulators, which use machine learning to model the model, producing a so-called "metamodel."

We opted to use a sampling method, but for our model, neither the simple one-at-a-time approach nor the full factorial approach were appropriate. We have nonlinearity in our model, making parameter interactions important to include in our analysis, and we have many uncertain parameters that can we wanted to vary across magnitudes, necessitating many samples. The method that best suited our needs is the Latin hypercube sampling (LHS) method, a kind of Monte Carlo method, the output of which we analyze with the use of Partial Rank Correlation Coefficients. This approach allows us to account for parameter interactions and sample the full parameter space, while only necessitating N simulation runs.

6.2 Latin Hypercube Sampling and Partial Rank Correlation Coefficients Method

Latin hypercube sampling was first developed and published by McKay, Conover, and Beckman in 1979 [69]. Originally it was used in analyzing risk assessment models. Another group compared several methods of sensitivity analysis, including LHS paired with regression analysis, and found it to perform best [47].

The method has since been applied to other types of models. Models that are amenable to the LHS method share these characteristics: (1) many uncertain parameters, (2) outcome variables are nonlinear functions of the parameters, (3) the full range of each parameter needs to be looked at, and (4) the models are computationally taxing.

We conducted our sensitivity analysis using LHS in combination with partial rank correlation coefficients (PRCC). This approach is detailed by Blower and Dowlatabadi in [17], where it is applied to a disease transmission model.

Using a combination of Latin hypercube sampling of the parameter space and Monte Carlo

simulations, we generate an array of outcome variable solutions. Then, computing the partial rank correlation coefficients, we determined which parameters most affected the solutions. Each of these steps, including generating the plots, was done via code I wrote in MATLAB.

6.2.1 Latin hypercube sampling technique for sampling parameter space to run Monte Carlo simulations

Step 1: Parameter sampling.

Say we want to sample each of our M parameters N times (note that N should be relatively large for best results, especially if simulations are not too expensive—we often choose $N = 200$). First, we need to define each parameter's range of possible values as a probablity distribution (uniform, triangular, normal, etc.). For most of our parameters, we decided that the triangular probability distribution was most appropriate for describing our parameters ranges of possible values. This is because we could determine a maximum and a minumum, and had some sense of a most likely value, but had no other information about the shape of the distribution. A uniform distribution makes sense if we have no sense of a most likely value for that parameter. Other distributions might be better choices if we have more data about the parameters' possible values. As an example, the diffusion coefficient from cell tracking data is best approximated by a triangular distribution (see Figure 6.2).

Then, following the LHS methodology in [17], I divided each parameter's distribution into N intervals of equal area (see Figure 6.1 for an approximation). This is to ensure that we will draw more samples near the most likely value, and fewer samples near the extreme high and low values.

Next, for a given parameter's distribution, within each of the N intervals, I drew a uniform random sample and stored that value in one of the M columns in an $M \times N$ matrix, until the N samples of the given parameter fill that column.

$$\begin{bmatrix} \eta_c(1) & \rho_c(1) & \cdots & D_r(1) \\ \eta_c(2) & \rho_c(2) & \cdots & D_r(2) \\ \vdots & \vdots & \ddots & \vdots \\ \eta_c(N-1) & \rho_c(N-1) & \cdots & D_r(N-1) \\ \eta_c(N) & \rho_c(N) & \cdots & D_r(N) \end{bmatrix} \tag{6.1}$$

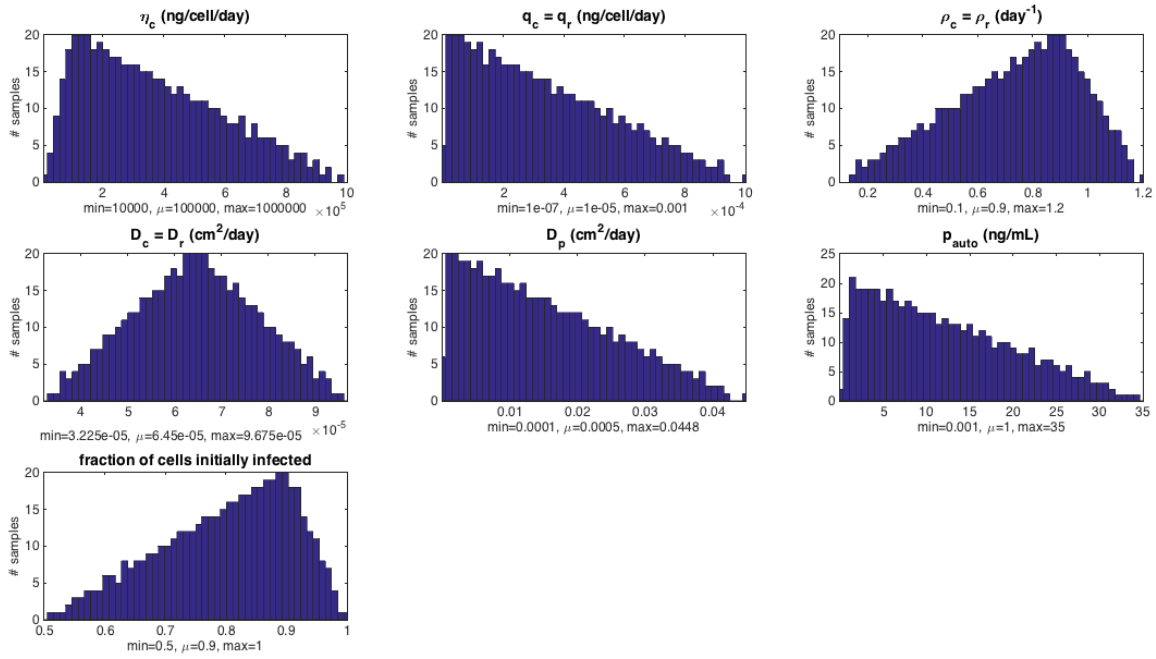

Figure 6.1: **Histograms of Parameter Sample Values.** In this example, 500 samples were drawn for each parameter. The shape of each histogram shows approximately what the probability distribution of the parameter's possible values looks like. Note that the bins of the histogram are of equal width, not equal area, so these *do not* show the intervals of equal area that we use for drawing samples. However, the histograms do show the occurence of more samples being drawn near the most likely value, since the intervals of equal area in that region would have smaller width.

Note that it is this sampling which gives us the "Latin" hypercube—because we are sampling from N distinct intervals, we have sampling without replacement. The M parameters give us an M–dimensional hypercube. The ordinal numbers essentially indicate the coordinates of the sample in this M–dimensional parameter space. In the example above, the first row of the matrix, indicates that we are drawing a sample from the first interval along the η_c axis, the first interval along the ρ_c axis, etc. Since the columns are all ordered similarly, this is a sample choice along the diagonal of our hypercube.

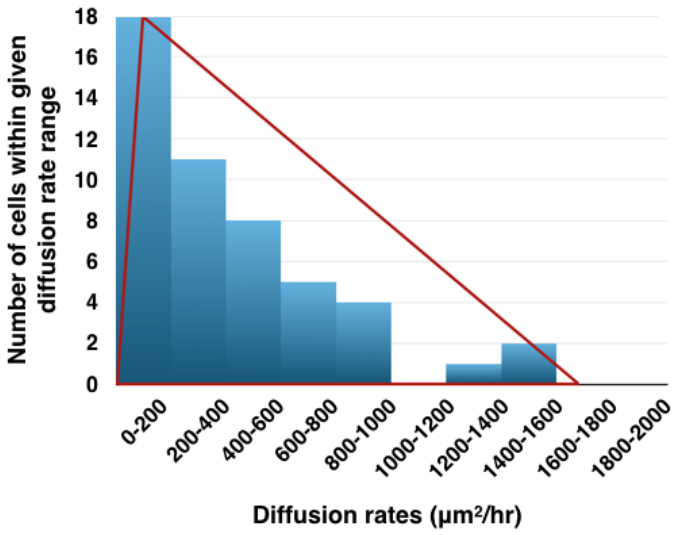

Figure 6.2: **Diffusion rate data approximated by a triangular distribution.** This distribution of diffusion rates from individually tracked cells (see Chapter 5, section 5.4.3; these are the cells of the gliomatosis control condition) data represents the many possible values can arise from cellular migration, which appears to be fairly well approximated by a triangular distribution. The peak of the triangle corresponds to the diffusion rate shared by the most cells, while the right corner corresponds with values shared by only one or two cells.

Step 2: Randomly pair samples.

After this was completed for each parameter, I permuted the values in each column of the $M \times N$ matrix of stored parameter values so that, as the matrix is read across the row, the pairing of the parameter values is random.

$$\begin{bmatrix} \eta_c(5) & \rho_c(31) & \cdots & D_r(9) \\ \eta_c(17) & \rho_c(1) & \cdots & D_r(2) \\ \vdots & \vdots & \ddots & \vdots \\ \eta_c(11) & \rho_c(3) & \cdots & D_r(N) \\ \eta_c(2) & \rho_c(28) & \cdots & D_r(4) \end{bmatrix} \tag{6.2}$$

This makes the samples more interesting, such that we do not have the smallest parameter values and largest parameter values all paired together. However, it does not alter the "Latinness" of our samples. Since the samples of each parameter (each dimension of our hypercube) are drawn without replacement, the Latin feature cannot be altered by this permutation.

Step 3: Solve model with each parameter set.

Next, we solve the model N times, using a different row of specified parameter values each time. The system of PDEs was solved numerically, as detailed in chapter 4.

Once the equations had been solved for each of the N parameter sets, I calculated the ratio of recruited progenitors to total tumor cells, $r/(c+r)$, at the center of the tumor ($x = 0$) at each time step. This was the model output we were most interested in fitting to the data with our parameterization. We can visualize the range of model outputs with an error bar plot of all the possible resulting ratios at each time point (Figure 6.3).

6.2.2 Partial Rank Correlation Coefficients for analyzing LHS results

The remaining steps allow us to compute the Partial Rank Correlation Coefficients (PRCCs) and their significance in order to compare model output with input. This allows us to see

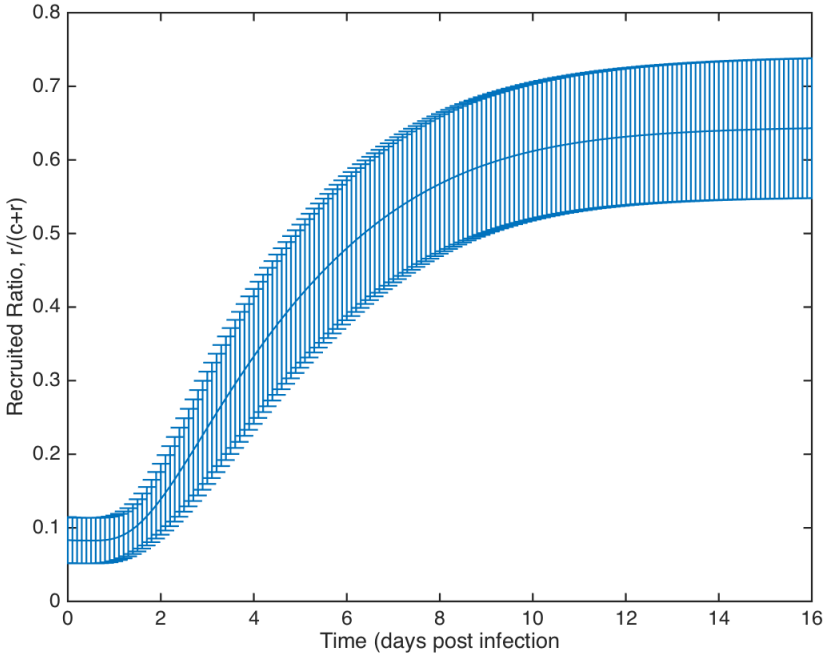

Figure 6.3: **Possible ratios of recruited to total tumor cells vs. time with specified parameter distributions.** LHS simulation results were used to calculate ratios of recruited, r, to total tumor cells, $c + r$ for each simulation over time. Looking at each time point, we calculated the mean and standard deviation. Plotting these against time, we see the spread of model outcome ratios generated by the Latin hypercube parameter samples.

which parameters are most strongly correlated with the output.

Step 4: Add output of interest to matrix of parameter samples

We then added the column of N outputs, as discussed above, to the the matrix of parameter values, such that the row of parameter values corresponds to the given output.

$$\begin{bmatrix} \eta_c(5) & \rho_c(31) & \cdots & D_r(9) \\ \eta_c(17) & \rho_c(1) & \cdots & D_r(2) \\ \vdots & \vdots & \ddots & \vdots \\ \eta_c(11) & \rho_c(3) & \cdots & D_r(N) \\ \eta_c(2) & \rho_c(28) & \cdots & D_r(4) \end{bmatrix} + \begin{bmatrix} Ratio(1) \\ Ratio(2) \\ \vdots \\ Ratio(N-1) \\ Ratio(N) \end{bmatrix} \tag{6.3}$$

$$= \begin{bmatrix} \eta_c(5) & \rho_c(31) & \cdots & D_r(9) & Ratio(1) \\ \eta_c(17) & \rho_c(1) & \cdots & D_r(2) & Ratio(2) \\ \vdots & \vdots & \ddots & \vdots & \vdots \\ \eta_c(11) & \rho_c(3) & \cdots & D_r(N) & Ratio(N-1) \\ \eta_c(2) & \rho_c(28) & \cdots & D_r(4) & Ratio(N) \end{bmatrix} \tag{6.4}$$

Step 5: Rank the input parameter and output variable values.

Next, we define a matrix R that contains the ranks of each of the input parameters and output. To do this, we sort the parameter values in each column to find each value's rank within the column. The smallest value of a given parameter is assigned value 1 and the largest is assigned value N. We then place the ordinal rank of a given parameter or output value at the same column and row location in R as that parameter or output value itself in the matrix in Step 4. Thus, R looks something like this:

$$R = \begin{bmatrix} 5 & 31 & \cdots & 9 & 10 \\ 17 & 1 & \cdots & 2 & N \\ \vdots & \vdots & \ddots & \vdots & \vdots \\ 11 & 3 & \cdots & N & 1 \\ 2 & 28 & \cdots & 4 & N-1 \end{bmatrix} \tag{6.5}$$

Step 6: Compute Pearson correlation coefficients.

Next, we use these ranks to compute the sample Pearson correlation coefficients. Letting $r_{n,m}$ denote the value in column m (of 1 to $M+1$ possible columns) and row n (of 1 to N possible rows), and $\mu = \frac{N+1}{2}$, the average rank value, we compute:

$$c_{i,j} = \frac{\sum_{n=1}^{N} (r_{n,i} - \mu)(r_{n,j})}{\sqrt{\sum_{n=1}^{N} (r_{n,i} - \mu)^2 \sum_{k=1}^{N} (r_{k,j} - \mu)^2}}, \quad i,j = 1,2,...M,M+1, \tag{6.6}$$

where the $c_{i,j}$ are values in the $M+1 \times M+1$ symmetric matrix C of correlation coefficients. Note that this can be easily done in MATLAB using the function `corrcoef.m`.

Step 7: Invert.

Now, let B be the inverse of matrix C. That is, let

$$B = [b_{i,j}] = C^{-1} \tag{6.7}$$

Step 8: Compute the partial rank correlation coefficients.

The partial rank correlation coefficient (PRCC) [51] between the ith input parameter and yth output is defined as

$$\phi_{i,y} = \frac{-b_{i,M+y}}{\sqrt{b_{i,i} b_{M+y,M+y}}}. \tag{6.8}$$

In our case, we are looking at only one output, the ratio of recruited glial progenitor cells to total tumor cells (recruited and transduced progenitors), so we have

$$\phi_{i} = \frac{-b_{i,M+1}}{\sqrt{b_{i,i} b_{M+1,M+1}}}. \tag{6.9}$$

Thus, these ϕ_i's or PRCCs form a vector of length M.

The values of these PRCCs are such that $-1 \leq \phi_i \leq 1$, and generally, the closer ϕ_i is to 1 or -1, the more significant the ith input parameter's influence on the specified outcome. The parameters corresponding to values that are closer to ± 1 are those that we most want to be careful about parameterizing. However, we can be more precise about the significance of these parameters on the outcome, as we explore in the next step.

Step 9: Determine significance with Student's T.

To determine significance of the PRCC value $\phi_{i,y}$, we compute the t-test statistic

$$t_{i,y} = \phi_{i,y}\sqrt{\frac{N-2}{1-\phi_{i,y}}}, \tag{6.10}$$

where t has a distribution that approximates that of a Student's T with $N-2$ degrees of freedom.

Since we have only one output of interest, with associated PRCCs ϕ_i, in our case we have

$$t_i = \phi_i\sqrt{\frac{N-2}{1-\phi_i}}. \tag{6.11}$$

The significance of the value of each t_i can be determined using a standard t-table. For example, if we drew $N = 100$ samples, then we have $N - 2 = 98$ degrees of freedom. Using this, we can look at the corresponding row in a t-table to find the smallest corresponding α-value for the t_i for a two-tailed test. The confidence in our result is $1 - \alpha$. Then, calculate the p-value. If the p-value is less than α, then we reject the null hypothesis and claim that that t_i significantly affects the outcome.

Modifications.

This process can also be performed with additional outputs of interest and/or for one or more outputs at different time points. Here we showed what happens when we look at only one output for each of the runs to simplify the process, but in practice, we looked at the output ratio, $r/(c+r)$, discussed above in step 3, at multiple time points. This allowed us to understand how the influence of a parameter value changes as the tumor grows.

To do this, we used the ratio at each time point as our multiple outputs that are appended to the matrix in step 4, so that it looked something like this:

$$\begin{bmatrix} \eta_c(5) & \rho_c(31) & \cdots & D_r(9) & Ratio(1)_{t=1} & \cdots & Ratio(1)_{t=tfinal} \\ \eta_c(17) & \rho_c(1) & \cdots & D_r(2) & Ratio(2)_{t=1} & \cdots & Ratio(2)_{t=tfinal} \\ \vdots & \vdots & \ddots & \vdots & \vdots & \ddots & \vdots \\ \eta_c(11) & \rho_c(3) & \cdots & D_r(N) & Ratio(N-1)_{t=1} & \cdots & Ratio(N-1)_{t=tfinal} \\ \eta_c(2) & \rho_c(28) & \cdots & D_r(4) & Ratio(N)_{t=1} & \cdots & Ratio(N)_{t=tfinal} \end{bmatrix} \tag{6.12}$$

We then followed the same ensuing steps, arriving at PRCC values for each parameter at each time step, $\phi_{i,tstep}$, such that we had a matrix of PRCCs with dimensions $i \times tsteps$, where $tsteps$ is the number of time steps in our simulation. The same was done for the t-test, with $t_{i,tstep}$.

Then, to visualize our results, the PRCCs and the test statistics for each parameter were plotted against time in Figures 6.4 and 6.5, respectively. This allows us to see when the influence of individual plays the most important role (e.g., early in the simulation versus at longer time scales).

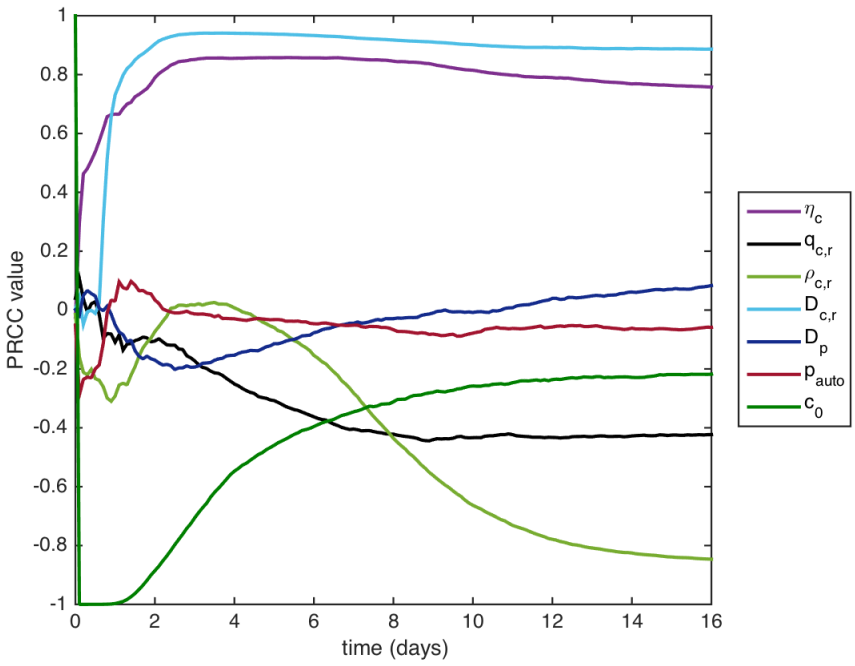

Figure 6.4: **Partial rank correlation coefficients of LHS parameters with recruited ratio vs. time.** Partial rank correlation coefficients (PRCC) were computed between the sampled parameters and the ratio of recruited cells to total tumor cells, $r/(c+r)$ at each time point of the simulations, as described in Section 6.2.2. Plotting these PRCC values across time allows us to see how the sensitivity of the model with respect to the parameters changes over the course of the simulation.

6.3 Results

6.3.1 Most sensitive parameters

Positive correlation. Our sensitivity analysis revealed that the parameters $D_{c,r}$ and η_c, the diffusion rate of transduced and recruited cells and the secretion rate of PDGF by transduced cells, respectively, are most influential upon the ratio of recruited (untransduced)

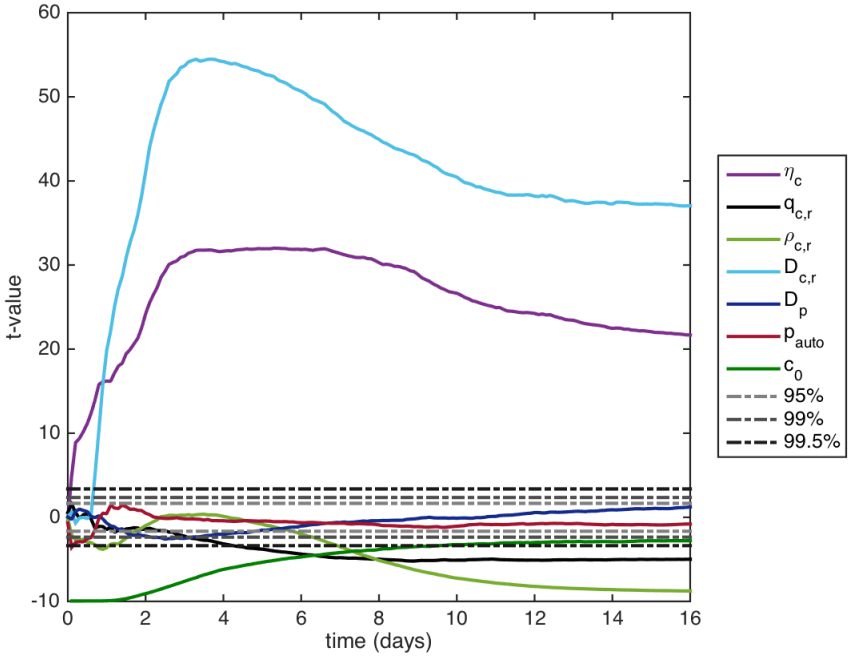

Figure 6.5: **Significance of parameter correlation with recruited ratio vs. time.** Student's t-test statistic was computed with the PRCC for each time point of the simulations, using equation 6.10. These are plotted over time (solid lines), along with lines indicating the thresholds of various confidence intervals (dash dot lines) for our $N = 200$ samples, thereby showing which correlations are significant and when that correlation might become significant or become insignificant.

glial progenitors to total tumor cells (both transduced and recruited), $r/(c+r)$ (Figure 6.4). These parameters are significantly positively correlated with this ratio for the duration of the simulations (Figure 6.5). The significance of η_c on the ratio is unsurprising, since it is by this PDGF secretion that the recruitment of untransduced glial progenitor cells even happens. It is perhaps more surprising that the rate of diffusion is so strongly correlated with this ratio. Likely, this is due to the moving of cells out into the surrounding tissue where there are

recruitable cells (normally present untransduced glial progenitors). Since transduced cells provide a source of PDGF, when they diffuse into the adjacent tissue, the glial progenitors there sense the PDGF and begin responding to it, filling up the space before the transduced cells can proliferate enough to catch up.

Negative correlation. Additionally, there are three parameters that are significantly negatively correlated with the ratio: c_0, $\rho_{c,r}$, and $q_{c,r}$, which are the initial percentage of cells within the injection area that are infected by the retrovirus and become transduced, the proliferation rate of transduced and recruited cells, and the consumption rate of PDGF by transduced and recruited cells, respectively (Figures 6.4 and 6.5). Unlike for the positively correlated parameters, these change over the duration of the simulation. In the first 8 days post injection (dpi), bigger values of c_0 strongly affect the ratio, pulling it downward. This makes sense, since more transduced cells in the initial condition early on lead to more transduced cells later as well. Further, this leaves fewer cells to be recruited in the injection area, leading to a small decrease in recruited cells at early time points. However, as the tumor dynamics proceed, the effects of the initial condition wane and become less significant. After those first 8 dpi, we see that $\rho_{c,r}$ becomes significantly influential. It is perhaps surprising that the proliferation rate is negatively correlated with the ratio of tumor cells. It could be that having more cells consuming the PDGF, and thus lowering the overall level of available PDGF, gives an advantage to cells that also make their own PDGF. We also see $q_{c,r}$ becoming significantly negatively correlated with the ratio after 6 dpi. This would similarly lower the overall level of available paracrine PDGF for the recruited cells, thereby advantaging the transduced cells that make PDGF and have an autocrine signal.

6.3.2 Least sensitive parameters

There were two parameters that showed no or little significant correlation with the ratio: D_p and $p_{autocrine}$, the diffusion rate of PDGF and the level of autocrine PDGF signal, respectively. These so some significance at early time points, but it is very short lived, in the case

of p_{auto}, and not very significant in comparison with other parameters, in the case of D_p. p_{auto} is significantly negatively correlated at the very beginning. This is likely related to the establishment of the inital cell population.

The diffusion rate of PDGF, D_p, seems like it would be a more significant paramter, since higher rates of diffusion of PDGF means that the PDGF is leaving the local area rather than staying available to drive the continued proliferation of recruited glial progenitor cells. However, the decrease in its significance after 5 dpi is possibly related to the cellular density—no matter how much PDGF there is or is not, high cellular density will decrease the proliferation of recruited cells, making the role of D_p less significant. It could also be related to a saturation of PDGF; if there is sufficient PDGF, the highest values of D_p that we tested may not be enough to make a "dent" in the PDGF supply.

6.4 Discussion

The Latin hypercube sampling (LHS) technique allowed us to run simulations that fully sample the parameter space, and through the use of partial rank correlation coefficients (PRCC), to understand how our parameters influence model outcomes. Here we have only shown one model outcome, the ratio of recruited cells to total tumor cells, $r/(c+r)$, though we have used it to look at other simulation outcomes as well. Since we had experimental data on this recruited ratio and it was one of the most important aspects for our model to fit, this technique helped us to narrow our possible parameter values to those that best helped us to achieve this ratio.

Fortunately, we had an abundance of cell tracking data available to use for parameterizing the cellular diffusion rates, $D_{c,r}$, since it was the most sensitive parameter. This data also allowed us to observe cell division, which helped us to parameterize the proliferation

rates, $\rho_{c,r}$. However, the second most sensitive parameter, η_c, the secretion rate of PDGF by transduced cells, we have no data for. We also had no data available for the rates of consumption of PDGF by transduced and recruited cells, $q_{c,r}$. This was very challenging to the parameterization of the model, but knowing that they were significantly (positively and negatively) correlated with the ratio allowed us to select values that gave us the correct ratio of recruited cells.

In addition to being a great tool for parameterizing a model (i.e., aid in selecting parameter values), it can also help us see they way in which model parameters affect the model overall. By varying the parameters, we see them almost more as variables in the system, seeing how a change in one affects the model outcomes. In the results section 6.3, some possible reasons for the observed correlations were provided. One was that density and/or PDGF saturation might have been the reason that D_p is not significantly correlated with the outcome. The model is less sensitive to the value of D_p than we first expected, but upon thinking about the possible reasons for this, we understood that it fit with our biological understanding of the tumor (at 10 days post injection, animals had sizable, dense tumors where the movement of PDGF was likely not as important as that of the vast quantity of cells producing the PDGF). Thus, while sensitivity analysis via LHS and PRCC cannot tell us *why* a particular correlation was observed, it does indicate *how* a parameter affects the overall outcome. As we consider the possible reasons for the observation, this can provide insight into the behavior of the model, which can in turn help to ensure that our model best reflects the biological mechanisms we are studying.

Chapter 7

2-DIMENSIONAL PROLIFERATION–INVASION–RECRUITMENT MODEL IMPLEMENTED ON A MOUSE BRAIN ATLAS

This chapter consists of a paper submitted to the Bulletin of Mathematical Biology in July 2016 for a special feature issue on Mathematical Oncology. Additional related material is given in an appendix section at the end of the chapter.

Massey, S. C., Rockne, R. C., Hawkins-Daarud, A., Gallaher, J., Anderson, A. R. A., Canoll, P., Swanson, K.R. Simulating PDGF–driven Glioma Growth and Invasion in an Anatomically–Accurate Brain Domain. *Bulletin of Mathematical Biology*, in review, 2016.

Abstract

Gliomas are the most common of all primary brain tumors. They are marked for their diffuse infiltration of the brain tissue, and are uniformly fatal. In recent years, the over-expression of platelet-derived growth factor (PDGF) has been shown to produce tumors in experimental rodent models that closely resemble this human disease [9,35], specifically proneural glioblastomas (a subtype of glioma). We have previously modeled this system, focusing on the key attribute of these experimental tumors—the "recruitment" of oligodendroglial progenitor cells to participate in tumor formation by PDGF–expressing retrovirally transduced cells—in one dimension, with spherical symmetry [67]. However, it has been observed that these recruitable progenitor cells are not uniformly distributed throughout the brain [79, 83, 87] and that tumor cells migrate at different velocities depending on the material properties of the different tissues in the brain [24]. Here we model the differential diffusion of PDGF–

expressing and recruited cell populations via a system of partial differential equations (PDEs) with spatially variable diffusion coefficients, and solve the equations in two spatial dimensions on a mouse brain atlas using a flux–differencing numerical approach. Simulations of our *in silico* model demonstrate qualitative agreement with observed tumor distribution patterns in the experimental animal system. Additionally, it was observed that tumor simulations with greater degrees of recruitment grow faster and that the recruitment process produces more nodular tumors than if there there is no recruitment at all, similar to our prior results from implementing our model in one dimension [67]. Simulations with greater difference in the rates of diffusion in gray versus white matter display a greater preponderance of tumor cells in the white matter structures of the brain. Combined, these results show that recruitment remains an important consideration in understanding and stopping glioma growth.

7.1 Introduction

Glioblastoma (GBM) is an aggressive cancer and is the most common primary brain tumor in adults. Malignant glioma cells are highly infiltrative of the normal surrounding tissue; however, the tumor cells rarely metastasize out of the central nervous system (CNS). The diffuse migration of tumor cells, combined with the complex spatial heterogeneity of brain tissue, leaves a large portion of the tumor cells invisible to clinical magnetic resonance imaging (MRI). This diffuse invasion is a hallmark of gliomas which presents many challenges for treatment and disease monitoring, particularly in the early stages of tumorigenesis, making *in vivo* and *in silico* tumor models especially important in gaining understanding of this disease.

Animal studies utilizing platelet-derived growth factor (PDGF) have provided improved models of glioma growth and evolution which recapitulate the diffuse, differential invasion of tumor cells within different regions of the brain [9, 10, 35]. These models demonstrate that PDGF-expressing retroviral injection into neonatal or adult rodent brain will induce the formation of glioma-like tumors (Figure 7.1) that appear histopathologically identical to human glioma [9,10,27,113]. Moreover, use of retroviruses that express higher levels of PDGF drives

the formation of more rapidly growing and higher-grade gliomas, which exhibit robust vascular proliferation and necrosis [90]. Much of this rapid growth is attributable to the observed phenomenon that, in this animal model, oligodendroglial progenitor cells (OPCs) transduced with the PDGF-expressing retrovirus recruit other, untransduced OPCs [9]. OPCs express the platelet-derived growth factor receptor PDGFRα, enabling them to participate in autocrine and paracrine PDGF signaling loops with the PDGF secreted by the retrovirally transduced OPCs. Thus, the paracrine PDGF signal from the transduced OPCs to the untransduced OPCs causes the observed recruitment, whereby untransduced cells show increased proliferation and migration rates consistent with cancer cells, and contribute to the bulk of the tumor, comprising as much as 80–90% of the overall mass. The transduced cells respond likewise, responding to the PDGF secreted by themselves and other nearby transduced OPCs, but make up a smaller proportion of the experimental tumors [9].

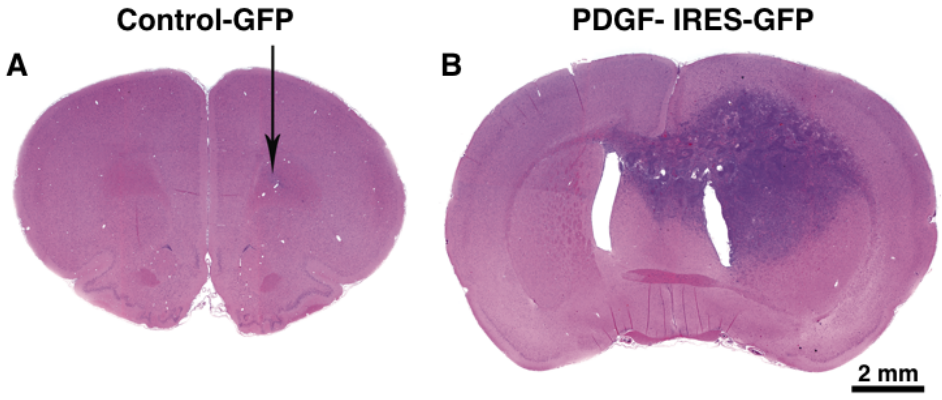

Figure 7.1: **Rodent brain slices.** No tumors formed in rodents injected with control retrovirus, which lacked the PDGF-expressing region (**A**), yet tumors formed in 100% of rodents injected with PDGF-expressing retrovirus (**B**). The observed tumor shape in (**B**) suggests differential rates of tumor cell migration, with strong preference for migration along the myelinated axons across the corpus callosum. *Figure reproduced from* [9].

To better understand the experimental results from these animal studies and their possible correlation to human disease, we previously adapted a reaction–diffusion model of glioma growth in humans [41], which we refer to as the "Proliferation–Invasion" (PI) model, to include a recruitment process. This model, which we have termed the "Proliferation–Invasion–Recruitment" (PIR) model [67], consists of four coupled partial differential equations. In this previous work, we assumed a simplified homogeneous brain, and solved our equations in one dimension with spherical symmetry. However, the experimental data (see Figure 7.1) motivates a reaction–diffusion model for tumor growth and migration which includes tissue-dependent differential rates of diffusion. Moreover, it is understood that the migration rates of glioma cells along myelinated axons, which compose the white matter of the brain, are up to 100-fold faster than in the dense gray matter of neuronal bodies and dendrites which compose the cortex [24, 41]. Thus, because glioma cells have been observed to move much more quickly along white matter tracts, migration not only depends on the local cellular density and the relative PDGF concentration gradient, which stimulates both migration and proliferation, but also upon the tissue properties.

To account for this and to ascertain the contribution of these differential diffusion rates, we have adapted our PIR model to run our simulations on a two-dimensional mouse brain map. We then take the diffusion coefficient to be defined through a piecewise constant function, where both transduced and recruitable glial progenitor cells traveling in white matter take on a faster rate than those traveling in gray matter. We show that differential diffusion rates allow for better morphological agreement between simulation and experiment, and that while these differential rates do not contribute largely to the overall speed of tumor growth, they do affect the relative preponderance of tumor cells (i.e., both transduced and recruitable OPCs) in the white and gray matter regions.

7.2 Proliferation-Invasion-Recruitment Model, in Two Spatial Dimensions

In the present model, there are three variables of interest: density of *transduced* cells (c) which have been caused by retroviral injection to over-express platelet-derived growth factor, density of *recruitable* oligodendroglial progenitor cells (r), and the concentration of PDGF (p). The proliferation-invasion-recruitment (PIR) model equations account for the proliferation and diffusion of both transduced and untransduced ("recruitable") oligodendroglial progenitor cells (OPCs), at rates $\rho_{c,r}$ and $D_{c,r}$, respectively, where the subscripts denote the relevant cell type. Additionally, it includes the production of PDGF by transduced cells and the consumption of PDGF by both cell types, at rates η_c and $q_{c,r}$, respectively. These contribute to the PDGF-driven recruitment of the recruitable OPCs, r, by setting up localized gradients of PDGF, which can also diffuse at rate D_p. We have schematized the model in Figure 7.2.

7.2.1 Model Equations

The equations for our model are as follows:

$$\overbrace{\frac{\partial c}{\partial t}}^{\substack{\text{rate of change}\\ \text{of transduced}\\ \text{cell density}}} = \overbrace{\nabla \cdot \left(\overline{D}_c\left(c, r, p, \vec{x}\right) \nabla c\right)}^{\substack{\text{net dispersal}\\ \text{of transduced cells}}} + \overbrace{\overline{\rho}_c\left(c, r, p, \vec{x}\right) c}^{\substack{\text{net proliferation}\\ \text{of transduced cells}}} \tag{7.1}$$

$$\overbrace{\frac{\partial r}{\partial t}}^{\substack{\text{rate of change}\\ \text{of recruitable}\\ \text{cell density}}} = \overbrace{\nabla \cdot \left(\overline{D}_r\left(c, r, p\right) \nabla r\right)}^{\substack{\text{net dispersal}\\ \text{of recruitable cells}}} + \overbrace{\overline{\rho}_r\left(c, r, p, \vec{x}\right) r}^{\substack{\text{net proliferation}\\ \text{of recruitable cells}}} \tag{7.2}$$

$$\overbrace{\frac{\partial p}{\partial t}}^{\substack{\text{rate of change}\\ \text{of PDGF}\\ \text{concentration}}} = \overbrace{\nabla \cdot \left(D_p \nabla p\right)}^{\substack{\text{dispersal}\\ \text{of PDGF}}} + \overbrace{\eta_c c}^{\substack{\text{secretion}\\ \text{of PDGF by}\\ \text{transduced}\\ \text{cells}}} - \overbrace{q_r \beta\left(p\right) r}^{\substack{\text{consumption}\\ \text{of PDGF by}\\ \text{recruited}\\ \text{cells}}} - \overbrace{q_c \beta\left(p\right) \alpha c.}^{\substack{\text{consumption}\\ \text{of PDGF by}\\ \text{transduced}\\ \text{cells}}} \tag{7.3}$$

Equations (7.1) to (7.3) are reaction–diffusion equations describing the movement of cells and PDGF, as well as their synthesis, and in the case of PDGF, consumption. Notice that

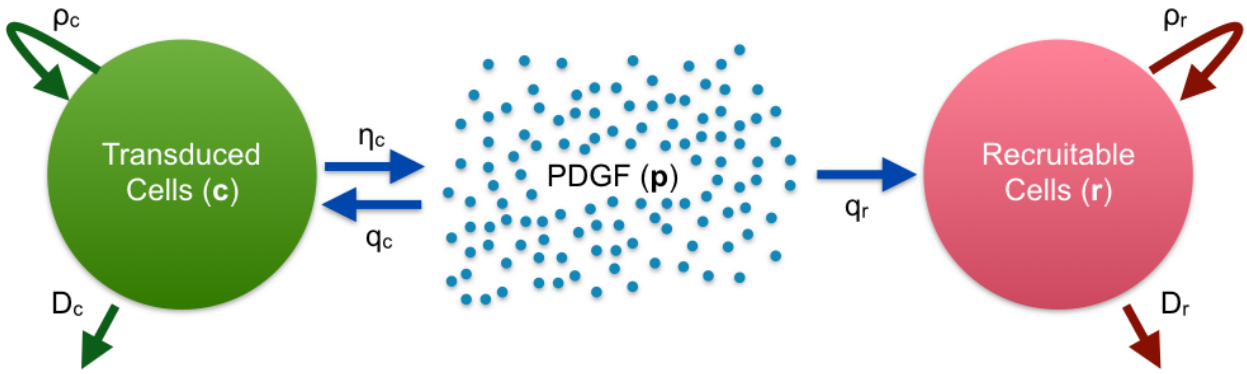

Figure 7.2: **Schematic representation of the model.** Transduced cells (c, shown in green) produce PDGF (p, shown in blue) at rate η_c; PDGF (p) is consumed by both transduced (c) and recruitable (r, shown in red) glial progenitor cells at rates q_c and q_r, respectively. PDGF stimulates proliferation and diffusion of infected glial progenitor cells at rates ρ_c and D_c, respectively, and of uninfected progenitors at rates ρ_r and D_r. Note that PDGF molecules can also diffuse. Equations relating these are given in Section 7.2, and Table 7.1 lists the parameters and the values used.

the diffusion and proliferation rates in (7.1) and (7.2) are density-dependent and PDGF-dependent. Accounting for these dependencies, the diffusion and proliferation rates take the form:

$$\overline{D}_c\left(c,r,p,\vec{x}\right) = D_c\left(\vec{x}\right)\frac{\beta\left(p+p_{auto}\right)}{\beta\left(EC_{50}\right)+\beta\left(p+p_{auto}\right)}\left(1-\frac{c+r}{K}\right) \tag{7.4}$$

$$\overline{D}_r\left(c,r,p,\vec{x}\right) = D_r\left(\vec{x}\right)\frac{\beta\left(p\right)}{\beta\left(EC_{50}\right)+\beta\left(p\right)}\left(1-\frac{c+r}{K}\right) \tag{7.5}$$

$$\overline{\rho}_c\left(c,r,p\right) = \rho_c\frac{\beta\left(p+p_{auto}\right)}{\beta\left(EC_{50}\right)+\beta\left(p+p_{auto}\right)}\left(1-\frac{c+r}{K}\right) \tag{7.6}$$

$$\overline{\rho}_r\left(c,r,p\right) = \rho_r\frac{\beta\left(p\right)}{\beta\left(EC_{50}\right)+\beta\left(p\right)}\left(1-\frac{c+r}{K}\right) \tag{7.7}$$

where the PDGF receptor binding kinetics are described by:

$$\beta\left(p\right) = \frac{p}{k_m+p} \tag{7.8}$$

$$\alpha = 1 - \beta(p_{auto}). \tag{7.9}$$

While these rates (7.4) to (7.7) look quite complicated, they can be broken down into three constituent parts: rate parameter, PDGF dependence, and density dependence. The density dependence ensures that we never exceed the carrying capacity. Although this is traditionally not needed in the diffusion term for a single species, in our model, the sum of both cell types is subjected to a single carrying capacity, making this a necessary component our cellular diffusion rate terms. PDGF dependence in our rates is motivated by experimental data, which demonstrate that the motility and cell division rates of OPCs are dependent on local PDGF concentration [7, 36, 81]. These rates are modulated both by PDGF receptor binding kinetics (which also modulate the PDGF consumption rates) and by what we call downstream dose-response. The PDGF receptor binding kinetics given in (7.8) are based on Michaelis-Menten enzyme kinetics, with the traditional parameter k_m being the concentration of PDGF at which half of the maximal binding rate is achieved. However, this is insufficient to describe the downstream proliferation and migration dose responses to PDGF, leading to our derivation of the more complicated ratio of β's. This is explained more thoroughly in [67], but essentially allows for the incorporation of the "downstream" dose response, with parameter EC_{50}, and the receptor binding, with parameter k_m, in a way that fits the data. The addition of the parameter p_{auto} allows us to include effects of autocrine signaling by transduced cells, which is also more thoroughly explained in [67]. Finally, the proliferation rate parameters are fixed, but we allow the diffusion parameters to vary spatially.

The rates of diffusion in (7.4) and (7.5) are functions of the spatial variable $\vec{x} = (x, y)$. It is assumed that these functions are piecewise constant depending on the local tissue properties, specifically, whether it is gray or white matter:

$$D_{c,r}(\vec{x}) = \begin{cases} D_{(c,r)w} & \text{for } \vec{x} \in \text{white matter} \\ D_{(c,r)g} & \text{for } \vec{x} \in \text{grey matter} \\ 0 & \text{for } \vec{x} \notin \text{brain tissue} \end{cases} \tag{7.10}$$

as is similarly done in proliferation invasion (PI) model simulations implemented on a brain atlas [97, 98]. We assume that these differential rates are related as follows:

$$D_{(c,r)w} = R_{wg} D_{(c,r)g}. \tag{7.11}$$

where the unitless parameter $R_{wg} > 1$, since cell migration is faster in white matter than in gray. In practice, when running simulations, we let D_c and D_r represent the migration rate in gray matter, and by varying R_{wg} in simulations, increase the diffusion rates of the cells to be R_{wg} times faster in white than in gray. These and all other parameters are listed in Table 7.1.

The model equations we have presented here are more thoroughly derived in the supplemental material of [67], where we developed a one–dimensional model of the experimental PDGF–driven tumors. However, the model presented here differs slightly from that in [67] in a few ways. First, by implementing our model in two dimensions we are able to incorporate different diffusion rates in gray versus white matter regions, as given by (7.10) and (7.11). Second, we have omitted chemotaxis. While there is evidence that OPCs chemotax in gradients of PDGF [7], there is also evidence that these cells move in response to PDGF in a way that is not chemotactic [36]. Based on the cell tracking work we have done [49, 67], our analysis indicates that the movement of these cells can be mathematically modeled sufficiently using diffusion alone—therefore taxis or directed migration terms are not included. Finally, a third change is the lack of an equation for the remaining brain cells which do not actively participate in the formation of tumors. These cells do contribute to total cell density and thus are related to density-dependence; however, we make the simplifying assumption that they are passive and die as the tumor expands, making their contribution to the tumor dynamics negligible.

7.2.2 Initial and Boundary Conditions.

Initial Conditions. To set the initial conditions for this problem, we take the baseline population of glial progenitor cells (OPCs) in normal healthy brain tissue (given by parameter

Table 7.1: **Model Parameters and their Values.** The derivation of most parameters can be found in [67] and its supplemental material. Many are experimentally derived, or came from a combination of literature sources and testing in simulations. (*) Note that the value given here for R_{wg} comes from varying the parameter in simulations, as described in the results in Section 7.3.

Symbol	Definition	Value	Units	Source
D_c	max diffusion rate of transduced cells	5.8×10^{-5}	$\frac{cm^2}{day}$	[67]
D_r	max diffusion rate of recruited cells	5.8×10^{-5}	$\frac{cm^2}{day}$	[67]
R_{wg}	ratio of diffusion rates in white vs. gray	10	unitless	*
D_p	diffusion rate of PDGF	5×10^{-4}	$\frac{cm^2}{day}$	[67, 105]
ρ_c	max proliferation rate of transduced cells	$\frac{ln(2)}{18/24}$	day^{-1}	[67]
ρ_r	max proliferation rate of recruited cells	$\frac{ln(2)}{18/24}$	day^{-1}	[67]
η_c	rate of PDGF secretion by transduced cells	10^{-5}	$\frac{ng/cell}{day}$	[67]
q_c	max rate of PDGF uptake by transduced cells	$10^{-5.15}$	$\frac{ng/cell}{day}$	[67]
q_r	max rate of PDGF uptake by recruited cells	$10^{-5.15}$	$\frac{ng/cell}{day}$	[67]
K	cellular carrying capacity	2.3×10^8	$\frac{cells}{mL}$	[67]
k_m	[PDGF] at which half max binding occurs	30	$\frac{ng}{mL}$	[67, 81]
EC_{50}	[PDGF] achieving half max dose response	$10^{1/2}$	$\frac{ng}{mL}$	[67]
p_{auto}	autocrine PDGF level for transduced cells	1	$\frac{ng}{mL}$	[67]
$O2a$	baseline population of OPCs in gray matter	2.2×10^6	$\frac{ng}{mL}$	[67]

$O2a$), and define a spherical region around the site of the injection wherein we assume that most (99%) of these progenitor cells are infected:

$$c_0(\vec{x} = \mathcal{R}, t = 0) = \begin{cases} 0.99 \cdot O2a(\vec{x}) & \text{for } \mathcal{R} < 0.03 \text{ cm} \\ 0 & \text{else} \end{cases} \tag{7.12}$$

where

$$\mathcal{R}^2 = (x - x_{injection})^2 + (y - y_{injection})^2 \tag{7.13}$$

is the radial distance from the injection site $(x_{injection}, y_{injection})$.

Any OPCs inside and outside of this region that are not infected following the injection, and thus not transduced, are considered to be "recruited" and "recruitable" cells, respectively.

$$r_0(\vec{x} = \mathcal{R}, t = 0) = \begin{cases} 0.01 \cdot O2a(\vec{x}) & \text{for } \mathcal{R} < 0.03 \text{ cm} \\ O2a(\vec{x}) & \text{else.} \end{cases} \tag{7.14}$$

Note that $O2a(\vec{x})$ is spatially dependent, since there are more OPCs in white matter than in gray matter. In practice, we let $O2a$ represent the density of these cells in gray matter and set $8/3 \cdot O2a$ represent the density in white matter, since OPCs make up approximately 3% of the normal gray matter and about 8% of the normal white matter [79, 83, 87]:

$$O2a(\vec{x}) = \begin{cases} O2a & \vec{x} \in \text{gray matter} \\ \frac{8}{3}O2a & \vec{x} \in \text{white matter.} \end{cases} \tag{7.15}$$

The injection site for our simulations was chosen by determining the approximate center of the tumor in Figure 7.1B and selecting a similar location in the computational domain specified by the brain atlas.

For the initial PDGF concentration, we take

$$p_0(\mathcal{R}, 0) \equiv 0$$

since we assume that there is no PDGF in the tissue until it is secreted by the transduced cells. In reality, there may be some small amount released in response to the injury of injecting the brain; however, we assume that to be negligible.

Boundary Conditions. The physical boundary conditions of the problem are no-flux of tumor cells outside of the brain $\mathcal{B}$, so that

$$\nabla q \cdot \vec{n} = 0 \tag{7.16}$$

where $\vec{n}$ is the vector normal to the boundary $\partial\mathcal{B}$.

Computational Domain. We utilize a brain atlas [62, 63] to define our computational domain. This atlas specifies, on a Cartesian grid with resolution 0.01 cm, the gray and white regions inside the brain where the tumor may grow, as well as the ventricles and anything outside the brain where it does not. (The brain atlas we used is open source; details may be found online at `http://brainatlas.mbi.ufl.edu`.)

7.2.3 Numerical Method

To implement our model, we use a fractional step approach. First, we use Godunov operator splitting to solve the reaction and diffusion terms separately. Further, we split the spatial dimensions to turn our two–dimensional problem into a sequence of two locally one–dimensional (LOD) problems. At each iteration of our method, we first solve the diffusion component, coupling the LOD technique with the Crank Nicholson (CN) method. This allows us to solve in the x– and then the y–directions in two sweeps, rather than using a ten point CN stencil, greatly increasing computational efficiency. Next, we solve the reaction terms using the TRBDF2 (trapezoidal rule and 2–step backward differentiation formula) method.

7.3 Simulation Results

7.3.1 Qualitative match between 2d simulation and experimental tumor

Simulations of the two-dimensional PIR model display similar patterns of invasion as those observed in the experimental murine system (Figure 7.3). In particular, the gray and white matter heterogeneity allows for good morphological agreement with experimental murine

tumors. The former one–dimensional model only simulated tumors to grow in a spherical shape, while the experimental tumors show a clear preference for growing along white matter tracts (Figure 7.3A). The addition of both the spatially heterogeneous initial condition for recruitable OPCs (Section 7.2.2) and the differential cellular diffusion rate in gray vs. white matter (Equations 7.10 and 7.11) contribute to the improved agreement between model simulations and the spatial distribution of tumor cells in the animal model. Specifically, by incorporating a 10-fold higher diffusion rate in white matter than in gray (i.e., setting R_{wg}, which is defined as the ratio D_w/D_g, equal to 10), we observe a similar pattern of growth in our model simulations. Values of R_{wg} smaller than 10 look more spherical, and values of R_{wg} greater than 10 appear to travel much further along the white matter tracts (see Figure 7.6 or 7.7 for examples of simulations with lower and higher values of R_{wg}). Since we had more data for the initial distribution of recruitable OPCs, we did not vary the percentages in gray or white matter. The effects of varying R_{wg} are explored more in section 7.3.3.

7.3.2 PDGF secretion rates positively correlate with tumor growth rates, but the recruitment process results in more nodular tumors.

We simulated tumors with different values of PDGF secretion rate, η_c, for 30 days and then compared results at that time point to look at how this parameter affects the speed of overall tumor growth. Our results show that the tumors with little or no PDGF secretion are significantly smaller than those with moderate or high PDGF secretion (Figure 7.4 A–C). This demonstrates that PDGF secretion, and thus recruitment, greatly contributes to the speed at which these tumors grow, with higher secretion resulting in fast-growing tumors, and low secretion resulting in relatively slow-growing tumors.

Next, we compared tumor simulations with the different rates of PDGF secretion (i.e., different values of η_c) at the same size as detected by T1 MRI. To do this, we simulated tumors until they had an average radius of 0.2 cm (2 mm) at the density threshold which roughly

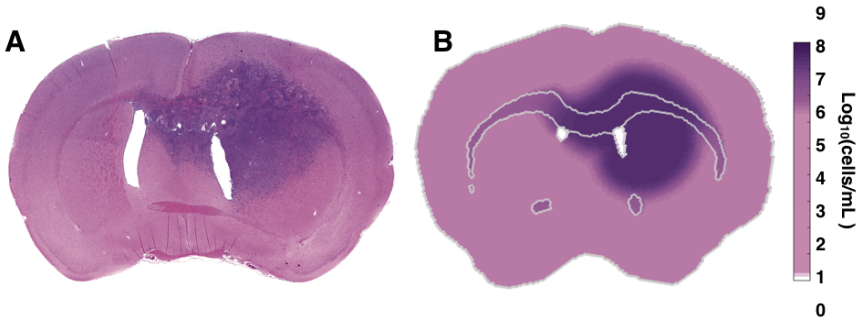

Figure 7.3: **Comparison of simulated tumor and H&E of experimental PDGF-driven tumor.** (**A**) Tissue slice from an experimental PDGF-driven tumor stained with hematoxylin and eosin (H&E), (*reproduced from* [9]). (**B**) simulated tumor using our 2D PIR model implemented on a rodent brain atlas, with parameter $R_{wg} = 10$. Color bar is on a log scale and shows the total density of recruitable and transduced cells. Gray outlined region in the middle shows the corpus callosum. The purple region shows the area where the tumor resides, while the pink is primarily reflective of the baseline density of recruitable cells.

corresponds to tumor detectability on T1 MRI—we take this to be 80% of carrying capacity. This comparison reveals that the tumors with less recruitment are more diffuse (Figure 7.5). Specifically, the tumor with no PDGF secretion, and thus no recruitment, has a more extensive region of tumor extending beyond the 80% density visible on T1 MRI, showing the greatest degree of diffuse invasion. The tumor with the most recruitment (on the right) has the least amount of tumor extending beyond the 80% density visible on T1 MRI, making it the least diffusely invasive.

In the aforementioned simulations and associated figures, we did not vary R_{wg} but held it fixed at 10 (as discussed in Section 7.3.1). This enabled us to examine the spatially dependent changes that occur due to tumor growth in gray vs. white matter brain regions without

the additional signal of varied magnitude. Looking across two different axes of the tumor, one in gray matter only, and the other passing through the white matter (labeled x and y, respectively, in both Figures 7.4 and 7.5), we can see the effect of having a differential diffusion rate upon the cellular density and the proportion of tumor that is made up of recruited cells. In the white matter, we see that the tumor cell density curve is less steep due to increased diffusion in this region (compare Figure 7.4C with Figure 7.4B, and likewise, Figure 7.5C with Figure 7.5B). There is also a slight increase in cell density in this region due to the presence of more background recruitable cells in the white matter. Correspondingly, the proportion of tumor made up by recruited cells is a bit higher at the leading "edge" when it is in white matter (compare Figure 7.5E with 7.5D), while increases are less steep in this region (compare Figure 7.4E with 7.4D). This is likely due to both the increase in background recruitable cells in the white matter, as well as the increased invasion rate of transduced cells happening at the "edge"—the transitional zone from dense tumor to normal brain, where there are mostly only recruitable OPCs (recruited fraction near 1)—when it passes through the white matter region. Note that the increases in Figure 7.5D and E for the curves at approximately 0.3 cm is due to cells diffusing out of the corpus callosum, just beyond the left end of the axis labeled x, into the gray matter. That is, cells and PDGF diffusing toward the right out of the corpus callosum increase the number of recruited cells in that region.

7.3.3 Significance of gray vs white matter diffusion rates.

To better understand the contribution of differential rates of diffusion in gray versus white matter, as separate from that of PDGF secretion rate, we ran a series of simulations varying both independently. We ran 16 simulations, with four values of R_{wg} and four values of η_c, and compared the results at similar tumor sizes (at the 80% density threshold that would be detectable on T1 MRI). The comparisons we focused on were the fraction of total tumor that resided in the white matter regions of the brain, as well as the time it took for the tumors to reach the given size, essentially indicating the speed of growth.

The first of these, fraction of tumor cells in white matter regions, increases both with increasing R_{wg} and with increasing η_c; however, at most sizes it is much more strongly affected by R_{wg} (Figure 7.6). At large tumor sizes, the fraction decreases, corresponding to the tumor growing beyond the size of the white matter regions. Note that at the smallest tumor size here, 0.1 cm T1 radius, the infiltrating "edge" of the tumor is close to the edge of the corpus callosum. Therefore, the tumors (initiated in gray matter) would not be expected to have a sizable fraction of cells inside the white matter, and any slight increase in size would cause many more cells to cross over into the corpus callosum and thus be in white matter, increasing the fraction. This is the likely cause for the apparent disruption of the observed pattern in this particular subplot as opposed to the others in Figure 7.6. That is, since the size is not in fact exact, but is a rounded figure, the slight variation in size among these simulations at this particular T1 radius could cause a big difference in the amount of tumor inside the white matter. Overall, the relationship between the fraction of tumor in white matter and R_{wg} suggests that tumors showing a proclivity for white matter regions may have greater differential rates of cellular diffusion in white matter than in gray.

In our second comparison, time duration of growth required to reach specific sizes at the 80% of carrying capacity density threshold that is detectable on T1 MRI, we see that while both R_{wg} and η_c correspond with faster growth, η_c is the most influential parameter (Figure 7.7). These heat maps show that the speed of these tumors' growth depends highly on the rate of PDGF secretion, and thus the degree of recruitment. This relationship is particularly pronounced at smaller tumor sizes, where R_{wg} appears to have very little effect. At extremely large tumor sizes, where the size of the dense tumor core approaches the size of the brain itself, R_{wg} appears to play a greater role in contributing to this speed of growth. However, this likely is of little practical importance, since tumors are typically lethal prior to reaching such large sizes. The result that recruitment plays a significant role in the growth rate of tumors suggests that reducing PDGF signal, perhaps through use of PDGF inhibitor

therapies or other drugs targeting the PDGF pathway, could greatly slow the growth of tumors that show a high degree of OPC recruitment.

7.4 Discussion

We have shown that our reaction-diffusion PDE model for glioma growth reproduces the growth patterns observed *in vivo* (Figure 7.3). The morphology of the tumor growth depends critically on differential rates of migration of tumor cells through the brain. Without the differential rates, we would obtain spherical symmetry equivalent to that in the one dimensional PIR model [67]. On the other hand, the degree to which the rate of diffusion in white matter exceeds that of gray matter, can greatly affect the shape and location of the tumor cells (Figures 7.4–7.7). Having greatly different rates can lead to tumors that fill the entire corpus callosum of the brain within a short period of time. Interestingly, this is consistent with observations from human patients, some of whom have tumors that are said to display a "preference" for white matter, or whose tumors are described as "white matter disease." It is likely that the cause of this preference in humans is not unlike that in our simulations of the experimental PDGF-driven tumors in rats.

Additionally, we found that the recruitment process results in a less diffuse, faster growing tumor, which is consistent with what we found using the one–dimensional spherically symmetric PIR model [67]. Importantly, we are able to observe that this is preserved with the addition of differential diffusion rates between gray and white matter (Figures 7.4 and 7.5). Further, the preservation of the effect of PDGF secretion rate on the overall speed of tumor growth in the presence of a broad range of differential diffusion rates in gray and white matter suggests that recruitment is an important factor to consider in human glioblastoma. Our results suggest that more rapidly growing untreated human tumors might be more likely to show recruitment of oligodendroglial progenitor cells. Interrupting the paracrine signaling that leads to recruitment could then be key to slowing the growth of these more rapidly growing tumors, and lead to longer patient survival times.

7.5 Appendix: Details of Numerical Method

Here we present the details of the numerical methods.

Notation. Together, the equations describing the change in our three variables with respect to time comprise a reaction-diffusion system of the form

$$u_t = \mathcal{D}(u) + \mathcal{R}(u) \tag{7.17}$$

where $\mathcal{R}$ and $\mathcal{D}$ are reaction and diffusion operators respectively, and u, u_t are the vectors of variables and their derivatives, respectively:

$$u = \begin{bmatrix} c \\ r \\ p \end{bmatrix}, \text{ and } u_t = \begin{bmatrix} c_t \\ r_t \\ p_t \end{bmatrix}. \tag{7.18}$$

For convenience, let U represent the numerical solution of the system, with $U^n_{x,y}$ indicating the numerical solution at time $t = n$ and grid location x, y.

7.5.1 Fractional Step Method and Operator Splitting

We computed the reaction and diffusion terms separately using a fractional step method, acheived via operator splitting. For simplicity, we have chosen to use Godunov splitting, although this method is only first order accurate.

The Godunov splitting scheme can be represented as follows:

$$U^{n+1} = \mathcal{D}(\Delta t)\mathcal{R}(\Delta t)U^n \tag{7.19}$$

Essentially, this says that at the start of a new time step, $n + 1$, we first solve the diffusion problem (using the solution U^n from the previous time step, n), and call this intermediate solution U^*:

$$U^* = \mathcal{D}(\Delta t)U^n. \tag{7.20a}$$

Next, we use that solution (U^*) in the reaction operator, and use the result to update the solution U^{n+1} at the current time step, $n+1$:

$$U^{n+1} = \mathcal{R}(\Delta t)U^*. \tag{7.20b}$$

Following this, we advance to the next time step and repeat the process until we reach the desired time length of the simulation.

7.5.2 Diffusion Terms

To solve the diffusion problem and simulate the diffusion of the cells and PDGF through the domain, we used a Locally One Dimensional (LOD) method in conjunction with the Crank-Nicolson numerical method.

Since we are working in 2 dimensions, we need to account for diffusion-driven flux from each grid cell in both the x and y directions. This can be accomplished with a large sparse matrix and stencil, but we found it more convenient (and faster) to split in x and y. This splitting results in an LOD method where we look at all the fluxes in the x–direction and those in the y–direction separately.

First, recall the Crank Nicholson method

$$U^{n+1} = U^n + \frac{k}{2}\left(F\left(U^{n+1}\right) + F\left(U\right)\right). \tag{7.21}$$

Now since

$$U^{n+1} = U^n + \Delta U, \tag{7.22}$$

we can write (7.21) as

$$U^n + \Delta U = U^n + \frac{k}{2}\left(F\left(\Delta U\right) + F\left(U\right)\right), \tag{7.23}$$

which gives us that

$$\Delta U = \frac{k}{2}\left[2F\left(U^n\right) + F\left(\Delta U\right)\right] \tag{7.24}$$

$$= kF\left(U^n\right) + \frac{k}{2}F\left(\Delta U\right), \tag{7.25}$$

an implicit equation for ΔU. We can solve this equation for ΔU using the conjugate gradient method, and use our result to update our solution at the next time step: $U^{n+1} = U^n + \Delta U$.

To solve 7.25, we need to determine the flux, F. This is where the locally one dimensional (LOD) technique comes in—we compute F separately for the x– and y–directions. In order to effectively do this, we take the $M \times N$ grid, and, excluding the boundaries, shape it into two vectors of length $MN-$boundary cells: one for the x-direction, the other for the y-direction. Each element of the vectors contains an index for center of each grid cell - we can think of it as being like a node. As we change our grid in this way, we also have corresponding vectors for the diffusion weights (i.e, depending on whether the grid cell is in white or gray matter, we weigh diffusion as described in (7.10); this information is passsed on to new vectors that correspond to the two x– and y–going vectors described above.

Since our diffusion coefficent depends on our variables, at the beginning of each time step $n+1$, we use the values of our variables at the previous time step $c^n = c(t = n, \vec{x})$, $r^n = r(t = n, \vec{x})$, and $p^n = c(t = n, \vec{x})$, to compute:

$$\frac{\beta(p^n + p_{auto})}{\beta(EC_50) + \beta(p^n + p_{auto})}\left(1 - \frac{c^n + r^n}{K}\right) \tag{7.26}$$

for the transduced cells, and

$$\frac{\beta(p^n)}{\beta(EC_50) + \beta(p^n)}\left(1 - \frac{c^n + r^n}{K}\right) \tag{7.27}$$

for the recruited cells. Recall from equations (7.4) and (7.5) that these, multiplied by the maximum diffusion rate paramters D_c and D_r give us the actual diffusion rates. This is easily associated with our grid, which also has the white vs. gray information and associated scaling of the diffusion rates. This is passed to code that does the flux computation (see Appendix B which lists the online repository where these codes may be found). The conjugate

gradient iterates through the the flux differencing as it narrows in on the ΔU (we do this in practice with a call to the `pcg.m` function in MATLAB). Once this is found we do the update $U^* = U^n + \Delta U$ and proceed to the reaction terms.

7.5.3 Reaction Terms

If we look at the reaction portion of our equations (i.e., without the diffusion terms), we have a system of the form

$$u_t = \mathcal{R}(u). \tag{7.28}$$

where the reaction operator $\mathcal{R}(u)$ is given by the right hand side of equations (7.1)–(7.3). We can scale our quantities in the first two equations by the carrying capacity of tumor cells K, to give the reaction operator as

$$\mathcal{R}(u) = \begin{bmatrix} \rho_c \frac{\beta(p+p_{auto})}{\beta(EC_{50})+\beta(p+p_{auto})} c\,(1-(c+r)) \\ \rho_r \frac{\beta(p)}{\beta(EC_{50})+\beta(p)} r\,(1-(c+r)) \\ \eta_c c - q_r \beta(p) r - q_c \beta(p+p_{auto})\,(1-\beta(p_{auto}))\,c \end{bmatrix} \tag{7.29}$$

where the β functional response terms are as follows:

$$\beta(p) = \frac{p}{k_m + p},\ \beta(p_{auto}) = \frac{p_{auto}}{k_m + p_{auto}},\ \beta(p{+}p_{auto}) = \frac{p + p_{auto}}{k_m + p + p_{auto}},\ \beta(EC_{50}) = \frac{EC_{50}}{k_m + EC_{50}}.$$

To solve this nonlinear system of ODEs (7.29), which describes the proliferation of cells (c and r) in the presence of PDGF and the production and consumption of PDGF (p) by those cells, we use the TR-BDF2 method. The TR-BDF2 method is given by

$$U^{n+1/2} = U^n + \frac{\Delta t}{4}\left(\mathcal{R}(U^n) + \mathcal{R}(U^{n+1/2})\right) \tag{7.30a}$$

$$U^{n+1} = \frac{1}{3}\left(4U^{n+1/2} - U^n + \Delta t \mathcal{R}(U^{n+1})\right) \tag{7.30b}$$

Since this is an implicit method, it requires the use of a nonlinear solve at each stage. Newton's method was used to solve the vector equation

$$G(\theta^k) = 0 \tag{7.31}$$

where θ^k is the solution at time $t = k$ and the nonlinear function G maps the state variables onto themselves, $G : \mathbb{R}^3 \to \mathbb{R}^3$. The solution at time $t = k + 1$ is approximated by

$$\theta^{k+1} = \theta^k + \delta^k \tag{7.32}$$

where δ^k solves the system of equations

$$J(\theta^k)\delta^k = -G(\theta^k) \tag{7.33}$$

where $J(\theta)$ is the Jacobian matrix,

$$J_{i,j}(\theta) = \frac{\partial}{\partial \theta_i} G_j(\theta). \tag{7.34}$$

This process is iterated until the error falls below a desired tolerance, $\|\delta^k\|_\infty < tol$.
We compute the Jacobian in pieces and pre-compute the derivatives of the functional response $\beta(p)$.

If we define

$$R(p) = \frac{\beta(p)}{\beta(EC_{50}) + \beta(p)}, \text{ where again } \beta(p) = \frac{p}{k_m + p}, \tag{7.35}$$

then we can expresss

$$\frac{d}{dp}(\beta(p)) = \frac{k_m}{(k_m + p)^2}, \quad \frac{d}{dp}(R(p)) = \frac{\beta(EC_{50})k_m}{(k_m + p)^2(\beta(EC_{50}) + \beta(p))^2}. \tag{7.36}$$

For the sake of clarity and thoroughness, we will also compute the partial derivatives of the logistic growth portion of the reaction terms.
First, define

$$CAP_c \equiv c\left(1 - \frac{c + r}{K}\right), \quad CAP_r \equiv r\left(1 - \frac{c + r}{K}\right) \tag{7.37}$$

to be the logistic portions of the reaction terms in (7.1) and (7.2), respectively.
Then we have

$$\frac{\partial}{\partial c}(CAP_c) = 1 - \frac{2c + r}{K}, \quad \text{and} \quad \frac{\partial}{\partial r}(CAP_c) = \frac{-c}{K} \tag{7.38}$$

and similarly,

$$\frac{\partial}{\partial r}(CAP_r) = 1 - \frac{2r+c}{K}, \quad \text{and} \quad \frac{\partial}{\partial c}(CAP_r) = \frac{-r}{K}. \tag{7.39}$$

Using these derivatives we can compute the 3×3 Jacobian, J, of the Reaction operator (7.29) and get:

$$J = \begin{bmatrix} \rho_c R(p+p_{auto})(1-\frac{2c+r}{K}) & -\rho_c R(p+p_{auto})\frac{c}{K} & \rho_c c(1-\frac{c+r}{K})\frac{d}{dp}(R(p+p_{auto})) \\ -\rho_r R(p)\frac{r}{K} & \rho_r R(p)(1-\frac{2r+c}{K}) & \rho_r r(1-\frac{c+r}{K})\frac{d}{dp}(R(p)) \\ \eta_c - q_c\beta(p)\alpha & -q_r\beta(p) & -q_c c\alpha\frac{d}{dp}(\beta(p)) - q_r r\frac{d}{dp}(\beta(p)) \end{bmatrix} \tag{7.40}$$

The function to be solved, $F(\theta) = 0$ from the first stage of the TR-BDF2 method is given by

$$F(\theta^n, \theta^{n+1/2}) = \left(\theta^n + \frac{\Delta t}{4}\mathcal{R}(\theta^n)\right) + \left(\frac{\Delta t}{4}\mathcal{R}(\theta^{n+1/2}) - \theta^{n+1/2}\right) \tag{7.41}$$

has Jacobian (J_F) given by

$$J_F = \frac{\Delta t}{4}J(\mathcal{R}(\theta^{n+1/2})) - I \tag{7.42}$$

where J is the Jacobian of the Reaction operator. Similarly for the second stage,

$$G(\theta^n, \theta^{n+1/2}, \theta^{n+1}) = \left(\frac{4}{3}\theta^{n+1/2} - \frac{1}{3}\theta^n\right) + \left(\frac{\Delta t}{3}\mathcal{R}(\theta^{n+1}) - \theta^{n+1}\right) \tag{7.43}$$

that has Jacobian (J_G) given by

$$J_G = \frac{\Delta t}{3}J(\mathcal{R}(\theta^{n+1})) - I. \tag{7.44}$$

Again, these were solved using Newton's method and used to update the solution at the current time step, $n+1$, and then advance to the next time step, repeating the solution of the diffusion and reaction components, until we reach t_{final} for the simulation.

Further detail about how this was implemented in code form can be found in Appendix B.

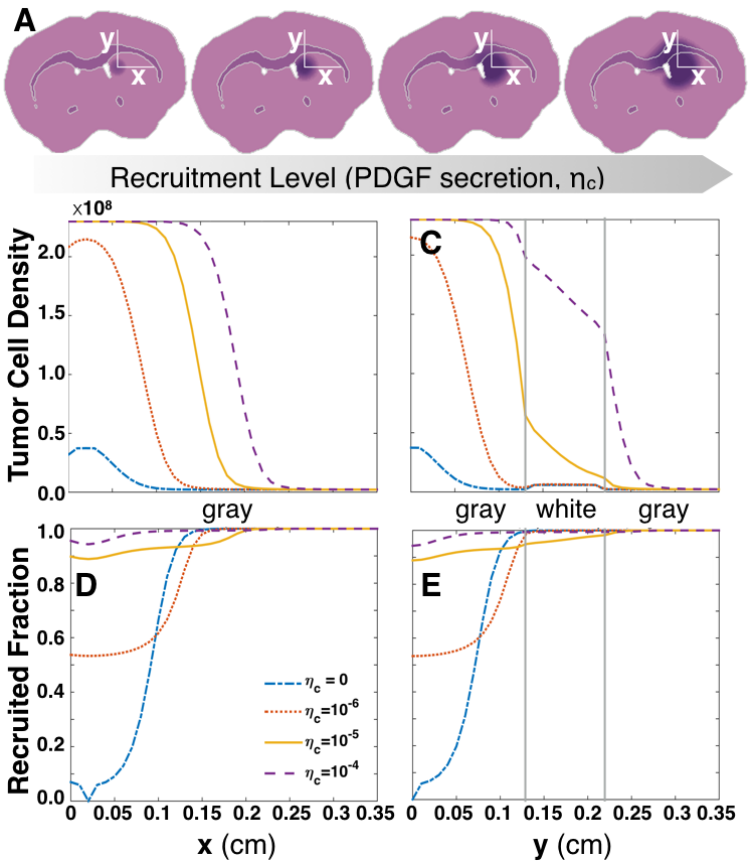

Figure 7.4: **Tumors of varying degrees of recruitment simulated for same length of time (30 days). A.** Simulated tumors at 30 days of growth, with different values for parameter η_c to simulate varied recruitment (from left to right: $\eta_c = 0, 10^{-6}, 10^{-5}$, and 10^{-4}, respectively). Lines labeled x and y show the locations of samples used in the plots for panels B–E, corresponding to the x and y labels below the columns. These start at the center where the simulation was initialized, then x extends out in only gray matter, while y extends through the corpus callosum (white matter), as indicated by the vertical lines in C and E. **B.** Cell densities vs. space, sampled in an exclusively gray matter region. **C.** Cell densities vs. space, sampled in a region that passes through white matter (vertical lines). **D.** Fraction of tumor that is made up of recruited progenitor cells vs. space. **E.** Fraction of tumor that is made up of recruited cells vs. space, passing through white matter (vertical lines).

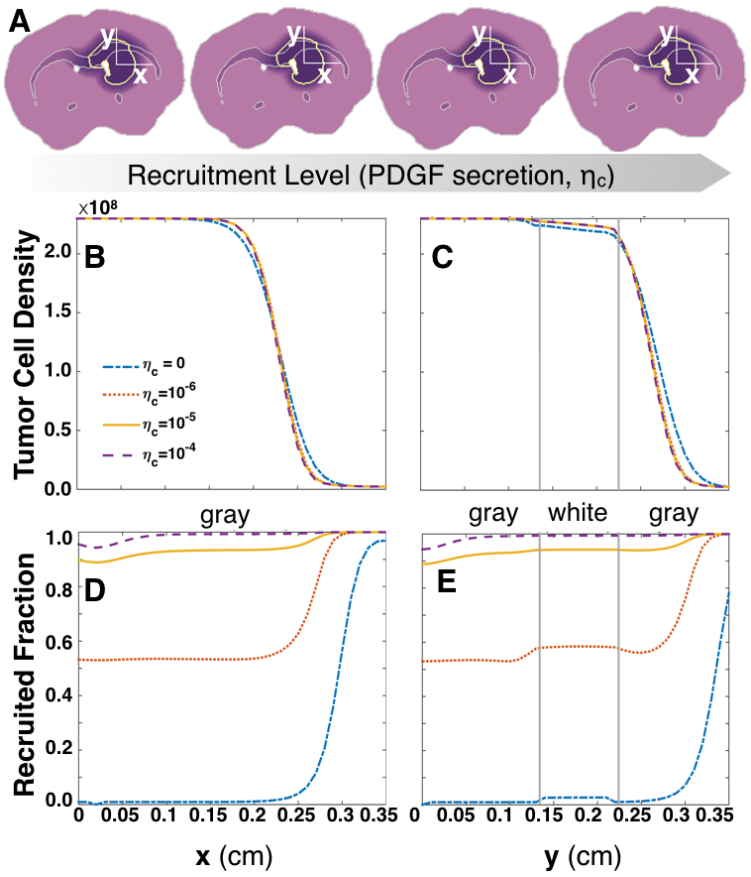

Figure 7.5: **Tumors of varying degrees of recruitment simulated until same size on T1 MRI (0.2 cm).** Simulated tumors with an averaged radius of 0.2 cm at the density threshold detectable by T1 MRI, having different values of η_c to indicate varying degrees of recruitment (from left to right: $\eta_c = 0, 10^{-6}, 10^{-5}$, and 10^{-4}, respectively). The MRI visible region is outlined in yellow. Lines labeled x and y show the locations of samples used in the plots for panels B–E, corresponding to the x and y labels below the columns. These start at the center where the simulation was initialized and then x extends out in only gray matter, while y extends through the corpus callosum (white matter), as indicated by the vertical lines in C and E. **B.** Cell densities vs. space, sampled in gray matter region. **C.** Cell densities vs. space, sampled through white matter (vertical lines). **D.** Fraction of tumor that is made up of recruited progenitor cells vs. space, staying in only gray matter. **E.** Fraction of tumor that is made up of recruited progenitor cells vs. space, passing through white matter (vertical lines).

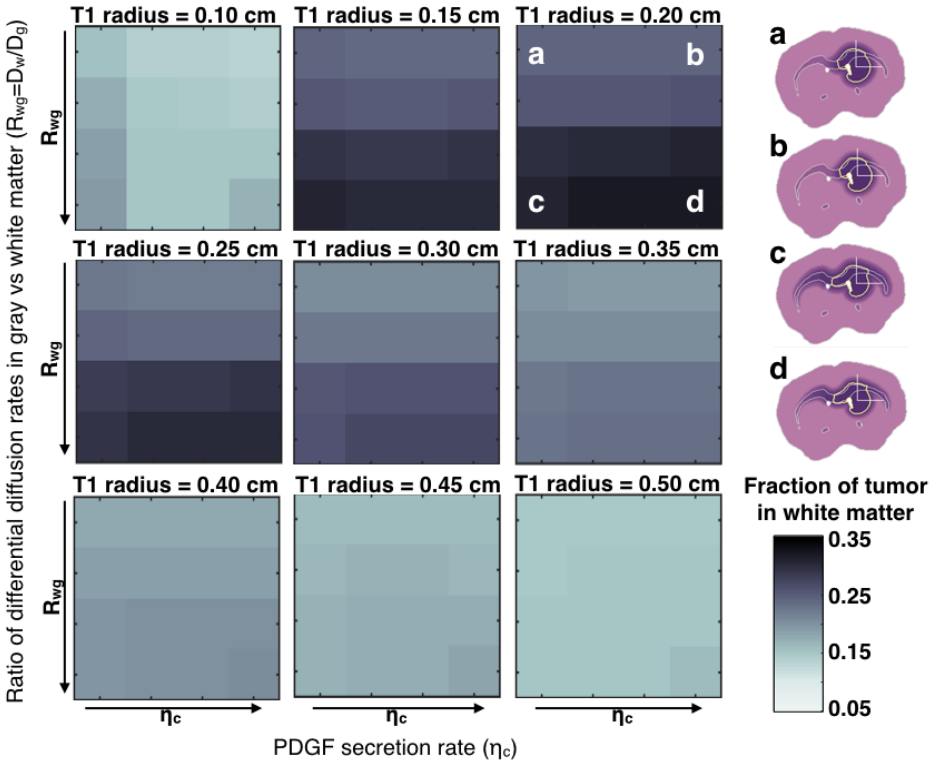

Figure 7.6: **Fraction of tumor cells in white matter regions at indicated T1 detectable sizes for varied ratios, R_{wg}, of differential cellular diffusion rates and varied PDGF secretion rates, η_c.** Each subplot relates to a different size of tumor as detected on T1 MRI. Arrows show direction of increasing parameter values. Going down the columns of each subplot, R_{wg} = 5, 10, 50, and 100, and from left to right along the rows $\eta_c = 0$, 10^{-6}, 10^{-5}, and 10^{-4}. The four tumor simulations shown correspond with the combinations of the high and low extreme values of these two parameters and have 0.2 cm average radius at the T1 MRI detectable threshold. The color map indicates the fraction of tumor that is in white matter structures as opposed to gray matter.

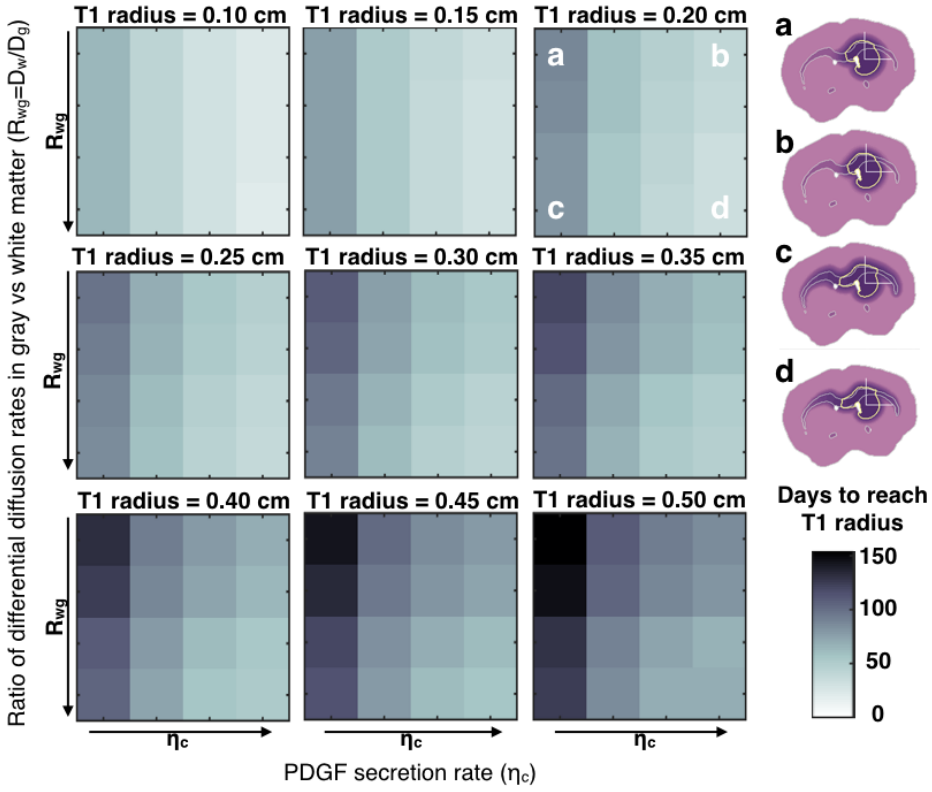

Figure 7.7: **Growth time required to reach indicated T1 detectable sizes for varied ratios, R_{wg}, of differential cellular diffusion rates and varied PDGF secretion rates, η_c.** Each subplot relates to a different size of tumor as detected on T1 MRI. Arrows show direction of increasing parameter values. Going down the columns of each subplot, $R_{wg} = 5$, 10, 50, and 100, and from left to right along the rows $\eta_c = 0$, 10^{-6}, 10^{-5}, and 10^{-4}. The four tumor simulations shown correspond with the combinations of the high and low extreme values of these two parameters and have 0.2 cm average radius at the T1 MRI detectable threshold. The color map indicates the time (in days) required to reach the indicated size as detectable on T1 MRI.

Chapter 8

CONCLUSIONS AND FUTURE WORK

In this dissertation, I have examined the role of platelet-derived growth factor (PDGF) in tumor initiation and progression. First, in chapters 2 and 3, I explored the role of PDGF in wound healing and inflammation, showing in chapter 3 that dysregulated wound healing could lead to tissue pathology, potentially even cancer. Then, in chapter 4, I developed a 1D spherically symmetric model of PDGF–driven tumor growth to investigate the importance of oligodendroglial progenitor cell (OPC) recruitment through paracrine PDGF signaling, as observed in an experimental animal model of glioma. I discussed the parameterization of this model, including the use of vast amounts of experimental data, in chapter 5, as well as a sensitivity analysis of the model in chapter 6. Finally, in chapter 7, I modified this tumor model for 2D to implement on a rodent brain atlas, which also allowed for differential rates of diffusion in gray versus white matter regions of the brain. Overall we have observed the following key results:

1. Sustained PDGF secretion following some tissue insult (with ensuing inflammation) can lead to chronic lesions, similar to chronic gliosis, and potentially large lesions reminiscent of neoplasia.

2. The Proliferation–Invasion–Recruitment (PIR model) accurately reflects the distribution of cells in the PDGF–driven experimental tumors of [9].

3. Higher levels of paracrine PDGF signaling in PIR simulated PDGF–driven tumors result in more aggressive tumor growth.

4. Growth rates of PDGF–driven tumors and PIR model simulated tumors are within the

range of those observed in untreated human gliomas, generally falling into the lower end of that range.

5. The PIR model is most sensitive to the parameter specifying the diffusion rate of tumor cells (transduced and untransduced OPCs). This highlights the importance of our being able to rely on data for determining this parameter.

6. The speed of PDGF–driven glioma growth is influenced more by PDGF signaling than by the ratio of gray to white diffusion rates.

7. The shape of PDGF–driven glioma growth is influenced more by the ratio of gray to white diffusion rates than by PDGF signaling.

Going forward, the PIR model of PDGF–driven glioma growth (which is very similar to proneural glioma) could be useful for investigating response to PDGF–inhibiting therapies. Implementing the model on a human brain atlas in 2D or even 3D would allow such therapy to be modeled in the context of tumor resection (surgical removal of tumor tissue). Given the success this model has had in predicting the distribution of cells in the animal models, we expect that this model could also be successful in understanding the growth and treatment of human proneural tumors. Further, I would be interested in seeing more work on the role inflammatory cytokines in stimulating the sustained release of PDGF. This could help us find alternative ways to suppress tumor growth and lead to approaches for reducing the small but nonzero risk of traumatic brain injuries leading to pathological conditions or even giving eventual rise to cancers.

BIBLIOGRAPHY

[1] C. Allamargot, A. Pouplard-Barthelaix, and C. Fressinaud. A single intracerebral microinjection of platelet-derived growth factor (pdgf) accelerates the rate of remyelination in vivo. *Brain research*, 918(1):28–39, 2001.

[2] E. C. Alvord Jr. Patterns of growth of gliomas. *Am J Neuroradiol*, 16(5):1013–7, 1995.

[3] M. Amano, C. Leblond, and N. Nadler. Radioautographic analysis of nuclear rna in mouse cells revealing three pools with different turnover times. *Experimental cell research*, 38(2):314–340, 1965.

[4] J. Andrae, R. Gallini, and C. Betsholtz. Role of platelet-derived growth factors in physiology and medicine. *Genes & development*, 22(10):1276–1312, 2008.

[5] J. Andrew, J. Hoyland, A. Freemont, and D. Marsh. Platelet-derived growth factor expression in normally healing human fractures. *Bone*, 16(4):455 – 460, 1995.

[6] J. F. Apperley, M. Gardembas, J. V. Melo, R. Russell-Jones, B. J. Bain, E. J. Baxter, A. Chase, J. M. Chessells, M. Colombat, C. E. Dearden, S. Dimitrijevic, F.-X. Mahon, D. Marin, Z. Nikolova, E. Olavarria, S. Silberman, B. Schultheis, N. C. Cross, and J. M. Goldman. Response to imatinib mesylate in patients with chronic myeloproliferative diseases with rearrangements of the platelet-derived growth factor receptor beta. *New England Journal of Medicine*, 347(7):481–487, 2002. PMID: 12181402.

[7] R. C. Armstrong, L. Harvath, and M. E. Dubois-Dalcq. Type 1 astrocytes and oligodendrocyte-type 2 astrocyte glial progenitors migrate toward distinct molecules. *Journal of Neuroscience Research*, 27(3):400–407, 1990.

[8] A. Armulik, G. Genové, M. Mäe, M. H. Nisancioglu, E. Wallgard, C. Niaudet, L. He, J. Norlin, P. Lindblom, K. Strittmatter, et al. Pericytes regulate the blood-brain barrier. *Nature*, 468(7323):557–561, 2010.

[9] M. Assanah, R. Lochhead, A. Ogden, J. Bruce, J. Goldman, and P. Canoll. Glial progenitors in adult white matter are driven to form malignant gliomas by platelet-derived growth factor-expressing retroviruses. *J Neurosci*, 26(25):6781–90, 2006.

[10] M. C. Assanah, J. N. Bruce, S. O. Suzuki, A. Chen, J. E. Goldman, and P. Canoll. Pdgf stimulates the massive expansion of glial progenitors in the neonatal forebrain. *Glia*, 57(16):1835–1847, 2009.

[11] K. A. Bates, E. S. Drummond, G. S. Cozens, and A. R. Harvey. Vascular insufficiency, not inflammation, contributes to chronic gliosis in a rat cns transplantation model. *Restorative neurology and neuroscience*, 34(2):313–323, 2016.

[12] C. Beadle, M. C. Assanah, P. Monzo, R. Vallee, S. S. Rosenfeld, and P. Canoll. The role of myosin ii in glioma invasion of the brain. *Mol Biol Cell*, 19(8):3357–68, 2008.

[13] B. Berk, R. Alexander, T. Brock, M. Gimbrone, and R. Webb. Vasoconstriction: a new activity for platelet-derived growth factor. *Science*, 232(4746):87–90, 1986.

[14] C. Betsholtz. Biology of platelet-derived growth factors in development. *Birth Defects Research Part C: Embryo Today: Reviews*, 69(4):272–285, 2003.

[15] L. Bissell, S. Tibrewal, V. Sahni, and W. S Khan. Growth factors and platelet rich plasma in anterior cruciate ligament reconstruction. *Current stem cell research & therapy*, 10(1):19–25, 2015.

[16] S. M. Blinkov and I. I. Glezer. *The human brain in figures and tables: a quantitative handbook*. Basic Books, 1968.

[17] S. M. Blower and H. Dowlatabadi. Sensitivity and uncertainty analysis of complex models of disease transmission: an hiv model, as an example. *International Statistical Review/Revue Internationale de Statistique*, pages 229–243, 1994.

[18] P. Boor, T. Ostendorf, and J. Floege. Pdgf and the progression of renal disease. *Nephrology Dialysis Transplantation*, 29(suppl 1):i45–i54, 2014.

[19] P. Boucher and M. Gotthardt. Lrp and pdgf signaling: a pathway to atherosclerosis. *Trends in cardiovascular medicine*, 14(2):55–60, 2004.

[20] A. Cairnie, L. Lamerton, and G. Steel. Cell proliferation studies in the intestinal epithelium of the rat: I. determination of the kinetic parameters. *Experimental cell research*, 39(2):528–538, 1965.

[21] A. Cairnie, L. Lamerton, and G. Steel. Cell proliferation studies in the intestinal epithelium of the rat: Ii. theoretical aspects. *Experimental cell research*, 39(2):539–553, 1965.

[22] J. S. Campbell, S. D. Hughes, D. G. Gilbertson, T. E. Palmer, M. S. Holdren, A. C. Haran, M. M. Odell, R. L. Bauer, H.-P. Ren, H. S. Haugen, M. M. Yeh, and N. Fausto. Platelet-derived growth factor c induces liver fibrosis, steatosis, and hepatocellular carcinoma. *Proceedings of the National Academy of Sciences of the United States of America*, 102(9):3389–3394, 2005.

[23] N. A. Charles, E. C. Holland, R. Gilbertson, R. Glass, and H. Kettenmann. The brain tumor microenvironment. *Glia*, 59(8):1169–1180, 2011.

[24] M. R. Chicoine and D. L. Silbergeld. Assessment of brain tumor cell motility in vivo and in vitro. *Journal of Neurosurgery*, 82(4):615–622, 1995. PMID: 7897524.

[25] V. Chintalgattu, D. Ai, R. R. Langley, J. Zhang, J. A. Bankson, T. L. Shih, A. K. Reddy, K. R. Coombes, I. N. Daher, S. Pati, S. S. Patel, J. S. Pocius, G. E. Taffet, L. M. Buja, M. L. Entman, and A. Y. Khakoo. Cardiomyocyte pdgfr- signaling is an essential component of the mouse cardiac response to load-induced stress. *The Journal of Clinical Investigation*, 120(2):472–484, 2 2010.

[26] G. C. Cruywagen, D. E. Woodward, P. Tracqui, G. T. Bartoo, J. Murray, and E. C. Alvord. The modelling of diffusive tumours. *Journal of Biological Systems*, 3(04):937–945, 1995.

[27] C. Dai, J. C. Celestino, Y. Okada, D. N. Louis, G. N. Fuller, and E. C. Holland. Pdgf autocrine stimulation dedifferentiates cultured astrocytes and induces oligodendrogliomas and oligoastrocytomas from neural progenitors and astrocytes in vivo. *Genes Dev*, 15(15):1913–25, 2001.

[28] O. De Wever, P. Demetter, M. Mareel, and M. Bracke. Stromal myofibroblasts are drivers of invasive cancer growth. *International journal of cancer*, 123(10):2229–2238, 2008.

[29] J.-B. Demoulin and A. Essaghir. Pdgf receptor signaling networks in normal and cancer cells. *Cytokine & growth factor reviews*, 25(3):273–283, 2014.

[30] R. B. Dickinson and R. T. Tranquillo. Optimal estimation of cell movement indices from the statistical analysis of cell tracking data. *AIChE Journal*, 39(12):1995–2010, 1993.

[31] J. M. Edelberg, W. C. Aird, W. Wu, H. Rayburn, W. S. Mamuya, M. Mercola, and R. D. Rosenberg. Pdgf mediates cardiac microvascular communication. *Journal of Clinical Investigation*, 102(4):837, 1998.

[32] M. Enesco and C. Leblond. Increase in cell number as a factor in the growth of the organs and tissues of the young male rat. *Development*, 10(4):530–562, 1962.

[33] T. Eschenhagen, T. Force, M. S. Ewer, G. W. de Keulenaer, T. M. Suter, S. D. Anker, M. Avkiran, E. de Azambuja, J.-L. Balligand, D. L. Brutsaert, G. Condorelli, A. Hansen, S. Heymans, J. A. Hill, E. Hirsch, D. Hilfiker-Kleiner, S. Janssens, S. de Jong, G. Neubauer, B. Pieske, P. Ponikowski, M. Pirmohamed, M. Rauchhaus, D. Sawyer, P. H. Sugden, J. Wojta, F. Zannad, and A. M. Shah. Cardiovascular side effects of cancer therapies: a position statement from the heart failure association of the european society of cardiology. *European Journal of Heart Failure*, 13(1):1–10, 2011.

[34] E. I. Fomchenko, J. D. Dougherty, K. Y. Helmy, A. M. Katz, A. Pietras, C. Brennan, J. T. Huse, A. Milosevic, and E. C. Holland. Recruited cells can become transformed and overtake pdgf-induced murine gliomas *In Vivo* during tumor progression. *PLoS ONE*, 6(7):e20605, 07 2011.

[35] E. I. Fomchenko and E. C. Holland. Platelet-derived growth factor-mediated gliomagenesis and brain tumor recruitment. *Neurosurg Clin N Am*, 18(1):39–58, viii, 2007.

[36] E. E. Frost, Z. Zhou, K. Krasnesky, and R. C. Armstrong. Initiation of oligodendrocyte progenitor cell migration by a pdgf-a activated extracellular regulated kinase (erk) signaling pathway. *Neurochem Res*, 34(1):169–181, 2009.

[37] R. Fry, S. Lesher, W. Kisieleski, and G. Sacher. Cell proliferation in the small intestine. *Cell proliferation*, pages 213–233, 1963.

[38] H. Gerhardt and C. Betsholtz. Endothelial-pericyte interactions in angiogenesis. *Cell and tissue research*, 314(1):15–23, 2003.

[39] D. Hampton, K. Rhodes, C. Zhao, R. Franklin, and J. Fawcett. The responses of oligodendrocyte precursor cells, astrocytes and microglia to a cortical stab injury, in the brain. *Neuroscience*, 127(4):813–820, 2004.

[40] D. Hanahan and L. M. Coussens. Accessories to the crime: functions of cells recruited to the tumor microenvironment. *Cancer cell*, 21(3):309–322, 2012.

[41] H. L. Harpold, J. Alvord, E. C., and K. R. Swanson. The evolution of mathematical modeling of glioma proliferation and invasion. *J Neuropathol Exp Neurol*, 66(1):1–9, 2007.

[42] B. J. Hayes, K. J. Riehle, M. Shimizu-Albergine, R. L. Bauer, K. L. Hudkins, F. Johansson, M. M. Yeh, W. M. Mahoney Jr, R. S. Yeung, and J. S. Campbell. Activation of platelet-derived growth factor receptor alpha contributes to liver fibrosis. *PloS one*, 9(3):e92925, 2014.

[43] C.-H. Heldin and B. Westermark. Mechanism of action and in vivo role of platelet-derived growth factor. *Physiological Reviews*, 79(4):1283–1316, 1999.

[44] M. Hermanson, K. Funa, M. Hartman, L. Claesson-Welsh, C.-H. Heldin, B. Westermark, and M. Nistr. Platelet-derived growth factor and its receptors in human glioma tissue: Expression of messenger rna and protein suggests the presence of autocrine and paracrine loops. *Cancer Research*, 52(11):3213–3219, 1992.

[45] R. V. Hoch and P. Soriano. Roles of pdgf in animal development. *Development*, 130(20):4769–4784, 2003.

[46] D. B. Hoelzinger, T. Demuth, and M. E. Berens. Autocrine factors that sustain glioma invasion and paracrine biology in the brain microenvironment. *Journal of the National Cancer Institute*, 99(21):1583–1593, 2007.

[47] R. L. Iman and J. C. Helton. An investigation of uncertainty and sensitivity analysis techniques for computer models. *Risk analysis*, 8(1):71–90, 1988.

[48] J. L. Ingram, A. B. Rice, K. Geisenhoffer, D. K. Madtes, and J. C. Bonner. Il-13 and il-1β promote lung fibroblast growth through coordinated up-regulation of pdgf-aa and pdgf-rα. *The FASEB journal*, 18(10):1132–1134, 2004.

[49] S. Ivkovic, C. Beadle, S. Noticewala, S. C. Massey, K. R. Swanson, L. N. Toro, A. R. Bresnick, P. Canoll, and S. S. Rosenfeld. Direct inhibition of myosin II effectively blocks glioma invasion in the presence of multiple motogens. *Molecular Biology of the Cell*, 23(4):533–542, jan 2012.

[50] R. L. Jensen. Growth factor-mediated angiogenesis in the malignant progression of glial tumors: A review. *Surgical neurology*, 49(2):189–195, 1998.

[51] M. Kendall and A. Stuart. The advanced theory of statistics vol. ii, 1979.

[52] N. Kohler and A. Lipton. Platelets as a source of fibroblast growth-promoting activity. *Experimental cell research*, 87(2):297–301, 1974.

[53] L. Lajtha, R. Oliver, and F. Ellis. Incorporation of 32p and adenine 14c into dna by human bone marrow cells in vitro. *British journal of cancer*, 8(2):367, 1954.

[54] C. Leblond and B. E. Walker. Renewal of cell populations. *Physiological Reviews*, 36(2):255–276, 1956.

[55] L. Lei, A. M. Sonabend, P. Guarnieri, C. Soderquist, T. Ludwig, S. Rosenfeld, J. N. Bruce, and P. Canoll. Glioblastoma models reveal the connection between adult glial progenitors and the proneural phenotype. *PLoS ONE*, 6(5):e20041, 05 2011.

[56] A. K. Letson and L. E. Dahners. The effect of combinations of growth factors on ligament healing. *Clinical orthopaedics and related research*, 308:207–212, 1994.

[57] J. M. Levine, R. Reynolds, and J. W. Fawcett. The oligodendrocyte precursor cell in health and disease. *Trends in Neurosciences*, 24(1):39 – 47, 2001.

[58] H. Li, X. Fan, and J. Houghton. Tumor microenvironment: the role of the tumor stroma in cancer. *Journal of cellular biochemistry*, 101(4):805–815, 2007.

[59] G. Lindmark, C. Sundberg, B. Glimelius, L. Påhlman, K. Rubin, and B. Gerdin. Stromal expression of platelet-derived growth factor beta-receptor and platelet-derived growth factor b-chain in colorectal cancer. *Laboratory investigation; a journal of technical methods and pathology*, 69(6):682–689, 1993.

[60] K. Lopez, M. Assanah, A. Waziri, D. Fusco, A. Tannenbaum, K. Linskey, G. M. McKhann, M. B. Sisti, J. Bruce, and P. Canoll. Human glioma cells recruit and expand adult glial progenitors via paracrine platelet-derived growth factor signaling. *Neurosurgery*, 62(6):1424–1425, 2008.

[61] D. N. Louis, H. Ohgaki, O. D. Wiestler, W. K. Cavenee, P. C. Burger, A. Jouvet, B. W. Scheithauer, and P. Kleihues. The 2007 who classification of tumours of the central nervous system. *Acta Neuropathol*, 114(2):97–109, 2007.

[62] Y. Ma, P. Hof, S. Grant, S. Blackband, R. Bennett, L. Slatest, M. McGuigan, and H. Benveniste. A three-dimensional digital atlas database of the adult c57bl/6j mouse brain by magnetic resonance microscopy. *Neuroscience*, 135(4):1203 – 1215, 2005.

[63] Y. Ma, D. Smith, P. R. Hof, B. Foerster, S. Hamilton, S. J. Blackband, M. Yu, and H. Benveniste. In vivo 3d digital atlas database of the adult c57bl/6j mouse brain by magnetic resonance microscopy. *Frontiers in Neuroanatomy*, 2(1), 2008.

[64] M. W. Majesky, M. A. Reidy, D. F. Bowen-Pope, C. E. Hart, J. N. Wilcox, and S. M. Schwartz. Pdgf ligand and receptor gene expression during repair of arterial injury. *The Journal of Cell Biology*, 111(5):2149–2158, 1990.

[65] K. Majumdar, B. D. Radotra, R. K. Vasishta, and A. Pathak. Platelet-derived growth factor expression correlates with tumor grade and proliferative activity in human oligodendrogliomas. *Surgical neurology*, 72(1):54–60, 2009.

[66] E. Masliah, M. Mallory, M. Alford, R. Deteresa, and T. Saitoh. Pdgf is associated with neuronal and glial alterations of alzheimer's disease. *Neurobiology of aging*, 16(4):549–556, 1995.

[67] S. C. Massey, M. C. Assanah, K. A. Lopez, P. Canoll, and K. R. Swanson. Glial progenitor cell recruitment drives aggressive glioma growth: mathematical and experimental modelling. *Journal of The Royal Society Interface*, 9(73):1757–1766, 2012.

[68] S. C. Massey, R. C. Rockne, A. Hawkins-Daarud, J. Gallaher, A. R. A. Anderson, P. Canoll, and K. Swanson. Simulating pdgf–driven glioma growth and invasion in an anatomically–accurate brain domain. Submitted.

[69] M. D. McKay, R. J. Beckman, and W. J. Conover. Comparison of three methods for selecting values of input variables in the analysis of output from a computer code. *Technometrics*, 21(2):239–245, 1979.

[70] M. Mendelsohn. Autoradiographic measurement of tumor growth. *Acta-Unio Internationalis Contra Cancrum*, 20:1400–1, 1964.

[71] M. L. Mendelsohn. Autoradiographic analysis of cell proliferation in spontaneous breast cancer of c3h mouse. ii. growth and survival of cells labeled with tritiated thymidine. *Journal of the National Cancer Institute*, 25:485–500, Sept 1960.

[72] M. L. Mendelsohn. Autoradiographic analysis of cell proliferation in spontaneous breast cancer of c3h mouse. iii. the growth fraction. *Journal of the National Cancer Institute*, 28(5):1015–1029, May 1962.

[73] M. L. Mendelsohn, F. C. Dohan, and H. A. Moore. Autoradiographic analysis of cell proliferation in spontaneous breast cancer of c3h mouse. i. typical cell cycle and timing of dna synthesis. *Journal of the National Cancer Institute*, 25:477–84, Sept 1960.

[74] B. Messier and C. Leblond. Cell proliferation and migration as revealed by radioautography after injection of thymidine-h3 into male rats and mice. *American Journal of Anatomy*, 106(3):247–285, 1960.

[75] J. Murray. *Mathematical Biology*, volume I: An Introduction. Springer-Verlag, New York, 3rd edition, 2002.

[76] J. D. Murray. *Lectures on Nonlinear-Differential-Equation Models in Biology*. Clarendon Press, Oxford, 1977.

[77] Y. Nakamura, F. Tanaka, Y. Yoshikawa, K. Mimori, H. Inoue, K. Yanaga, and M. Mori. Pdgf-bb is a novel prognostic factor in colorectal cancer. *Annals of surgical oncology*, 15(8):2129–2136, 2008.

[78] A. D. Norden, G. S. Young, K. Setayesh, A. Muzikansky, R. Klufas, G. L. Ross, A. S. Ciampa, L. G. Ebbeling, B. Levy, J. Drappatz, S. Kesari, and P. Y. Wen. Bevacizumab for recurrent malignant gliomas: Efficacy, toxicity, and patterns of recurrence. *Neurology*, 70(10):779–787, 2008.

[79] M. C. Nunes, N. S. Roy, H. M. Keyoung, R. R. Goodman, G. McKhann, L. Jiang, J. Kang, M. Nedergaard, and S. A. Goldman. Identification and isolation of multipotential neural progenitor cells from the subcortical white matter of the adult human brain. *Nature Medicine*, 9(4):439 – 447, 2003.

[80] J. Pallud, E. Mandonnet, H. Duffau, M. Kujas, R. Guillevin, D. Galanaud, L. Taillandier, and L. Capelle. Prognostic value of initial magnetic resonance imaging growth rates for world health organization grade ii gliomas. *Annals of Neurology*, 60(3):380–383, 2006.

[81] N. Pringle, E. J. Collarini, M. J. Mosley, C.-H. Heldin, B. Westermark, and W. D. Richardson. Pdgf a chain homodimers drive proliferation of bipotential (o-2a) glial progenitor cells in the developing rat optic nerve. *The EMBO journal*, 8(4):1049, 1989.

[82] J. M. Redwine and R. C. Armstrong. In vivo proliferation of oligodendrocyte progenitors expressing pdgfar during early remyelination. *Journal of neurobiology*, 37(3):413–428, 1998.

[83] W. Rhee, S. Ray, H. Yokoo, M. E. Hoane, C. C. Lee, A. M. Mikheev, P. J. Horner, and R. C. Rostomily. Quantitative analysis of mitotic olig2 cells in adult human brain and gliomas: Implications for glioma histogenesis and biology. *Glia*, 57(5):510–523, 2009.

[84] K. Rhodes, G. Raivich, and J. Fawcett. The injury response of oligodendrocyte precursor cells is induced by platelets, macrophages and inflammation-associated cytokines. *Neuroscience*, 140(1):87–100, 2006.

[85] R. Ross, J. Glomset, B. Kariya, and L. Harker. A platelet-dependent serum factor that stimulates the proliferation of arterial smooth muscle cells in vitro. *Proceedings of the National Academy of Sciences*, 71(4):1207–1210, 1974.

[86] R. Ross, E. W. Raines, and D. F. Bowen-Pope. The biology of platelet-derived growth factor. *Cell*, 46(2):155–169, 1986.

[87] N. S. Roy, S. Wang, C. Harrison-Restelli, A. Benraiss, R. A. R. Fraser, M. Gravel, P. E. Braun, and S. A. Goldman. Identification, isolation, and promoter-defined separation of mitotic oligodendrocyte progenitor cells from the adult human subcortical white matter. *The Journal of Neuroscience*, 19(22):9986–9995, 1999.

[88] N. Scolding, R. Franklin, S. Stevens, C.-H. Heldin, A. Compston, and J. Newcombe. Oligodendrocyte progenitors are present in the normal adult human cns and the lesions of multiple sclerosis. *Brain*, 121(12):2221–2228, December 1998.

[89] N. Shigesada and K. Kawasaki. *Biological invasions: theory and practice*. Oxford University Press, 1997.

[90] A. H. Shih, C. Dai, X. Hu, M. K. Rosenblum, J. A. Koutcher, and E. C. Holland. Dose-dependent effects of platelet-derived growth factor-b on glial tumorigenesis. *Cancer Res*, 64(14):4783–9, 2004.

[91] G. G. Steel. *Growth Kinetics of Tumors: Cell Population Kinetics in Relation to the Growth and Treatment of Cancer*. Clarendon Press, Oxford, 1977.

[92] C. L. Stokes, D. A. Lauffenburger, and S. K. Williams. Migration of individual microvessel endothelial cells: stochastic model and parameter measurement. *Journal of Cell Science*, 99(2):419–430, 1991.

[93] M. Swann. The control of cell division: A review i. general mechanisms. *Cancer Research*, 17(8):727–757, 1957.

[94] M. Swann and J. Mitchison. The mechanism of cleavage in animal cells. *Biological Reviews*, 33(1):103–135, 1958.

[95] K. Swanson, R. Rockne, J. Rockhill, and E. Alvord. Combining mathematical modeling with serial mr imaging to quantify and predict response to radiation therapy in individual glioma patients. *Neuro-Oncology*, 9(4):575–575, 2007.

[96] K. R. Swanson. *Mathematical modeling of the growth and control of tumors*. 1999.

[97] K. R. Swanson, E. Alvord, and J. Murray. A quantitative model for differential motility of gliomas in grey and white matter. *Cell proliferation*, 33(5):317–329, 2000.

[98] K. R. Swanson, E. Alvord, and J. Murray. Virtual brain tumours (gliomas) enhance the reality of medical imaging and highlight inadequacies of current therapy. *British journal of cancer*, 86(1):14–18, 2002.

[99] K. R. Swanson and E. C. Alvord Jr. Serial imaging observations and postmortem examination of an untreated glioblastoma: a traveling wave of glioma growth and invasion. *Neuro-oncol*, 4(4):340, 2002.

[100] K. R. Swanson, H. L. Harpold, D. Peacock, R. Rockne, C. Pennington, L. Kilbride, R. Grant, J. M. Wardlaw, and E. C. Alvord Jr. Velocity of radial expansion of contrast-enhancing gliomas and the effectiveness of radiotherapy in individual patients: a proof of principle. *J Clin Oncol*, 20:301–308, May 2008.

[101] M. D. Szeto, G. Chakraborty, J. Hadley, R. Rockne, M. Muzi, E. C. Alvord, K. A. Krohn, A. M. Spence, and K. R. Swanson. Quantitative metrics of net proliferation and invasion link biological aggressiveness assessed by mri with hypoxia assessed by fmiso-pet in newly diagnosed glioblastomas. *Cancer Research*, 69(10):4502–4509, 2009.

[102] S. Takayama, M. Sasahara, K. Iihara, J. Handa, and F. Hazama. Platelet-derived growth factor b-chain-like immunoreactivity in injured rat brain. *Brain research*, 653(1):131–140, 1994.

[103] L. Tao and C. Nicholson. Diffusion of albumins in rat cortical slices and relevance to volume transmission. *Neuroscience*, 75(3):839 – 847, 1996.

[104] J. H. Taylor, P. S. Woods, and W. L. Hughes. The organization and duplication of chromosomes as revealed by autoradiographic studies using tritium-labeled thymidinee. *Proceedings of the National Academy of Sciences of the United States of America*, 43(1):122, 1957.

[105] R. G. Thorne, S. Hrabětová, and C. Nicholson. Diffusion of epidermal growth factor in rat brain extracellular space measured by integrative optical imaging. *Journal of Neurophysiology*, 92(6):3471–3481, 2004.

[106] H.-H. Tsai, M. Tessier-Lavigne, and R. H. Miller. Netrin 1 mediates spinal cord oligodendrocyte precursor dispersal. *Development*, 130(10):2095–2105, 2003.

[107] V. Tyagi, J. Theobald, J. Barger, M. Bustoros, N. S. Bayin, A. S. Modrek, M. Kader, E. G. Anderer, B. Donahue, G. Fatterpekar, et al. Traumatic brain injury and subsequent glioblastoma development: Review of the literature and case reports. *Surgical Neurology International*, 7, 2016.

[108] C. V. Ustach, W. Huang, M. K. Conley-LaComb, C.-Y. Lin, M. Che, J. Abrams, and H.-R. C. Kim. A novel signaling axis of matriptase/pdgf-d/-pdgfr in human prostate cancer. *Cancer Research*, 70(23):9631–9640, 2010.

[109] P. van der Valk, J. Lindeman, and W. Kamphorst. Growth factor profiles of human gliomas: Do non-tumour cells contribute to tumour growth in glioma? *Annals of Oncology*, 8(10):1023–1029, 1997.

[110] P. van Heyningen, A. R. Calver, and W. D. Richardson. Control of progenitor cell number by mitogen supply and demand. *Current Biology*, 11:232–241, Feb 2001.

[111] R. G. Verhaak, K. A. Hoadley, E. Purdom, V. Wang, Y. Qi, M. D. Wilkerson, C. R. Miller, L. Ding, T. Golub, J. P. Mesirov, et al. Integrated genomic analysis identifies clinically relevant subtypes of glioblastoma characterized by abnormalities in pdgfra, idh1, egfr, and nf1. *Cancer cell*, 17(1):98–110, 2010.

[112] C. H. Wang, J. K. Rockhill, M. Mrugala, D. L. Peacock, A. Lai, K. Jusenius, J. M. Wardlaw, T. Cloughesy, A. M. Spence, R. Rockne, E. C. Alvord, and K. R. Swanson. Prognostic significance of growth kinetics in newly diagnosed glioblastomas revealed by combining serial imaging with a novel biomathematical model. *Cancer Research*, 69(23):9133–9140, 2009.

[113] B. Westermark, C. H. Heldin, and M. Nister. Platelet-derived growth factor in human glioma. *Glia*, 15(3):257–63.

[114] G. Wolswijk and M. Noble. Cooperation between pdgf and fgf converts slowly dividing o-2aadult progenitor cells to rapidly dividing cells with characteristics of o-2aperinatal progenitor cells. *The Journal of Cell Biology*, 118(4):889–900, 1992.

[115] J. H. Wright, M. M. Johnson, M. Shimizu-Albergine, R. L. Bauer, B. J. Hayes, J. Surapisitchat, K. L. Hudkins, K. J. Riehle, S. C. Johnson, M. M. Yeh, et al. Paracrine activation of hepatic stellate cells in platelet-derived growth factor c transgenic mice: Evidence for stromal induction of hepatocellular carcinoma. *International Journal of Cancer*, 134(4):778–788, 2014.

[116] A. Younger, K. Wing, M. Penner, and M. Cresswell. A study to evaluate the safety of platelet-derived growth factor for treatment of osteochondral defects of the talus. *Knee Surgery, Sports Traumatology, Arthroscopy*, 24(4):1250–1258, 2016.

[117] H. Zhang, L. Vutskits, V. Calaora, P. Durbec, and J. Z. Kiss. A role for the polysialic acid neural cell adhesion molecule in pdgf-induced chemotaxis of oligodendrocyte precursor cells. *Journal of Cell Science*, 117:93–103, 2003.

Appendix A

STEADY STATES OF PROLIFERATION–INVASION–RECRUITMENT MODEL

The Proliferation–Invasion–Recruitment (PIR) model describes the growth of PDGF–driven brain tumors. Understanding the steady states of such a model could be helpful in understanding what conditions could lead to a cessation of tumor growth. Moreover, analyzing the stability of those could elucidate whether there are any conditions for which pattern formation might occur, as is possible in models of multiple interacting species. Here we find the uniform steady states of the model and look at the stability of this with respect to both spatially homogeneous and spatially heterogeneous perturbations.

A.1 Uniform Steady States

At the uniform steady state, all derivatives are 0. Thus we set the time derivatives

$$\frac{\partial c}{\partial t}, \frac{\partial r}{\partial t}, \frac{\partial p}{\partial t}, \frac{\partial n}{\partial t} = 0, \tag{A.1}$$

and the spatial derivatives

$$\nabla \cdot (D_c \cdot \nabla c), \nabla \cdot (D_r \cdot \nabla r), \nabla \cdot (D_p \cdot \nabla p) = 0. \tag{A.2}$$

Putting these into our model equations (4.1)–(4.4), we have:

$$\frac{\partial c}{\partial t} = \nabla \cdot (D_c \nabla c) - \rho_c \frac{\beta (p + p_{auto})}{\beta (EC_{50}) + \beta (p + p_{auto})} c \left(1 - \frac{c + r + n}{K}\right) \tag{A.3}$$

$$\frac{\partial r}{\partial t} = \nabla \cdot (D_r \nabla r) - \rho_r \frac{\beta (p)}{\beta (EC_{50}) + \beta (p)} r \left(1 - \frac{c + r + n}{K}\right) \tag{A.4}$$

$$\frac{\partial p}{\partial t} = \nabla \cdot (D_p \nabla p) + \eta_c c - q_c \alpha \beta(p) c - q_r \beta(p) r \tag{A.5}$$

$$\frac{\partial n}{\partial t} = -\lambda (c + r) n \tag{A.6}$$

(A.7)

we are left with the following system of four equations and four variables to solve:

$$\rho_c \frac{\beta(p+p_{auto})}{\beta(EC_{50})+\beta(p+p_{auto})} c\left(1-\frac{c+r+n}{K}\right)=0 \tag{A.8}$$

$$\rho_r \frac{\beta(p)}{\beta(EC_{50})+\beta(p)} r\left(1-\frac{c+r+n}{K}\right)=0 \tag{A.9}$$

$$\eta_c c - q_c\beta(p)\alpha c - q_r\beta(p)r = 0 \tag{A.10}$$

$$-\lambda(c+r)n = 0 \tag{A.11}$$

Solutions of the c equation. Now, solving equation (A.8), there are a three possibilities: either $\rho_c \frac{\beta(p+p_{auto})}{\beta(EC_{auto})+\beta(p+p_{auto})} = 0$, $c = 0$, or $1 - \frac{c+r+n}{K} = 0$.

Our first option gives

$$\rho_c \frac{\beta(p+p_{auto})}{\beta(EC_{auto})+\beta(p+p_{auto})} = 0 \tag{A.12}$$

$$\implies \beta(p+p_{auto}) = 0 \tag{A.13}$$

(A.14)

Recalling the definition $\beta(p) = \frac{p}{k_m+p}$, this becomes

$$\frac{p+p_{auto}}{k_m+p+p_{auto}} = 0 \tag{A.15}$$

$$\implies p+p_{auto} = 0 \tag{A.16}$$

$$\implies p = -p_{auto} \tag{A.17}$$

Since we cannot physically have negative concentrations (once something is depleted, you cannot remove any more of it), this is only actually possible for $p = 0 = p_{auto}$. However, in our model, we have parameter $p_{auto} > 0$. Thus, this solution is nonphysical.

The next option requires no additional work: $c = 0$.

Finally, the third option, $1 - \frac{c+r+n}{K} = 0$ implies $1 = \frac{c+r+n}{K}$, and multiplying both sides by K, we have the result that $c + r + n = K$. This means that at steady state, the total cell density is equal to the carrying capacity.

Solutions of the r equation. The solutions to equation (A.9) are similar to those for equation (A.8) above—either $\rho_r \frac{\beta(p)}{\beta(EC_{50})+\beta(p)} = 0$, $r = 0$, or $1 - \frac{c+r+n}{K} = 0$.

First, $\rho_r \frac{\beta(p)}{(\beta(EC_{50})+\beta(p)} = 0$ implies that $\beta(p) = p/(km + p) = 0$ and thus, $p = 0$.

The second solution $r = 0$, requires no additional work.

The third solution, $1 - \frac{c+r+n}{K} = 0$, as before, happens when $c + r + n = K$.

Solutions of the p equation. More work is needed in solving equation (A.10), and we will see that the solution is more complex and nontrivial than for the other equations we have solved thus far:

$$\eta_c c - q_c \beta(p) \alpha c - q_r \beta(p) r = 0. \tag{A.18}$$

Adding the q_c, q_r terms to both sides and factoring out $\beta(p)$ gives

$$\eta_c c = \beta(p) \left(q_c \alpha c + q_r r \right) \tag{A.19}$$

Recalling that $\beta(p) = \frac{p}{k_m+p}$, this is

$$\eta_c c = \frac{p}{k_m + p} \left(q_c \alpha c + q_r r \right). \tag{A.20}$$

Dividing both sides by the q terms, we have

$$\frac{p}{k_m + p} = \frac{\eta_c c}{q_c c \alpha + q_r r}, \tag{A.21}$$

and solve this expression for p:

$$p = \frac{\eta_c c}{q_c c\alpha + q_r r}(k_m + p) = \frac{\eta_c c}{q_c c\alpha + q_r r}k_m + \frac{\eta_c c}{q_c c\alpha + q_r r}p \tag{A.22}$$

$$\implies p\left(1 - \frac{\eta_c c}{q_c c\alpha + q_r r}\right) = \frac{\eta_c c}{q_c c\alpha + q_r r}k_m \tag{A.23}$$

$$\implies p = \frac{\frac{\eta_c c k_m}{q_c c\alpha + q_r r}}{1 - \frac{\eta_c c}{q_c c\alpha + q_r r}}. \tag{A.24}$$

Fortunately, this expression can be simplified. Multiplying both the numerator and the denominator by $(q_c\alpha c + q_r r)/(\eta_c c)$, we have

$$p = \frac{k_m}{\frac{q_c c\alpha + q_r r}{\eta_c c} - 1}. \tag{A.25}$$

Now, substituting the 1 in the denominator with $1 = (\eta_c c)/(\eta_c c)$, we have

$$p = \frac{k_m}{\frac{q_c c\alpha + q_r r - \eta_c c}{\eta_c c}}. \tag{A.26}$$

Finally, multiplying the right hand side by $(\eta_c c)/(\eta_c c)$, we arrive at the simplified solution:

$$p = \frac{k_m \eta_c c}{(q_c\alpha - \eta_c)c + q_r r}. \tag{A.27}$$

Note that the solution depends on both c and r. This means that the value of p at steady state depends on the steady state values of c and r.

Solutions of the n equation. The last equation (A.11) is the most simple to solve. $n_t = -\lambda(c + r)n = 0$ implies that either $c + r = 0$ or $n = 0$. Thus, at steady state, either the brain has no transduced or recruited cells (no tumor) or has no normal brain cells (n). Another way of viewing this is that at steady state the brain is either composed entirely of transduced and recruited glial progenitor cells (i.e., cancer), or all normal brain cells, exclusive of any glial progenitor cells. The density of these cells may or may not be at the carrying capacity, depending on where the various solutions found above co-occur.

Combining solutions into the steady states. There are several possibilties that these solutions lead us to for the steady states. However, as we will show, only one corresponds to the physically relevant regime.

First, there is a possible equilibrium solution corresponding to the $c + r = 0$ solution of equation (A.11). In that case, $r = -c$, such that substitution in (A.27) gives

$$p = \frac{k_m \eta_c c}{(q_c \alpha - \eta_c)c - q_r c} \tag{A.28}$$

$$= \frac{k_m \eta_c c}{(q_c \alpha - \eta_c - q_r)c} \tag{A.29}$$

$$= \frac{k_m \eta_c}{q_c \alpha - \eta_c - q_r} \tag{A.30}$$

as the particular value of p, for this equilibrium. Looking at the equations (A.8) and (A.9), we must have either $c, r = 0$ or $c + r + n = K$, since $p > 0$. Since $c + r = 0$, the second option reduces to $n = K$. If $c, r = 0$, we have no constraint on the value of variable n; if we instead take $n = K$, there is no constraint on the value of c or r other than that $c = -r$. This is clearly not physiologically possible - we cannot have negative values of cell densities. However, given our initial conditions and the increasing nature of equations (A.3) and (A.4), we also will never have $c, r = 0$.

Another possibility is that we have $n = 0$ as a solution to (A.11), paired with $c = 0$ as a solution to (A.8). Then, substituting $c = 0$ into (A.27) gives $p = 0$ as a solution to (A.10). This is also a solution to (A.9), so we have at this solution that r could be anything.

Third, we can again take $n = 0$ as a solution to (A.11), this time along with the $p = -p_{auto}$ solution to (A.8) and the $c + r = K$ solution to (A.9). However, we note that $p = -p_{auto}$ is not physically possible since we cannot have negative quantities, so we move on to the next possiblity.

The most interesting and only physically relevant equilibrium solution comes from taking $c + r = K$, a solution to equations (A.8) and (A.9). This necessitates that we take $n = 0$ as our solution to equation (A.11), and then p is a function of c and r, given by (A.27). Note that the previous solution is really just one case of this equilibrium solution that occurs

outside the physiologic domain, but it is possible to have values in the physiogic domain that correspond to this equilibrium.

Since we have positive initial conditions and equations (A.3) and (A.4) are increasing we will tend toward $c+r=K$ in our solutions. Similarly, since equation (A.6) is decreasing, we will tend toward $n=0$ in our solutions. Note however, that in reality, a patient or animal with a tumor will die before steady state is attained at every location in the spatial domain. At a lethal tumor burden, we do observe that $c+r=K$ and $n=0$ at the center of our simulated tumors (see Fig. 4.4B), but the tumor has not yet filled the entire domain, and thus our system has not yet reached the uniform steady state.

In summary, steady state solutions are:

Steady state 1: nontrivial, not achievable given initial conditions.

$$\text{Glial progenitor cells: } c, r = 0 \tag{A.31}$$

$$\text{PDGF: } p = \frac{k_m \eta_c}{q_c \alpha - \eta_c - q_r} \tag{A.32}$$

$$\text{Other brain cells: } n \text{ can be anything} \tag{A.33}$$

This is a particular case of the next steady state, since $c+r=0$ for $c, r=0$, however in the following we assume that $c+r=0$ and $c, r \neq 0$.

Steady state 2: nontrivial, not physical due to negative cell quantity.

$$\text{Glial progenitor cells: } c+r=0 \text{ such that } c=-r \tag{A.34}$$

$$\text{PDGF: } p = \frac{k_m \eta_c}{q_c \alpha - \eta_c - q_r} \tag{A.35}$$

$$\text{Other brain cells: } n = K \tag{A.36}$$

Steady State 3: trivial, not achievable given initial conditions.

$$\text{Glial progenitor cells: } c = 0, \ r \text{ anything} \tag{A.37}$$

$$\text{PDGF: } p = 0 \tag{A.38}$$

$$\text{Other brain cells: } n = 0 \tag{A.39}$$

Steady State 4: nontrivial, achievable.

$$\text{Glial progenitor cells: } c + r = K, \tag{A.40}$$

$$\text{Steady state for PDGF: } p = \frac{k_m \eta_c c}{(q_c \alpha - \eta_c)c + q_r r}, \tag{A.41}$$

$$\text{Remaining brain cells: } n = 0. \tag{A.42}$$

Of these, only steady state 4 is both physically possible (no negative physical quantities) and attainable by our model due to the initial conditions, which stipulate that $r > 0$. It is worth noting that while achievable by our model, this steady state reflects a brain full of tumor—lethality occurs from tumor burden before it reaches that magnitude, making it unrealistic for the biological setting.

Notice that at this uniform steady state the concentration of PDGF, p, depends on both the c and r cell densities, so it is possible to have various proportions of these three at steady state, giving rise to a line of equilibrium. Knowing one of these values, we can then deduce what the other values will be using equations (A.40) and (A.41). To better illustrate this, let us define a variable θ to represent the ratio of recruited to total tumor cells,

$$\theta = \frac{r}{c + r}, \tag{A.43}$$

such that at steady state we have $r = \theta K$ and $c = (1 - \theta)K$. Substituting these into (A.41), we have

$$p = \frac{k_m \eta_c (1 - \theta)K}{(q_c \alpha - \eta_c)(1 - \theta)K + q_r \theta K}, \tag{A.44}$$

which gives us the relationship between the PDGF concentration, p, and the proportion, θ, of tumor that is comprised of recruited cells. A graph of this relationship is plotted in figure A.1.

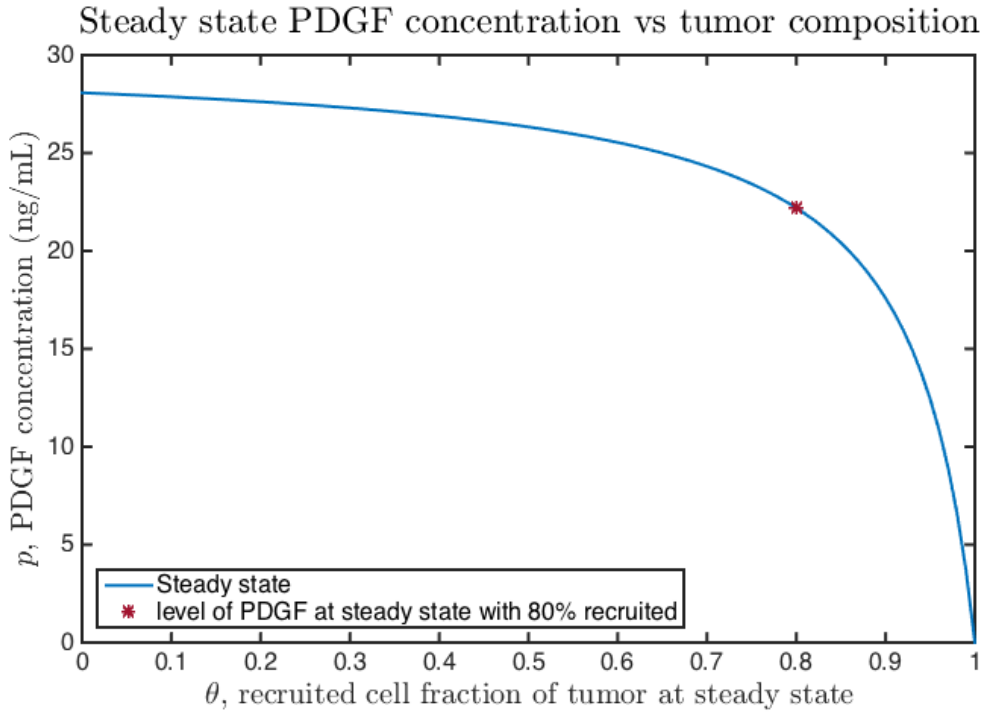

Figure A.1: **Steady state PDGF concentration vs Recruited cell percentage.** The steady state of platelet-derived growth factor concentration depends on the percentage of recruited cells in the tumor at steady state, as shown in (A.44). The astrisk represents the PDGF level for a tumor that is comprised of 80% recruited cells at steady state.

A.2 Linear Stability Analysis

Although we do not expect to ever reach any of these uniform steady states in our simulations, as noted in the previous section, we are still interested in the stability of steady states. For this analysis, we will focus on Steady State 4, which is the only steady state that we could possibly achieve given physiological constraints (i.e., our positive initial conditions and parameter values).

A.2.1 Linear stability of steady state to spatially homogeneous perturbations.

Denoting the steady state of interest as c_*, r_*, p_*, and n_*, I linearize my model as follows. First, let $\vec{\omega}$ represent the vector of spatially homogeneous perturbations:

$$\vec{\omega} = \begin{bmatrix} c(t) - c_* \\ r(t) - r_* \\ p(t) - p_* \\ n(t) - n_* \end{bmatrix} = \begin{bmatrix} \hat{c}(t) \\ \hat{r}(t) \\ \hat{p}(t) \\ \hat{n}(t) \end{bmatrix}, \tag{A.45}$$

where the $\hat{c}, \hat{r}, \hat{p}, \hat{n}$ are the perturbations for c, r, p, n, respectively, and $|\vec{\omega}|$ is assumed to be small.

Then we can substitute

$$\begin{bmatrix} c(t) \\ r(t) \\ p(t) \\ n(t) \end{bmatrix} = \begin{bmatrix} \hat{c}(t) + c_* \\ \hat{r}(t) + r_* \\ \hat{p}(t) + p_* \\ \hat{n}(t) + n_* \end{bmatrix} \tag{A.46}$$

into the model equations:

$$\begin{aligned} \frac{\partial \hat{c}}{\partial t} =& \nabla \cdot \left(\overline{D}_c(\hat{c}(t) + c_*, \hat{r}(t) + r_*, \hat{p}(t) + p_*, \hat{n}(t) + n_*) \nabla(\hat{c}(t) + c_*) \right) \\ & + f\left(\hat{c} + c_*, \hat{r} + r_*, \hat{p} + p_*, \hat{n} + n_*\right) \qquad \text{(A.47)} \\ \frac{\partial \hat{r}}{\partial t} =& \nabla \cdot \left(\overline{D}_r(\hat{c}(t) + c_*, \hat{r}(t) + r_*, \hat{p}(t) + p_*, \hat{n}(t) + n_*) \nabla(\hat{r}(t) + r_*) \right) \\ & + g\left(\hat{c} + c_*, \hat{r} + r_*, \hat{p} + p_*, \hat{n} + n_*\right) \qquad \text{(A.48)} \\ \frac{\partial \hat{p}}{\partial t} =& \nabla \cdot \left(D_p \nabla(\hat{p}(t) + p_*) \right) + h\left(\hat{c} + c_*, \hat{r} + r_*, \hat{p} + p_*, \hat{n} + n_*\right) \qquad \text{(A.49)} \\ \frac{\partial \hat{n}}{\partial t} =& l\left(\hat{c} + c_*, \hat{r} + r_*, \hat{p} + p_*, \hat{n} + n_*\right) \qquad \text{(A.50)} \end{aligned}$$

where f is the reaction term of equation (A.8), g that of the equation (A.9), h that of (A.10), and l that of equation (A.11) as follows:

$$f = \rho_c \frac{\beta(p + p_{auto})}{\beta(EC_{50}) + \beta(p + p_{auto})} c \left(1 - \frac{c + r + n}{K}\right) \tag{A.51}$$

$$g = \rho_r \frac{\beta(p)}{\beta(EC_{50}) + \beta(p)} r \left(1 - \frac{c + r + n}{K}\right) \tag{A.52}$$

$$h = \eta_c c - q_c \beta(p) \alpha c - q_r \beta(p) r \tag{A.53}$$

$$l = -\lambda (c + r) n. \tag{A.54}$$

Collecting terms of order $\mathcal{O}(|\vec{\omega}|)$ we get equations of the form:

$$\frac{\partial \hat{c}}{\partial t} = f_c(c_*, r_*, p_*, n_*)\hat{c} + f_r(c_*, r_*, p_*, n_*)\hat{r} + f_p(c_*, r_*, p_*, n_*)\hat{p} + f_n(c_*, r_*, p_*, n_*)\hat{n} \tag{A.55}$$

$$\frac{\partial \hat{r}}{\partial t} = g_c(c_*, r_*, p_*, n_*)\hat{c} + g_r(c_*, r_*, p_*, n_*)\hat{r} + g_p(c_*, r_*, p_*, n_*)\hat{p} + g_n(c_*, r_*, p_*, n_*)\hat{n} \tag{A.56}$$

$$\frac{\partial \hat{p}}{\partial t} = h_c(c_*, r_*, p_*, n_*)\hat{c} + h_r(c_*, r_*, p_*, n_*)\hat{r} + h_p(c_*, r_*, p_*, n_*)\hat{p} + h_n(c_*, r_*, p_*, n_*)\hat{n} \tag{A.57}$$

$$\frac{\partial \hat{n}}{\partial t} = l_c(c_*, r_*, p_*, n_*)\hat{c} + l_r(c_*, r_*, p_*, n_*)\hat{r} + l_p(c_*, r_*, p_*, n_*)\hat{p} + l_n(c_*, r_*, p_*, n_*)\hat{n}. \tag{A.58}$$

The indicated derivatives evaluated at the steady state are as follows:

$$
\begin{aligned}
f_c(c_*, r_*, p_*, n_*) &= \frac{-c_*}{K}\rho_c \frac{\beta(p_* + p_{auto})}{\beta(EC_{50}) + \beta(p_* + p_{auto})} \\
f_r(c_*, r_*, p_*, n_*) &= \frac{-c_*}{K}\rho_c \frac{\beta(p_* + p_{auto})}{\beta(EC_{50}) + \beta(p_* + p_{auto})} \\
f_p(c_*, r_*, p_*, n_*) &= 0 \\
f_n(c_*, r_*, p_*, n_*) &= \frac{-c_*}{K}\rho_c \frac{\beta(p_* + p_{auto})}{\beta(EC_{50}) + \beta(p_* + p_{auto})} \\
g_c(c_*, r_*, p_*, n_*) &= \frac{-r_*}{K}\rho_r \frac{\beta(p_*)}{\beta(EC_{50}) + \beta(p_*)} \\
g_r(c_*, r_*, p_*, n_*) &= \frac{-r_*}{K}\rho_r \frac{\beta(p_*)}{\beta(EC_{50}) + \beta(p_*)} \\
g_p(c_*, r_*, p_*, n_*) &= 0 \\
g_n(c_*, r_*, p_*, n_*) &= \frac{-r_*}{K}\rho_r \frac{\beta(p_*)}{\beta(EC_{50}) + \beta(p_*)} \\
h_c(c_*, r_*, p_*, n_*) &= \eta_c - q_c\beta(p_*)\alpha \\
h_r(c_*, r_*, p_*, n_*) &= -q_r\beta(p_*) \\
h_p(c_*, r_*, p_*, n_*) &= -\frac{k_m}{(k_m + p)^2}\left(q_r r_* + q_c\alpha c_*\right) \\
h_n(c_*, r_*, p_*, n_*) &= 0 \\
l_c(c_*, r_*, p_*, n_*) &= -\lambda n_* \\
l_r(c_*, r_*, p_*, n_*) &= -\lambda n_* \\
l_p(c_*, r_*, p_*, n_*) &= 0 \\
l_n(c_*, r_*, p_*, n_*) &= -\lambda c_* - \lambda r_*
\end{aligned}
\tag{A.59}
$$

General solutions of $\partial\hat{c}/\partial t,\ \partial\hat{r}/\partial t,\ \partial\hat{p}/\partial t,$ and $\partial\hat{n}/\partial t$ have the form $\vec{\omega} \propto \vec{\omega}_0 \exp\{\boldsymbol{\lambda} t\}$, where here $\boldsymbol{\lambda}$ refers to an eigenvalue, not the model parameter, and $\vec{\omega}_0$ is an eigenvalue of the

stability matrix, A:

$$A = \left[\begin{array}{cccc} f_c & f_r & 0 & f_n \\ g_c & g_r & 0 & g_n \\ h_c & h_r & h_p & 0 \\ l_c & l_r & 0 & l_n \end{array} \right]_{(c_*, r_*, p_*, n_*)} \tag{A.60}$$

thus satisfying $\boldsymbol{\lambda}\vec{\omega}_0 = A\vec{\omega}_0$.

Notice that for our steady state of interest, namely (A.42), $l_c = l_r = 0$. Further, we see in (A.59) that $f_c = f_r = f_n$ and that $g_c = g_r = g_n$.

Incorporating these simplifications, A becomes:

$$A = \left[\begin{array}{cccc} f_c & f_c & 0 & f_c \\ g_c & g_c & 0 & g_c \\ h_c & h_r & h_p & 0 \\ 0 & 0 & 0 & l_n \end{array} \right]_{(c_*, r_*, p_*, n_*)} \tag{A.61}$$

Now, for the solutions of $\partial\hat{c}/\partial t$, $\partial\hat{r}/\partial t$, $\partial\hat{p}/\partial t$, and $\partial\hat{n}/\partial t$ to be nontrivial, then the eigenvalues $\boldsymbol{\lambda}$ must satisfy the characteristic equation:

$$|A - \boldsymbol{\lambda} I| = \left| \begin{array}{cccc} f_c - \boldsymbol{\lambda} & f_c & 0 & f_c \\ g_c & g_c - \boldsymbol{\lambda} & 0 & g_c \\ h_c & h_r & h_p - \boldsymbol{\lambda} & h_n \\ 0 & 0 & 0 & l_n - \boldsymbol{\lambda} \end{array} \right|_{(c_*, r_*, p_*, n_*)} = 0 \tag{A.62}$$

where $|\cdot|$ is the determinant operator.

Solving for our eigenvalues, we find that

$$|A - \boldsymbol{\lambda} I| = \left[\boldsymbol{\lambda}^2 - \boldsymbol{\lambda}\left(f_c + g_c\right)\right]\left(h_p - \boldsymbol{\lambda}\right)\left(l_n - \boldsymbol{\lambda}\right) \tag{A.63}$$

giving us the following eigenvalues:

$$\boldsymbol{\lambda}_1 = 0 \tag{A.64}$$

$$\boldsymbol{\lambda}_2 = f_c(c_*, r_*, p_*, n_*) + g_c(c_*, r_*, p_*, n_*) \tag{A.65}$$

$$\boldsymbol{\lambda}_3 = h_p(c_*, r_*, p_*, n_*) \tag{A.66}$$

$$\boldsymbol{\lambda}_4 = l_n(c_*, r_*, p_*, n_*) \tag{A.67}$$

$$\tag{A.68}$$

If $Re\{\boldsymbol{\lambda}\} > 0$, then the uniform steady state is linearly unstable. On the otherhand, if $Re\{\boldsymbol{\lambda}\} < 0$, then the perturbations will decay and return to the steady state. As we noted in Chapter 2, in Section 2.3.2 $\boldsymbol{\lambda} = 0$ if and only if there is more than one equilibrium, and indeed the uniform steady state of interest is a line as we showed in Figure A.1 and the accompanying text.

Since our parameter values are all positive, and the steady states $c_*, r_*, p_*, n_* \geq 0$, we have from (A.59) that $f_c(c_*, r_*, p_*, n_*), g_c(c_*, r_*, p_*, n_*), h_p(c_*, r_*, p_*, n_*), l_n(c_*, r_*, p_*, n_*) < 0$. Thus, eigenvalues $\boldsymbol{\lambda}_2$, $\boldsymbol{\lambda}_3$, and $\boldsymbol{\lambda}_4 < 0$.

Therefore, we have linear stability of the nontrivial and achievable steady state to spatially homoogeneous perturbations. This is not unexpected given the fact that we have no loss of c or r cells in our model and the steady state is a domain filled to carrying capacity with those cells. We conclude from our stability result that this steady state is trivial from the stand point of understanding model behavior, along with the other steady states that were found to be trivial and/or unachievable.

Appendix B

WHERE TO FIND CODE FILES

Codes for Chapter 3 can be found here:

`https://github.com/scmassey/varied_paracrine_PDGF_dynamics`

Codes for Chapter 7 can be found here:

`https://github.com/scmassey/2D_Proliferation-Invasion-Recruitment`

VITA

Susan Christine Massey

Precision Neurotherapeutics (PNT) Innovation Program

Mayo Clinic, Arizona

5777 East Mayo Boulevard,

Phoenix, AZ 85054

Massey.Susan@mayo.edu

Education.

Ph.D., Applied Mathematics, University of Washington, Seattle, WA, Dec. 2016

M.Sc., Applied Mathematics, University of Washington, Seattle, WA, Dec. 2011

B.S., Mathematics, University of Washington, Seattle, WA, June 2008

Professional Experience.

2015– Informatics Specialist I, Precision Neurotherapeutics Innovation Program
Mayo Clinic Arizona, Phoenix, AZ

2014–2015 Teaching and Research Assistant, Depts. of Mathematics and
Applied Mathematics, Universtiy of Washington, Seattle, WA

2010–2013 NSF Graduate Research Fellow, Dept. of Applied Mathematics,
University of Washington, Seattle, WA

2009–2010 NSF VIGRE Fellow, Dept. of Applied Mathematics,
University of Washington, Seattle, WA

2008–2009 Research Scientist I, Dept. of Pathology,
University of Washington, Seattle, WA

Honors and Awards.

2006–2008 McNair Scholar, Office of Minority Affairs, University of Washington

2007 Amgen Scholar, Undergraduate Research Program, University of Washington

2007–2008 Boeing Scholar, Office of Minority Affairs, University of Washington

2007–2008 Trjitzinsky Award, American Mathematcial Society

2008 Society for Industrial and Applied Mathematics (SIAM) University of Washington chapter poster contest winner

2008 Undergraduate research travel award

2009–2010 NSF Vertical Integration of Research and Education in the Mathematical Sciences (VIGRE) Fellowship

2010–2013 NSF Graduate Research Fellowship

2011 Amgen Fellows Travel Award

2016 Landahl–Busenberg Travel Grant, Society of Mathematical Biology

Professional Organization Memberships.

American Mathematical Society (AMS)

Association for Women in Mathematics (AWM)

Society for Industrial and Applied Mathematics (SIAM)

Society for Mathematical Biology (SMB)

Publications.

Peer-reviewed Journal Articles

- **S. C. Massey**, M. C. Assanah, K. A. Lopez, P. Canoll, K. R. Swanson. Progenitor cell recruitment drives aggressive glioma growth: mathematical and experimental modeling. *Journal of the Royal Society Interface*, 9:1757-1766, 2012.

- S. Ivkovic, C. Beadle, S. Noticewala, **S. C. Massey**, K. R. Swanson, L. N. Toro, A. R. Bresnick, P. Canoll P, S. S. Rosenfeld. Direct Inhibition of Myosin II Effectively

Blocks Glioma Invasion In the Present of Multiple Motogens. *Molecular Biology of the Cell*, 23:533-542, 2012.

- E. A. Stoll, B. A. Habibi, A. M. Mikheev, J. Lasiene, **S. C. Massey**, K. R. Swanson, R. C. Rostomily, P. J. Horner. A subpopulation of neural stem/progenitor cells in the aged subventricular zone has increased mitotic activity. *Stem Cells*, 29(12):2005-17, 2011.

- S. J. Lee, T. Seaborn, F. J. Mao, **S. C. Massey SC**, N. Q. Luu, M. A. Schubert, J. W. Chien, P. A. Carpenter, C. Moravec, P. J. Martin, M. E. D. Flowers. Frequency of abnormal findings detected by comprehensive evaluation at one year after allogeneic hematopoietic cell transplantation. *Biology of Blood and Marrow Transplantation*, 15(4):416-20, 2009.

Contributed Works

- **S. C. Massey** and K. Swanson. Reaction-Diffusion Model of PDGF-driven Recruitment in Experimental Glioblastoma. *BioRxiv*, doi: http://dx.doi.org/10.1101/038471 - to appear in the forthcoming National Cancer Institute (NCI) Handbook of Mathematical Methods in Cancer Biology.

- G. Chakraborty, R. Sodt, **S. C. Massey**, S. Gu, R. Rockne, E. C. Alvord, Jr., andK. R. Swanson. Bridging from Multiscale Modeling to Practical Clinical Applications in the Study of Human Gliomas. In: Multiscale Cancer Modeling. Ed. T.S. Deisboeck and G. Stamatakos. *CRC Press*, 2010. ISBN-10 1439814406

- **S. C. Massey**. Parameter sensitivity investigation of a mathematical model of glioma tumorigenesis mediated by platelet-derived growth factor. *The McNair Scholars Journal of the University of Washington*, 8:173-185, 2009.

Abstracts

- **S. C. Massey**, P. Canoll, K. R. Swanson. Abstracts from the 21st Annual Scientific Meeting and Education Day of the Society for Neuro-Oncology: TMOD-16. Biomathematical model of proneural tumors suggests best candidates for PDGF-inhibitor therapies. *Neuro-Oncology*, 18(suppl 6): vi210-vi210, 2016.

- **S. C. Massey**, K. R. Swanson, P. Canoll. Abstracts from the 15th Annual Meeting of the Society for Neuro-Oncology (SNO), November 1821, 2010, Montreal, Quebec, Canada: CB-84. PDGF-driven glioma model reveals that environmentally targeted therapies may be more effective at altering recurrent disease kinetics. *Neuro-Oncology*, 12(suppl 4): iv25, 2010.

- **S. C. Massey**, P. D. Canoll, K. R. Swanson. Abstracts from the 2009 Joint Meeting of the Society for Neuro-Oncology (SNO) and the American Association of Neurological Surgeons/Congress of Neurological Surgeons (AANS/CNS) Section on Tumors: 45. Modeling the effects of progenitor cell recruitment on glioma growth and progression. *Neuro-Oncology*, 11(5): 574-5, 2009.

Conference Presentations.

- Invited Talk, July 2016: Analyzing in situ cellular motion in experimental animal glioma models. The 2016 Joint Society for Mathematical Biology Annual Meeting and the European Conference for Mathematical and Theoretical Biology, University of Nottingham, Nottingham, United Kingdom.

- Contributed Talk, July 2011: Parameter Sensitivity Investigation of a Mathematical Model of Glioma Angiogenesis via Latin Hypercube Sampling. Presented at the European Conference for Mathematical and Theoretical Biology, Jagiellonian University, Kraków, Poland.

- Contributed Talk, June 2011: Parameter Sensitivity Investigation of a Mathematical Model of Glioma Angiogenesis via Latin Hypercube Sampling. Presented at the

Casablanca International Workshop in Mathematical Biology: Analysis and Control, Hassan II University, Casablanca, Morocco.

- Poster presentation, April 2011: Parameter sensitivity investigation of a mathematical model of glioma angiogenesis via Latin hypercube sampling. Presented at the Second Annual Physical Sciences–Oncology Centers (PS–OCs) Network Investigators Meeting, San Diego, CA.

- Poster presentation, November 2010: PDGF–driven glioma model reveals that environmentally targeted therapies may be more effective at altering recurrent disease kinetics. Presented at the 2010 Annual Meeting of the Society for Neuro-Oncology, Montreal, QC, Canada.

- Poster presentation, October 2009: Modeling the effects of progenitor cell recruitment on glioma growth and progression. Presented at the 2009 Joint Meeting of the Society for Neuro-Oncology and the AANS/CNS Section on Tumors, New Orleans, LA.

- Contributed Talk, July 2009: Paracrine PDGF Signaling and Progression in Experimental Gliomas. Presented at the Society for Mathematical Biology (SMB) Annual Meeting 2009 in Vancouver, BC, Canada.

- Platform presentation and Poster, January 2009: Parameter sensitivity investigation of a mathematical model of glioma tumorigenesis mediated by platelet-derived growth factor. Presented at the Mathematical Biosciences Institute (MBI) Workshop 4: Cancer Development, Angiogenesis, Progression, and Invasion, at Ohio State University, Columbus, OH.

- Contributed Talk, August 2008: Parameter sensitivity investigation of a mathematical model of glioma tumorigenesis mediated by platelet-derived growth factor. Presented

at the Society for Mathematical Biology (SMB) Annual Meeting 2008 in Toronto, ON, Canada.

- Poster, July 2008: Parameter sensitivity investigation of a mathematical model of glioma tumorigenesis mediated by platelet-derived growth factor. Presented at the 2008 SIAM Anxnual Meeting in San Diego, CA.

- Platform Presentation, May 2008: Modeling Glioma Tumorigenesis Mediated by Platelet Derived Growth Factor. Presented at the 2008 University of Washington McNair Research Conference, Seattle, WA.

Related Professional Experience.

- Co-organized a mini symposium, "Mathematical Oncology: Impacting the Clinic," for the 2016 Joint Society for Mathematical Biology Annual Meeting and the European Conference for Mathematical and Theoretical Biology, University of Nottingham, Nottingham, UK. Speakers:

  - David Dingli: "Dynamics of oncolytic virus spread within tumors."
  - Eunjung Kim: "Phase i trials in melanoma: a framework to translate preclinical findings to the clinic."
  - Alicia Martnez-Gonzlez: "Protracted metronomic therapies to target low-grade gliomas malignant transformation."
  - Heiko Enderling: "Proliferation saturation index predicts OPX GTV reduction to prospectively identify patients for adaptive radiotherapy."

- Panel member, June 2011: "How to foster working relationships between biologists and mathematicians." Casablanca International Workshop in Mathematical Biology: Analysis and Control, Hassan II University, Casablanca, Morocco.